Electrochemical Energy Reviews (2023) 6:14
https://doi.org/10.1007/s41918-022-00153-7

REVIEW ARTICLE

Recent Advancements in Photoelectrochemical Water Splitting for Hydrogen Production

Yibo Zhao[1] · Zhenjie Niu[1] · Jiwu Zhao[1] · Lan Xue[1] · Xianzhi Fu[1] · Jinlin Long[1]

Received: 19 September 2021 / Revised: 3 December 2021 / Accepted: 1 March 2022 / Published online: 30 March 2023

Abstract

Sunlight is the most abundant and inexhaustible energy source on earth. However, its low energy density, dispersibility and intermittent nature make its direct utilization with industrial relevance challenging, suggesting that converting sunlight into chemical energy and storing it is a valuable measure to achieve global sustainable development. Carbon–neutral, clean and secondary pollution-free solar-driven water splitting to produce hydrogen is one of the most attractive avenues among all the current options and is expected to realize the transformation from dependence on fossil fuels to zero-pollution hydrogen. Artificial photosynthetic systems (APSs) based on photoelectrochemical (PEC) devices appear to be an ideal avenue to efficiently achieve solar-to-hydrogen conversion. In this review, we comprehensively highlight the recent developments in photocathodes, including architectures, semiconductor photoabsorbers and performance optimization strategies. In particular, frontier research cases of organic semiconductors, dye sensitization and surface grafted molecular catalysts applied to APSs based on frontier (molecular) orbital theory and semiconductor energy band theory are discussed. Moreover, research advances in typical photoelectrodes with the metal–insulator–semiconductor (MIS) architecture based on quantum tunnelling are also introduced. Finally, we discuss the benchmarks and protocols for designing integrated tandem photoelectrodes and PEC systems that conform to the solar spectrum to achieve high-efficiency and cost-effective solar-to-hydrogen conversion at an industrial scale in the near future.

Keywords Photoelectrochemical (PEC) cells · Solar water splitting · Photocathodes · Semiconductors · Metal–insulator–semiconductor (MIS) heterostructure · Tandem photoelectrodes

1 Introduction

As the cleanest energy source, hydrogen will make a predictable contribution to inhibiting the growth of environmental carbon. Hydrogen, as a key industrial raw material, has been widely used in power generation, transportation, and synthetic fuels, upgrading oil/biomass, ammonia/fertilizer, metal production and chemical processes [1], because it has a superior gravimetric heating value of up to 141.9 MJ kg^{-1}, which is higher than that of methane (55.5 MJ kg^{-1}), gasoline (47.5 MJ kg^{-1}), diesel (44.8 MJ kg^{-1}) and methanol (20 MJ kg^{-1}), and a competitive advantage of zero emissions after combustion [2]. Conventional routes to industrial hydrogen production are based on coal-based water–gas shift (WGS) and fossil fuel reformation (generally, methane-dominated natural gas) processes, which commonly emit a large amount of CO_2 [2]. Among all hydrogen production options, the excess production capacities of power plants in the nighttime and solar energy in the daytime exhibit cost-effectiveness and superiority. A mature industrial system has been established for electrocatalytic hydrogen production from water splitting [3, 4], while solar-to-hydrogen conversion is still in the laboratory exploration and preliminary application stages due to the longstanding scientific challenges [5–7]. The solar energy received on the total surface (the land and the ocean) of the earth is 173 000 TW [8], which is 9 830 times the global primary energy consumption (17.6 TW) in 2020 [9]. The production capacity of installed photovoltaic (PV) power that can directly utilize solar energy was only 707.5 GW in 2020 [9]. Therefore, solar energy, as a

Yibo Zhao and Zhenjie Niu are contributed equally to this work.

✉ Jinlin Long
jllong@fzu.edu.cn

[1] State Key Laboratory of Photocatalysis On Energy and Environment, College of Chemistry, Fuzhou University, Fuzhou 350116, Fujian, China

renewable energy, urgently needs to be reasonably developed and utilized. Given the dispersion, intermittent nature and low power density of solar irradiation, the US Department of Energy has set an energy conversion target of 5% for valuable solar H_2 production [10]. To date, there are three typical conversion routes for solar water splitting: photocatalysis, PV-driven electrocatalysis (PV-EC) and integrated artificial photosynthetic systems (APSs) based on photoelectrochemical (PEC) devices [11, 12]. We focus on the last route, in which the integration of the light-harvesting and water splitting modules enables direct solar-to-hydrogen conversion, leading to fewer energy conversions and lower energy loss. [10]. Although considerable progress has been made in APS water splitting in recent years, there are still key issues, such as the solar-to-hydrogen conversion efficiency and stability, that need to be optimized to meet the cost-effective industrial requirements.

In this review, based on the latest research results on solar-driven hydrogen production, we review the recent advancements in APSs and discuss the difficulties and solutions encountered in photocathode materials. Moreover, the applications of organic semiconductors in PEC systems are highlighted from the perspective of frontier (molecular) orbital theory and semiconductor energy band theory, and their application potential is prospected. In particular, the application frontier of quantum (electron) tunnelling with statistical significance in photoelectrodes is introduced. Finally, the benchmarks and protocols for the design of high-efficiency tandem photoelectrodes and PEC systems are discussed.

2 Fundamentals of Water Splitting

The water splitting reaction consists of hydrogen evolution reaction (HER) and oxygen evolution reaction (OER). An energy input of $\Delta G = 273.15$ kJ mol^{-1} is required in thermodynamics for water splitting, which corresponds to a minimum Nernstian potential of + 1.23 V. The reaction equation has several manifestations depending on the conditions.

The water splitting reaction is

$$H_2O \rightarrow H_2 + 1/2O_2 \quad (1)$$

In an alkaline electrolyte,

$$\text{Cathode: } 2H_2O + 2e^- \rightarrow H_2 + 2OH^- \quad (2)$$

$$\text{Anode: } 2OH^- \rightarrow H_2O + 1/2O_2 + 2e^- \quad (3)$$

In an acidic electrolyte,

$$\text{Cathode: } 2H^+ + 2e^- \rightarrow H_2 \quad (4)$$

$$\text{Anode: } H_2O \rightarrow 2H^+ + 1/2O_2 + 2e^- \quad (5)$$

Generally, a potential larger than 1.23 V is required for electrochemical water splitting due to the voltage drop and overpotential. Among these, the voltage drop of the electrochemical cell originates from the resistance of the electrolyte, ohmic contact and ionic membrane. The catalytic activity of the electrocatalyst, the kinetic parameter activation energy and the restriction of diffusion on the electrode surface are the primary causes of overpotential in the anode and the cathode. The voltage drop can be reduced by optimizing the structural design of the electrochemical cell, but an overpotential decrease requires an electrocatalyst with superior performance. Figure 1a shows the mechanism of the HER in an acidic electrolyte, which includes three typical steps: the Volmer, Tafel and Heyrovsky steps. Specifically, in the Volmer step, H* is adsorbed on the surface of the catalyst by coupling a proton and an electron. Then, bonding of two adsorbed H* into H_2 is the Tafel step, whereas combination of the adsorbed H*, a free proton in the electrolyte and an electron into H_2 is the Heyrovsky step.

The Tafel slope, reflecting the overpotential and current density, is widely accepted for use in experimental assessment of the electrocatalytic performance of a material for a specific reaction. A low Tafel slope means that the catalyst only needs a small increase in overpotential to achieve a large increase in the current density [13]. However, a bond strength between the catalyst and adsorbed H* that is neither strong nor weak is the essential factor of efficient HER. Volcano diagrams were reported by Trasatti [14] and Nørskov [15] from the perspectives of the strength of the metal-hydrogen bond and hydrogen chemisorption energy, respectively (Fig. 1b and c). The active metals in Fig. 1b and c were divided into five categories based on the HER activity, combined with the electronic structure and physical properties (Fig. 1d). The chemisorption energies in the green and yellow regions are not moderate, and the ferromagnetic and $d^{10}s^1$ groups are not superior to noble metals in the HER (Fig. 1b and c). There is no doubt that platinum exhibits the best HER activity and the lowest overpotential among all noble metals.

3 Band Bending of Semiconductors

Thermodynamically, an input voltage of at least − 1.23 V from the grid is required even if platinum with unprecedented performance is used as the electrocatalyst for water splitting. Although solar-to-electricity conversion is considered to be the most scientific method, the energy dissipation and entropy increment depend on the number of conversions from low-density energy (e.g., solar energy) to high-density energy (e.g., electricity and chemical energy).

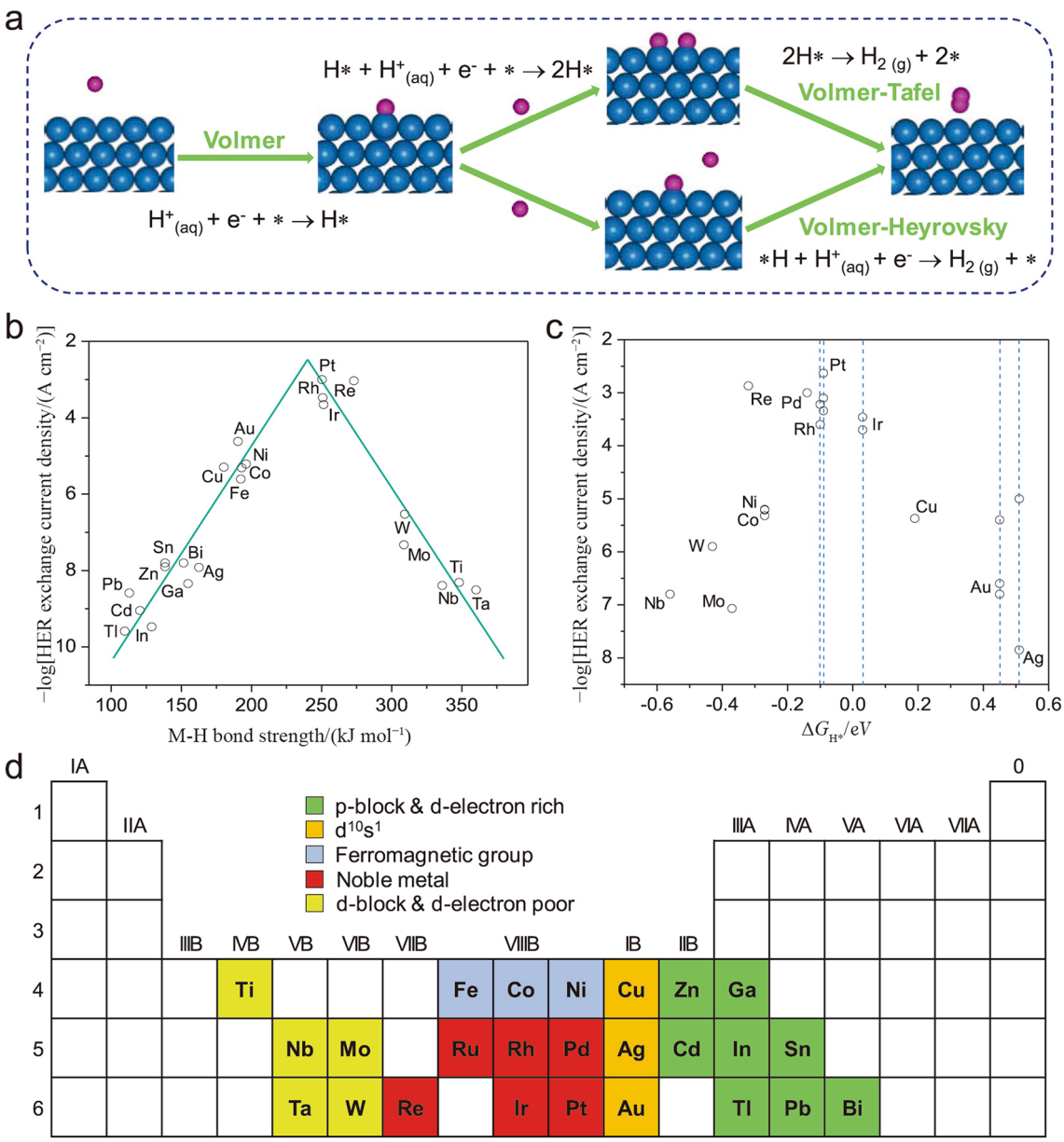

Fig. 1 Mechanism of the HER and the activity trend of electrocatalysts. **a** Mechanism of the HER on the surface of an electrode in an acidic electrolyte. **b** Volcano plot of the exchange current density for electrolytic hydrogen evolution vs. strength of the intermediate metal-hydrogen bond formed between absorbed H and the electrode surface. Reprinted with permission from Ref. [14]. Copyright © 1972 Published by Elsevier B.V. **c** Experimentally measured exchange current density for hydrogen evolution over different metal surfaces plotted as a function of the calculated hydrogen chemisorption energy per atom, ΔE_H. Reprinted with permission from Ref. [15]. Copyright © 2005 ECS-The Electrochemical Society, Inc. **d** Periodic table depicting the HER activity over different metals based on the electronic structure and physical properties. Based on data from Ref. [14, 15]

Therefore, the solar-driven HER is a perfect way to efficiently utilize solar energy. Specifically, hydrogen production by photocatalysis (PC) is a promising approach, but industrializing it is currently difficult because it commonly requires a high-value sacrificial agent to consume photogenerated holes [16]. Solar thermochemical or photothermal synergistic water decomposition to produce hydrogen is another feasible method, but it requires external facilities to maintain a high temperature (300–1 500 °C), which makes it uncompetitive [17–19]. Among all the options for solar-driven HER, the PEC system is superior due to the easy product separation, high efficiency, good durability and continuous operability [20–24]. The light-harvesting module in the PEC system is a semiconductor, which can be classified into the positive-type (the p-type, holes are the majority carriers), which is beneficial for the HER, and the negative-type

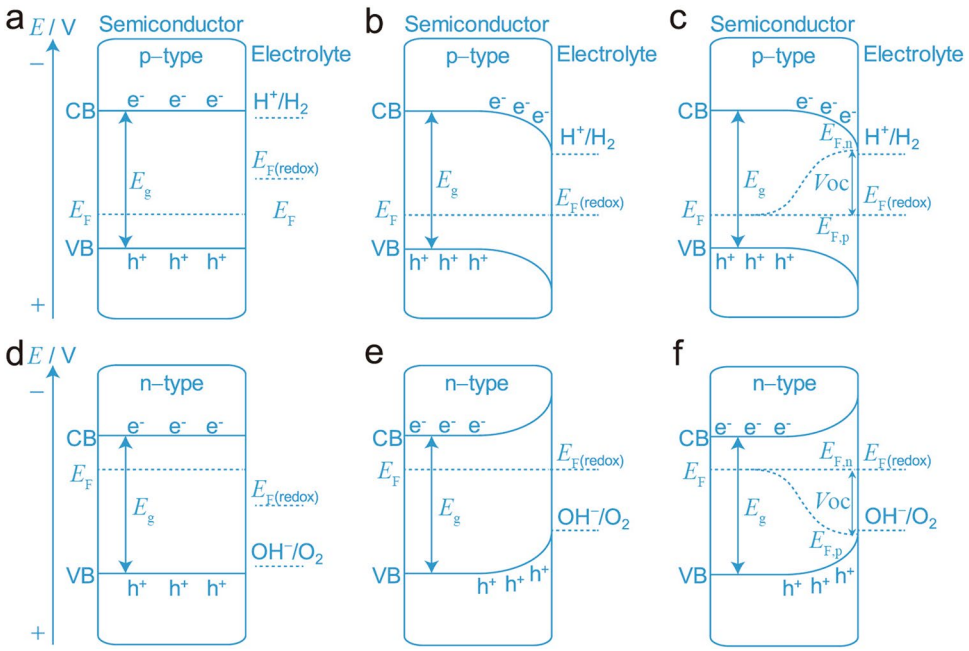

Fig. 2 Band diagram of p-type and n-type semiconductors immersed in an electrolyte with redox potential $E_{F(redox)}$ **a**, **d** before equilibrium; **b, e** at equilibrium; **c**, **f** with illumination of light or when biased. The open-circuit voltage is symbolized by V_{OC}, and the quasi-Fermi level is symbolized by $E_{F,\,p}$ (holes) and $E_{F,\,n}$ (electrons)

(the n-type, electrons are the majority carriers), which is beneficial for the OER [25–27].

As shown in Fig. 2a and d, the band diagram is composed of the forbidden band/band gap, whose electron probability is quantum mechanically forbidden, the valence band (VB) and the conduction band (CB). The Fermi level (E_F) should be located at the midpoint of the band gap in intrinsic semiconductors since the number of electrons is equal to the number of holes. However, the E_F of p-type semiconductors is close to the VB [28]. When a p-type semiconductor is immersed in an electrolyte and its E_F is more positive than the Fermi level ($E_{F(redox)}$) of the electrolyte, the charge carriers will be transferred from the electrolyte to the semiconductor until an equilibrium is established between E_F and $E_{F(redox)}$, while the opposite is true for an n-type semiconductor (Fig. 2b and 2e). After equilibrium, a depletion layer (the space-charge layer) is formed because the majority carriers of the semiconductor are depleted at the interface. Furthermore, the electrons and holes transfer in opposite directions due to the electric field derived from the band bending; specifically, the majority carriers transfer to the bulk, and the minority carriers move to the depletion layer (Fig. 2b and e).

Obviously, the minority carriers determine whether a reduction or an oxidation reaction occurs at the semiconductor–electrolyte interface. That is, a cation-dominated Helmholtz layer is formed on the surface of a p-type semiconductor, while the opposite is true for an n-type semiconductor. However, the semiconductor is in a nonequilibrium state when illuminated or biased, and the quasi-Fermi level is employed to present the statistical gradient distribution of electrons ($E_{F,\,n}$) and holes ($E_{F,\,p}$) (Fig. 2c and f). The difference between $E_{F,\,p}$ and the redox potential of the HER in p-type semiconductors and the difference between $E_{F,\,n}$ and the potential of the OER in n-type semiconductors under illumination is termed "photovoltage" or "open-circuit voltage (V_{OC})" (Fig. 2c, f). In addition to irradiation, the applied bias is another nonnegligible factor contributing to the shift of the quasi-Fermi level. Both V_{OC} and the applied bias are commonly accepted to be the driving force for water splitting. However, a bias-free light-driven PEC device that can generate a sufficiently large V_{OC} under irradiation is desired to reduce or even eliminate the bias requirement.

4 Configuration of PEC Devices

The wavelengths of solar radiation are generally divided into ultraviolet (UV), visible (Vis) and infrared (IR) regions according to the sensitivity of human vision (Fig. 3a). The absorption band edge of semiconductors depends on E_g, and V_{OC} depends on the position of the quasi-Fermi level, which is also related to E_g. Therefore, the most efficient utilization of solar radiation involves achieving full-band absorption by coupling semiconductors with different band gaps under the premise that V_{OC} can drive water splitting.

According to the functions of semiconductor photoelectrodes (Fig. 3b, c and d), the configurations of PEC devices are classified into three categories. Figure 3b shows a typical H-type configuration, where the photoelectrode and electrode are separated by an ion exchange membrane (IEM), such as an anion exchange membrane (AEM), a cation exchange membrane (CEM) and a bipolar membrane (BM), which is formed by stacking an AEM and a CEM [29]. A

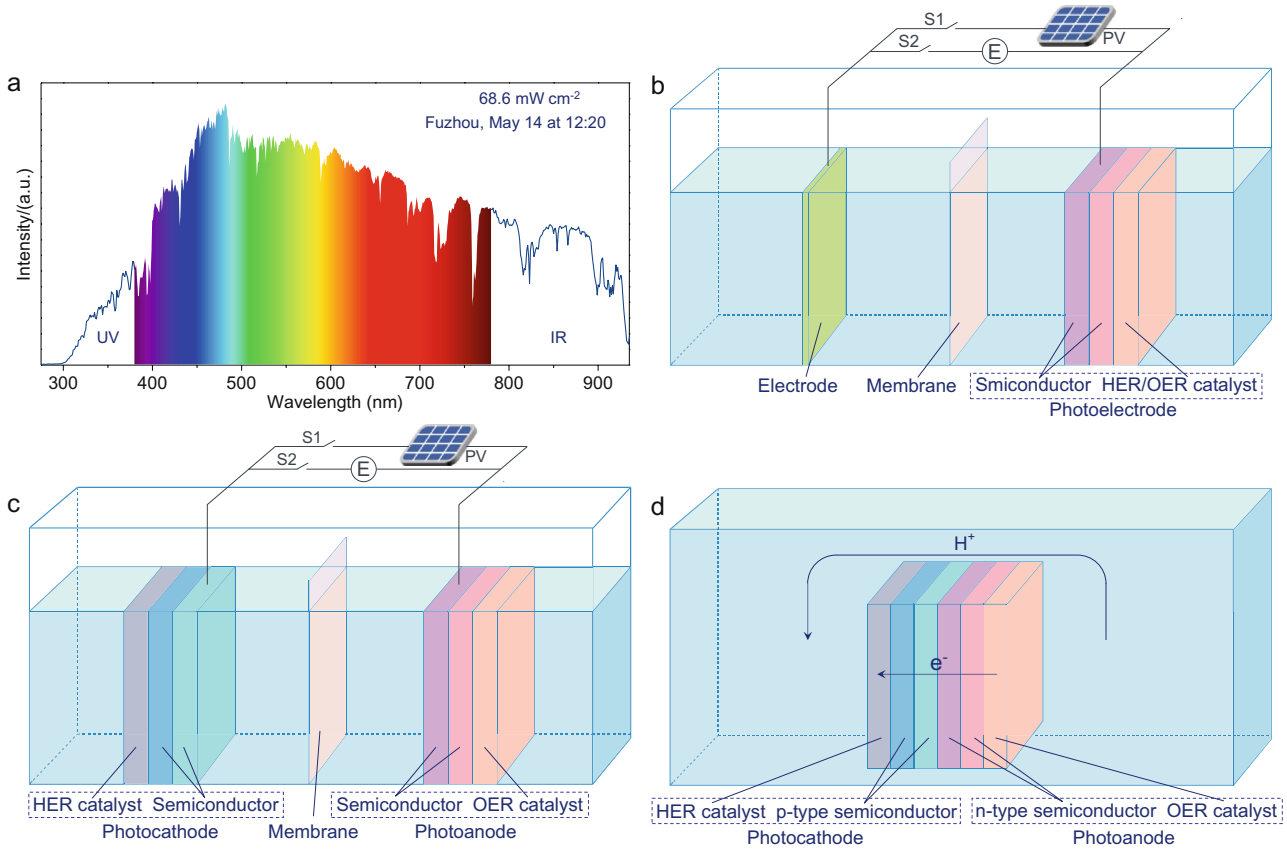

Fig. 3 Solar spectrum and APSs for solar-to-hydrogen conversion. **a** Solar spectrum and irradiance power collected in Fuzhou (26°05'N, 119°20'W) by a light intensity meter (ILT950). **b–d** Photosynthetic systems with different configurations: **b** electrode and tandem photoelectrode configuration; **c** tandem photocathode and photoanode configuration; **d** integrated tandem photosynthetic system configuration

photoelectrode can be either a photocathode for the HER or a photoanode for the OER. Notably, a photoelectrode can be a multicomponent composite or a single-component semiconductor without HER or OER cocatalysts. The photogenerated carriers transfer in opposite directions under the synergy of band bending and applied bias to achieve spatial separation. Specifically, the minority carriers in the semiconductor migrate to the photoelectrode surface for the HER or OER, while the majority carriers migrate to the counter electrode along the external circuit for the other half-reaction. The ions in the electrolyte migrate from one side to another side through an IEM, forming a closed electrochemical circuit. In addition, if the V_{OC} is insufficient to drive the entire reaction, then it needs to be compensated by applying a bias (Fig. 3b and c).

Connecting the photocathode and photoanode in series is an effective strategy to further increase V_{OC} (Fig. 3c). However, the unfavourable voltage drop caused by the IEM and the electrolyte is still inevitable. In further optimization, constructing tandem photoelectrodes in which a photocathode and a photoanode are coupled without an IEM is a superior approach (Fig. 3c and d). With the inner electric field (IEF) caused by V_{OC}, the electrons flow from the anode to the cathode inside the tandem photoelectrode, while the protons in the electrolyte rapidly migrate and supplement the cathode surface for the HER (Fig. 3c). In this configuration of PEC devices, integrating light-harvesting modules such as PVs into the tandem photoelectrode is an advanced choice to achieve bias-free light-driven water splitting. This strategy not only improves the efficiency of solar utilization but also simplifies the device structure. Therefore, many researchers are making efforts for preliminary attempts in this field [2, 30–33].

5 Evaluation Criteria for Energy Conversion of PEC Devices

For a biased PEC system, the applied biased photon-to-current efficiency (ABPE) is generally employed to evaluate the contribution of the incident light,

$$\mathrm{ABPE} = \frac{j \times \left(E_{\mathrm{redox}} - E_{\mathrm{cell\ voltage}}\right)}{P_{\mathrm{light}}} \times 100\%$$

where E_{redox} is the redox potential of 1.23 V for water splitting, j is the photocurrent (A), $E_{\mathrm{cell\ voltage}}$ is the cell voltage (V) of the PEC device, and P_{light} is the intensity (AM 1.5G, 100 mW cm^{-2}) of incident light collected by the light meter.

The solar-to-hydrogen conversion efficiency (η_{STH}) is commonly used as an indicator to evaluate the performance of PEC devices. The formula is as follows:

$$\eta_{\mathrm{STH}} = \frac{\text{Chemical energy}}{\text{Solar energy}} \times 100\% = \frac{\Delta G \times Y_{\mathrm{H_2}}}{P_{\mathrm{light}} \times S} \times 100\%$$

where ΔG is the Gibbs free energy (273.15 kJ mol^{-1}) of water splitting, $Y_{\mathrm{H_2}}$ is the yield of hydrogen (mol s^{-1}), P_{light} is the intensity (AM 1.5G, 100 mW cm^{-2}) of the incident light, and S is the irradiated area (cm^2).

The use of the photon quantum efficiency (QE) to evaluate the photon-to-chemical conversion efficiency in PEC devices is also accepted.

$$\mathrm{QE} = \frac{\text{Overall number of transferred electrons}}{\text{Number of photons}} \times 100\% = \frac{Y_{\mathrm{H_2}} \times n_{\mathrm{e}} \times N_{\mathrm{A}}}{\int_{i_{\mathrm{s}}}^{i_{\mathrm{e}}} P_i \mathrm{d}i \times S \times \frac{\lambda_i}{hc}} \times 100\%$$

where $Y_{\mathrm{H_2}}$ is the yield of hydrogen (mol s^{-1}), n_{e} represents the number of electrons ($n_{\mathrm{e}} = 2$) required to generate a hydrogen molecule, N_{A} is the Avogadro constant (6.02×10^{23} mol^{-1}), P_i (mW cm^{-2}) is the light intensity of the incident light with wavelength λ_i (nm) measured by a light meter, i_{s} and i_{e} (nm) represent the start and end wavelengths of the incident light spectrum integration, respectively, S is the illuminated area (cm^2), h is the Planck constant (6.626×10^{-34} J s), and c is the speed of light (3×10^8 m s^{-1}). Note that if incident light with a centre wavelength of λ is generated by a bandpass filter, then i_{e}, i_{s} and λ_i in the formula are all equal to λ.

The incident photon-to-current efficiency (IPCE) evaluates the water splitting performance of an electrode from the perspective of photoelectric conversion. It is commonly obtained at a fixed wavelength of incident light. The formula is as follows:

$$\mathrm{IPCE} = \frac{\text{Number of photogenerated electrons}}{\text{Number of photons}} \times 100\% = \frac{\frac{i}{\mathrm{e}} \times \frac{hc}{\lambda}}{P_\lambda \times S} \times 100\%$$

where i is the photocurrent (A), e (1.602×10^{-19} C) is the charge of an electron, h is the Planck constant (6.626×10^{-34} J s), c is the speed of light (3×10^8 m s^{-1}), λ (nm) is the wavelength of the incident light, P_λ (mW cm^{-2}) is the light intensity of the incident light measured by a light meter, and S is the irradiated area (cm^2).

The Faraday efficiency (FE) is the most commonly used evaluation criterion for electrode stability. The photocorrosion of the photoelectrode will make the FE far from 100% because not all electrons are used for water splitting. The formula for the FE is as follows:

$$\mathrm{FE} = \frac{\text{Experimental hydrogen throughput}}{\text{Theoretical hydrogen throughput}} \times 100\% = \frac{Y_{\mathrm{H_2}}}{\frac{j}{n_{\mathrm{e}} \times F}} \times 100\%$$

where $Y_{\mathrm{H_2}}$ is the experimental hydrogen throughput (mol s^{-1}), j is the photocurrent (A), n_{e} is the number of transferred electrons required to generate a hydrogen molecule ($n_{\mathrm{e}} = 2$), and F is the Faraday constant (96 485.3 C mol^{-1}).

6 Electrode Materials for the HER in PEC Devices

This section will discuss the perspectives of light-harvesting materials in photoelectrodes, HER catalysts on the surface of photoelectrodes, and innovative materials with potential applications.

6.1 Silicon-Based Materials

Silicon (Si) is abundant in the Earth's crust [34]. As a p-type semiconductor, it is not only widely used in integrated circuits in the electronics industry but also shines in the PV field of solar energy conversion. For PEC water splitting, Si has become a supermaterial due to its structural inclusiveness, a CB position of − 0.5 V (vs. the reversible hydrogen electrode (RHE)), which is more negative than the potential for hydrogen production (Si is therefore suitable for water reduction), narrow E_{g} of 1.12 eV, wide spectrum absorption, high carrier migration rates and suitable band diagrams. In theory, the photocurrent density of Si as high as ca. 44 mA cm^{-2} under 100 mW cm^{-2} irradiation surpasses that of most current photoelectrodes [35, 36]. Compared with polycrystalline silicon, monocrystalline silicon exhibits a faster photogenerated carrier transport speed and a lower recombination probability [37].

6.1.1 Surface Treatment of Silicon

However, planar Si has an inherently high reflectivity of up to 30%. In practical applications, surface treatment and

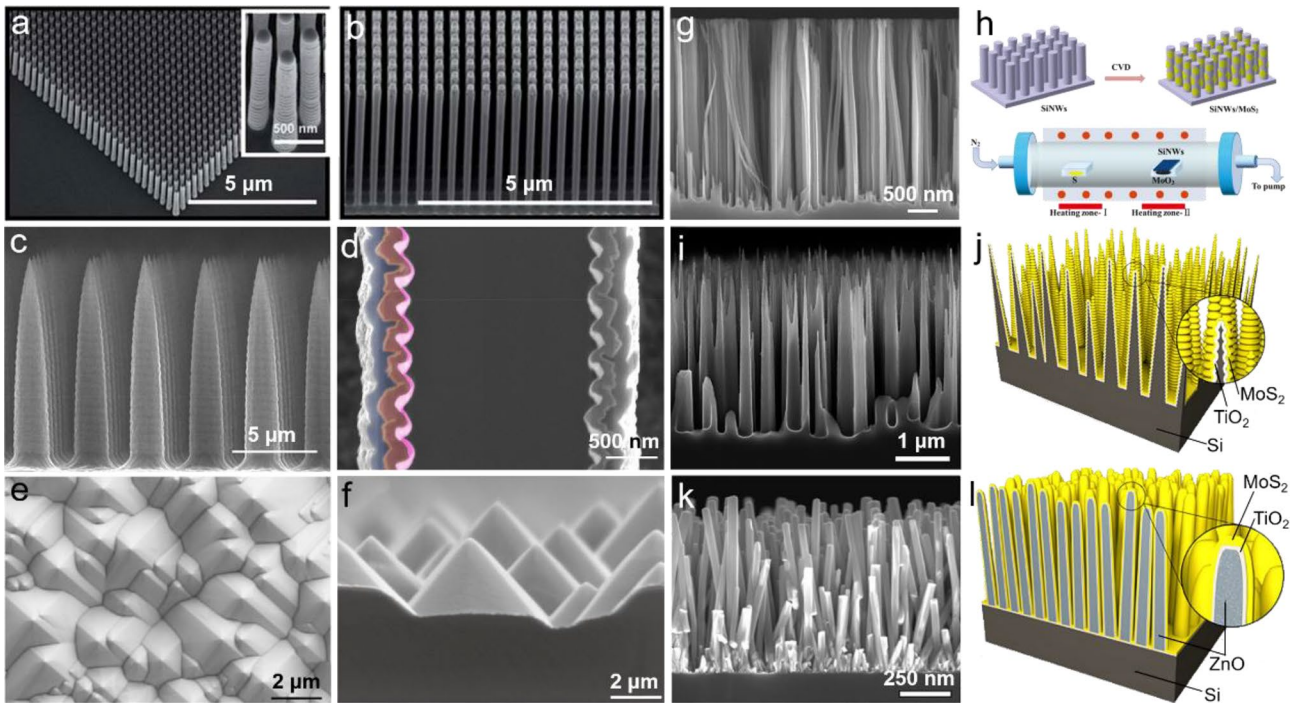

Fig. 4 Surface treatment strategy of planar silicon. Top-view images of Si NW photocathodes with lengths of **a** 2 μm and **b** 5 μm. Reprinted with permission from Ref. [40]. Copyright © 2018 The Royal Society of Chemistry. Scanning electron microscopy (SEM) images of **c** silicon microwires obtained by wet etching and **d** the completed Si microwire photocathode, ITO/Au (pink), Cu_2O (red), Ga_2O_3 (orange), and TiO_2 (blue). Reprinted with permission from Ref. [38]. Copyright © 2019 American Chemical Society. **e** Top-view and **f** cross-sectional images of bare n^+p-Si micropyramid arrays. Reprinted with permission from Ref. [47]. Copyright © 2018 Published by Elsevier B.V. and Science Press. **g** Cross-sectional SEM image of SiNW arrays. **h** Schematic of the synthesis procedures for fabricating SiNWs/MoS_2 by the CVD method. Reprinted with permission from Ref. [53]. Copyright © 2018 The Royal Society of Chemistry. **i** SEM image of the $MoS_2|TiO_2|Si_{NW}$ structure, and **j** schematic diagram of the photoelectrode architecture. **k** SEM image of the $MoS_2|TiO_2|ZnO_{NW}|Si$ structure, and **l** schematic diagram of the photoelectrode. Reprinted with permission from Ref. [54]. Copyright © 2019 American Chemical Society

antireflection coating (ARC) are widely used strategies to suppress the reflection of incident light [38, 39]. Constructing nanowires (NWs) on the surface is a universal treatment method. Liu et al. reported a vertically aligned NW array Si-based photoelectrode, which is a favourable configuration for the HER (Fig. 4a–d) [38, 40–44]. This configuration not only enhances the light absorption through multiple scattering of incident light but also decouples the light absorption and photogenerated carrier raial transmission and collection [40]. Moreover, the low photogenerated carrier fluxes caused by the high specific surface area of NWs make the photoelectrode more compatible with the loaded HER electrocatalyst compared to the planar photoelectrode [45, 46]. Liu et al. employed a top-down microfabrication technique including e-beam lithography and a subsequent deep reactive ion etching (DRIE) process, which are well established in the semiconductor industry (Fig. 4a and b) [40]. A systematic study of the structural parameters of the NWs showed that arrays with a diameter of 200 nm, a length of 1 mm and an interwire spacing of 175 nm exhibit superior HER performance [40]. Huskens et al. prepared tapered Si microwire arrays by combining DRIE with a Si slow etchant (Fig. 4c) [38]. Next, a multilayer composite photocathode with a tight bonding interface was fabricated by spin-coating, sputtering and electrodeposition (Fig. 4d) [38]. This PEC device features a photocurrent density of ca. 10 mA cm^{-2} at 0 V vs. RHE and outstanding durability over 200 h [38]. Moreover, an external quantum yield of 80% for the HER is achieved by matching the absorption band edge of the composite material [38]. Therefore, the ordered Si NWs not only ameliorate light harvesting but also serve as the foundation for the preparation of tandem photoelectrodes.

Zhang et al. prepared a silicon micropyramid structure by employing a chemical etching method to treat p-type Si (Fig. 4e and f) [47]. The micropyramid configuration is a commonly used surface treatment strategy because the enhanced roughness will make the other components of the photoelectrode and the light absorber Si closer composites [38, 48–51]. Similarly, it exhibits a broadband light-harvesting capability due to the omnidirectional surface structure [47, 52]. Combining Si, which is inert to the HER,

and materials with high catalytic activity is an effective strategy to reduce the overpotential. Hu et al. used metal-assisted chemical etching (MACE) technology to prepare high-density vertically aligned Si NWs (Fig. 4g) [53]. Then, a one-step chemical vapour deposition (CVD) method was used to directionally grow a few layers of cocatalyst MoS_2 on the surface of Si NWs to improve the HER performance (Fig. 4h) [53]. Jaramillo et al. employed a pseudo-Bosch etching process and a wet chemical deposition technique to prepare Si NWs and ZnO NWs on a Si substrate, respectively (Fig. 4i, j, k and l) [54]. The core highlight is the decoupling of the light absorber surface area and the electrocatalytic active surface area (ECSA) through the structured ZnO interface layer (Fig. 4k and l). By comparison, the effect of the absorber surface area on the photovoltage and the essential contribution of the ECSA to the HER performance were verified. The results showed that the photocathode with the ZnO NW configuration has both the electrocatalytic activity of the structured catalyst and the photoactivity of planar silicon [54].

6.1.2 Interface Protection and Passivation

Due to the active chemical properties of Si, chemical reactions or corrosion occur when it is directly placed in an electrolyte. Therefore, surface passivation is widely used to keep Si stable but without compromising its outstanding light absorption [55–60]. Liu et al. used electrochemical etching, drop casting and heat treatment processes to prepare inverted pyramid textured p-Si photoelectrodes, and then, Co_2P as both a protective layer and an HER electrocatalyst was deposited onto the p-Si (Fig. 5a) [61]. The authors stated that the macroscopically continuous but locally unevenly distributed Co_2P layer makes the light absorber (vertices) and catalytically active (top edges) sites separate spatially (Fig. 5a). With this strategy, the PEC device exhibited a photocurrent as high as ca. 35.2 mA cm^{-2} under bias-free simulated light irradiation (AM 1.5G) and catalysed hydrogen production at a current density higher than 30 mA cm^{-2} for at least 150 h without significant attenuation [61]. Because of its instability in alkaline electrolytes, Si has been studied under acidic conditions, as reported in most literature. In view of this, Huskens et al. electrodeposited metallic Ni after precisely removing the SiN_x on the top of NWs and then obtained a defect-free protective layer of NiSi after a rapid thermal annealing (RTA) process (Fig. 5b) [62]. The NiMo catalyst for the HER was electrodeposited on top of the prepared NiSi, and it was also directly deposited on the metallic Ni without the RTA process for comparison (Fig. 5b). The results showed that only the photoelectrode with NiMo deposited on NiSi has enhanced corrosion resistance in the 1 M KOH solution (1 M = 1 mol L^{-1}) and exhibits superior HER performance. In this way, the electrocatalyst on the surface can also be regarded as a protective layer for the light absorber. In addition, Wang et al. and Kim et al. presented a novel PEC architecture based on 3D pyramid-like graphene/p-Si Schottky junctions, which greatly enhances the light-harvesting efficiency and exhibits promising PEC performance for hydrogen generation. A graphene interlayer is applied between p-Si and MoP nanorods to enable fully engineered interfaces without forming a metallic secondary compound, which absorbs parasitic light and provides an inefficient electron path for hydrogen evolution. Growth on graphene-passivated silicon photocathodes has been successfully demonstrated to remarkably improve the PEC-HER performance in balance [63–65]. However, inert materials that are generally resistant to acid–base corrosion and light corrosion and that have outstanding self-stability are the first choice for the protective layer in PEC systems. To date, TiO_2 has been one of the most widely used materials for photoelectrode protection. Wang et al. reported that TiO_2 can be used as a protective layer to decouple the trade-off between Si-based photoelectrode efficiency and stability (Fig. 5c and d) [66]. The key factor stated by the authors was the graded oxygen defects of the crystalline TiO_2 protective layer. For this factor, a comparative experiment designed by the author showed that a photoelectrode with a well-crystallized and defect-free TiO_2 protective layer cannot exhibit PEC properties (Fig. 5c). In contrast, the use of black TiO_2 with oxygen defects as a protective layer led to a limiting current density of ca. − 35.3 mA cm^{-2} and stable operation at 10 mA cm^{-2} in 1.0 M KOH for at least 100 h (Fig. 5c). The author stated that there are conducting paths generated by defects, as well as suitable band alignment, in black TiO_2 that can be used as photogenerated carrier transport channels (Fig. 5d). Moreover, the authors also proposed that the protons adsorbed on the electrocatalyst Pd would spill over onto the surface of black TiO_2 for the HER. Therefore, TiO_2 as a protective layer can be considered to possibly have a nonnegligible contribution to the catalytic HER.

In addition, Ti^{3+} species induced by UV photons in TiO_2 as traps for photogenerated carriers were previously reported to possibly deteriorate the performance of the protective layer [67, 68]. Gong et al. prepared a series of protective layers on Si substrates by atomic layer deposition (ALD) and employed photoelectrochemistry and spectroscopy to conduct an in-depth study (Fig. 5e) [69]. As expected, pn^+-Si/TiO_2/Pt is similar to pn^+-Si/Pt without a protective layer, and its photocurrent density drastically drops within a few hours (Fig. 5e). However, the photoelectrode pn^+-Si/Ta_2O_5/Pt shows outstanding stability for up to 200 h, which is protected by another nearly transparent Ta_2O_5 layer with superior chemical stability and a band gap of 4.2 eV (Fig. 5e). In addition, Ta_2O_5 has been demonstrated to not only exhibit superior stability over a wider pH range as a protective layer [70] but also efficiently transport electrons from light

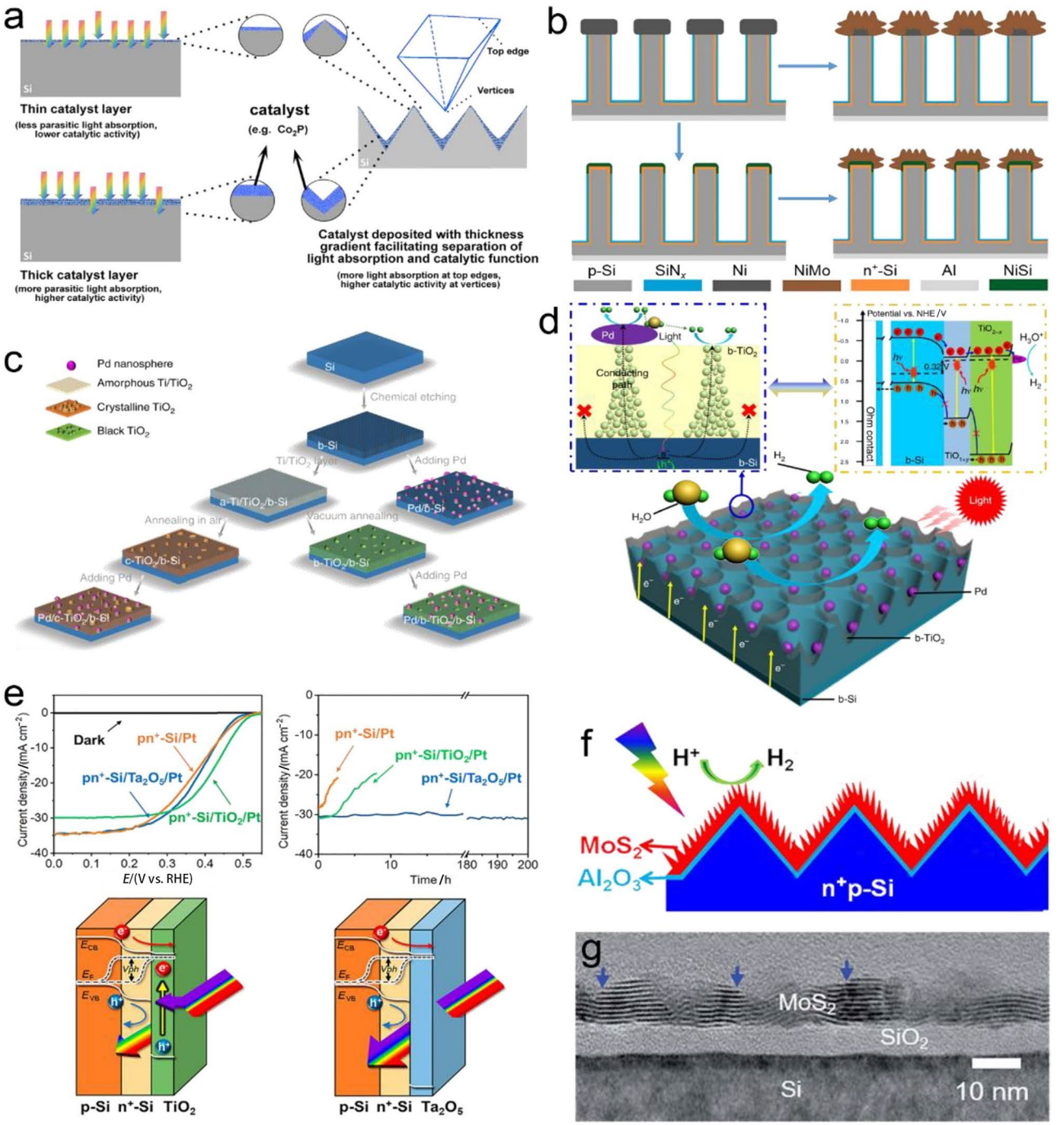

Fig. 5 Interface protection and passivation strategies of Si-based photoelectrodes. **a** Schematic illustration of the influence of catalyst loading on inverted pyramid textured p-Si. Reprinted with permission from Ref. [61]. Copyright © 2019 American Chemical Society. **b** Fabrication scheme for alkaline-stable photocathodes. Reprinted with permission from Ref. [62]. Copyright © 2018 American Chemical Society. **c** Surface protection strategies for nanoporous black Si photocathodes. **d** Schematic of the Pd nanoparticle/black TiO_2/black Si photocathode. Reprinted with permission from Ref. [66]. Copyright © 2018 The Author(s). **e** $J-V$ curves and durability for pn^+-Si/Pt, pn^+-Si/Ta_2O_5/Pt and pn^+-Si/TiO_2/Pt electrodes; band diagrams of pn^+-Si/TiO_2 and pn^+-Si/Ta_2O_5. Reprinted with permission from Ref. [69]. Copyright © 2019 American Chemical Society. **f** Integrated photocathode with the $MoS_2/Al_2O_3/n^+$p-Si configuration. Reprinted with permission from ACS [72]. Copyright © 2017 American Chemical Society. **g** TEM image of a photocathode with the MoS_2/SiO_2/Si configuration. Reprinted with permission from Ref. [74]. Copyright © 2017 The Royal Society of Chemistry

absorbers, such as Si PVs, as an electron-selective heterogeneous contact layer [71]. Shen et al. reported an Al_2O_3 protective layer with a thickness of ca. 2 nm and a MoS_2 catalyst layer with a thickness of ca. 67 nm fabricated on Si substrates by ALD and magnetron sputtering methods, respectively (Fig. 5f) [72]. The $MoS_2/Al_2O_3/n^+p$-Si photocathode exhibited a current density of 35.6 mA cm^{-2} and remarkable durability over 120 h. Among the layers, Al_2O_3 not only protects Si from corrosion but also suppresses the interface recombination of photogenerated carriers as a passivation layer [72]. However, the instability in acid–base electrolytes limits its application [73]. Kim et al. also deposited MoS_2 on a Si substrate by the ALD method and then heat-treated it at 500–700 °C to further make it crystalline (Fig. 5g) [74]. Interestingly, the heat treatment process produced a protective layer of SiO_2 with good light transmittance and an inconspicuous interface with the Si substrate (Fig. 5g). The $MoS_2/SiO_2/Si$ photocathode exhibited a photocurrent density of ca. 31 mA cm^{-2} and durability without obvious degradation within 24 h under simulated light irradiation of 100 mW cm^{-2} in 0.5 M H_2SO_4 electrolyte [72].

6.1.3 Construction of Junctions

The most commonly used strategy to improve the conductivity of pure Si (the intrinsic semiconductor) is doping with impurity atoms (the extrinsic semiconductor) [75–77]. The valence electron configuration of the host Si atom is $3s^23p^2$, while the impurity atoms are generally nonmetallic B ($2s^22p^1$) and P ($3s^23p^3$). A hole-rich p-type semiconductor will be generated when the electron acceptor B with fewer valence electrons than the host atom replaces the lattice site of Si. Conversely, electron donor P doping creates an electron-rich n-type semiconductor [78]. The p–n junction is a commonly used junction structure in the electronics industry, and it also has advantages when applied to photoelectrodes [79–82] because the internal electric field in the space-charge region (SCR, also termed the depletion region, where the diffusion of majority carriers and drift of minority carriers have reached an equilibrium) of the p–n junction contributes to the separation of photogenerated carriers. The direction of the electric field is from the n region, where holes are the minority carriers, to the p region, where electrons are the minority carriers. Liu et al. fabricated a sandwich p–i–n (p-type-intrinsic-n-type) amorphous silicon (a-Si) photoelectrode with ferrihydrite (Fh) as the hole storage interlayer and Ni as the hydrogen evolution catalyst (Fig. 6a) [83]. The authors stated that the a-Si/Fh/Ni photoelectrode achieved a record bias-free photocurrent density of ca. 15.6 mA cm^{-2} and a half-cell energy conversion efficiency of ca. 4.08% [83]. The "+" (n^+ and p^+) represents heavy doping of impurities and "−" (n^- and p^-) represents light doping in the semiconductor [84]. The generally accepted purpose of heavy doping is to reduce the barrier at the interface to achieve ohmic contact [85, 86, 87]. He et al. reported a MoS_2/p^+nn^+-Si photoelectrode for the HER with a photocurrent density of ca. 36.3 mA cm^{-2}, a half-cell solar-to-hydrogen (STH) efficiency of 5.57% and an open-circuit potential (OCP) of 0.5 V vs. RHE under AM 1.5G illumination (Fig. 6b) [88]. Tilley et al. demonstrated a $pn^+Si/TiO_2/Pt$ photocathode containing a buried junction, where TiO_2 is used as a protective layer and Pt is used as a catalyst for the HER (Fig. 6c) [89]. In this model PEC system, dual working electrode (DWE) technology was employed to systematically study the independent properties of the light absorber and electrocatalyst under operation conditions (Fig. 6c) [89]. The focus of this method was the semiconductor–electrolyte interface and the mechanism of light absorber performance degradation due to photocorrosion and other reasons. The DWE methodology can also be applied to other newly developed and more complex PEC systems based on various types of junctions [90, 91].

The multijunction structure assembled by stacking a single junction structure can enhance the output potential of the light absorber [92, 93]. Zhang et al. fabricated a tandem photocathode on textured aluminium-doped zinc oxide (AZO) with an HTO/a-SiGe:H p–i–n/Si:H p–i–n structure, in which H-doped TiO_2 (HTO) was used as the protective layer (Fig. 6d) [94]. The authors designed and optimized the photoelectrode from the aspects of the band diagram, electron transport barrier, interface ohmic loss and factors related to electron tunnelling probability, such as carrier density and depletion layer width. This work successfully found a breakthrough for the conventional trade-off between the activity and stability of Si-based PEC devices [94]. He et al. demonstrated both back-buried junction (BBJ) and spatial decoupling of absorber–electrocatalyst strategies on silicon to achieve bias-free water splitting (Fig. 6e) [95]. In the structure of the photoelectrode, SiN_x was used as an antireflection coating, and SiO_2 was used as a passivation layer (Fig. 6e). Benefiting from the tandem absorber structure design and the precise preparation of the interdigitated carrier separation path, the PEC device exhibited an absorption of 95% for the solar spectrum, a V_{OC} of ca. 1.8 V, an STH efficiency of ca. 15.6% and a photocurrent density of ca. 40.5 mA cm^{-2} [95]. In particular, this PEC system shows promise for industrial applications because multiple devices can be integrated (p^+nn^+-p^+nn^+-p^+nn^+) through an easy tin soldering connection to expand production. Mi et al. constructed a photocathode with a p^+pn^+–Si/GaN/n^+–GaN NW/Pt structure and an approximately aligned CB minimum (CBM) in the band diagram (Fig. 6e) [96]. Among the components, the authors stated that the GaN NW array not only protects Si from corrosion but also reduces the transfer resistance of charge carriers [95]. Furthermore, the PEC device at that time exhibited the highest ABPE of

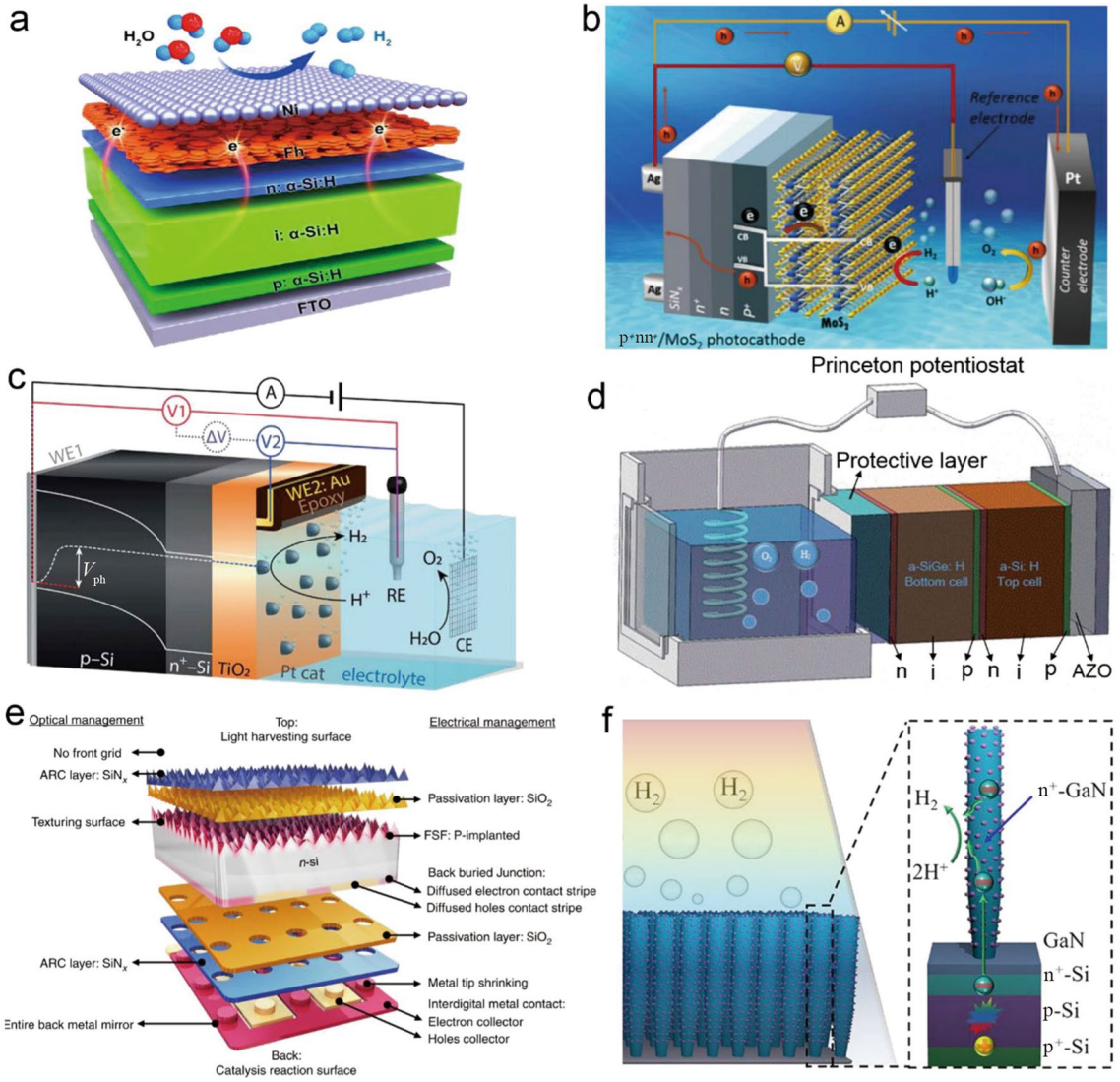

Fig. 6 Construction of junctions commonly used in Si-based photocathodes. **a** An a-Si/ferrihydrite(Fh)/Ni photocathode. Reprinted with permission from Ref. [83]. Copyright © 2021 Wiley–VCH GmbH. **b** Schematic illustration of the MoS_2-integrated Si photocathode. Reprinted with permission from Ref. [88]. Copyright © 2019 Optical Society of America under the terms of the OSA Open Access Publishing Agreement. **c** DWE configuration used during PEC measurements with a $pn^+Si/TiO_2/Pt$ photocathode. Reprinted with permission from Ref [89]. Copyright © 2018 The Royal Society of Chemistry. **d** Schematic device structure of the a-Si:H/a-SiGe:H tandem photocathode with the protective layer. Reprinted with permission from Ref. [94]. Copyright © 2016 The Royal Society of Chemistry. **e** Schematic of the components of the BBJ cell. Reprinted with permission from Ref. [95]. Copyright © 2020 The Author(s). **f** Schematic of the n^+-GaN NW/n^+-p Si photocathode. Reprinted with permission from Ref. [96]. Copyright © 2018 American Chemical Society

approximately 10.5% among all current Si-based photocathodes and outstanding stability up to 120 h at a photocurrent density of approximately 35 mA cm^{-2}.

6.2 Cuprous and Copper Oxide

Among all the current p-type oxide photocathode semiconductors, Cu-based semiconductors are promising materials because they exhibit superior performance in PEC water splitting [96]. Furthermore, cuprous (Cu_2O) and copper oxide (CuO) are more advantageous due to their low production cost and technical threshold compared with Si-based materials. The CB positions of Cu_2O and CuO are at −0.7 and −0.1 V (vs. RHE), respectively. Compared with hydrogen production, they have a more negative voltage and are suitable for water reduction. In addition, the high photoactivity and abundance make them competitive [97–99]. Among them, Cu_2O exhibits E_g of ca. 2.1 eV, a theoretical photocurrent density of ca. 14.7 mA cm^{-2} and an STH conversion efficiency of ca. 18.7% under simulated light irradiation of AM 1.5G [100, 101]. Generally, the use of surface conformal protective coatings, including stable oxides [80,

102], films [103–105] and polymers [106–108], is a favourable approach to suppress the poor stability of Cu_2O [95]. For CuO, many researchers believe that its E_g is between 1.4 and 1.7 eV, so it can absorb a large proportion of the solar spectrum [109, 110]. A joint experimental and theoretical study by Pierson et al. accurately proved that CuO has direct E_g of 1.46 eV [111]. The research on the application of CuO to solar-driven water splitting is not comprehensive [112–115]. Li et al. prepared a Cu_2O photoelectrode with a conformal protective layer of CuO through straightforward one-step fast annealing of copper foil in a H_2–O_2 flame (ca. 1 300 K) (Fig. 7a) [116]. Researchers performing similar works using CuO to protect Cu_2O believe that this configuration has an appropriate band alignment that is conducive to the transport of photogenerated carriers [117–122]. The proportion of each layer in the composite Cu/Cu_2O/CuO photocathode with a sandwich structure depends on the annealing time (Fig. 7a and b). The intimate junction is composed of the (110) plane of Cu_2O and the (111) plane of CuO [116]. The authors stated that in the annealing time range of 0–10 s, the photocurrent exhibits an upward trend with the thickness of CuO (Fig. 7b). However, a thicker CuO negatively affects the light absorption of Cu_2O when annealed for 15 s, resulting in a decrease in the photocurrent (Fig. 7b). The main challenge faced by CuO as a protective layer here is the inherent photocorrosion in an aqueous solution [113, 123]. Specifically, CuO will be reduced to Cu under the joint effects of photogenerated electrons and protons [124]. The reason is that the electrochemical reduction potentials from CuO to Cu_2O and from Cu_2O to Cu are both located in the band gap of CuO. The widely accepted effective strategy to suppress photocorrosion is to avoid direct contact between the light absorber and protons in the electrolyte.

Tielly et al. confirmed that the FE of the HER for the bare CuO thin-film photocathode at 0.4 V vs. RHE is ca. 0.01% in a 1 M phosphate buffer (pH = 7) under chopped irradiation of simulated AM 1.5G (100 mW cm^{-2}) [125]. That is, the photocurrent of the unprotected CuO photocathode is mainly from the photocorrosion and degradation of the photoelectrode rather than the HER. Tielly et al. also demonstrated an optimized high-efficiency CuO photocathode with a classical TiO_2 protective overlayer featuring an n-type CdS buffer layer that can form a buried p–n junction with the photoabsorber (Fig. 7c) [125]. The CuO/CdS/TiO_2/Pt photocathode with a favourable band alignment exhibited a superior performance (Fig. 7d) and a nearly 100% hydrogen evolution FE [125]. This configuration achieves effective suppression of photocorrosion, which is attributed to the powerful extraction of minority carriers in p-type CuO by the integrated junction of n-type CdS.

Since a seminal benchmark strategy of using the ALD method to prepare a protective overlayer for preventing Cu_2O photocorrosion was reported in 2011 [98], Grätzel and others subsequently carried out systematic research on optimization of the Cu_2O photocathode performance. Specifically, the stability of the Cu_2O photocathode was further improved by utilizing a thinner TiO_2 protective overlayer and the hydrogen evolution electrocatalyst RuO_x [126]. After that, they developed a coaxial Cu_2O NW array photocathode based on the surface p–n junction with a remarkable photocurrent density of 10 mA cm^{-2} at the RHE potential [127]. Benefiting from the development of Cu_2O PV devices, Ga_2O_3 was introduced as a superior surface multifunctional layer [128–130]. Among all the current Cu_2O-based photocathodes, many studies have focused on the configurations of Cu_2O/AZO/TiO_2 [131–137] and Cu_2O/Ga_2O_3/TiO_2 [89, 138, 139–142]. Generally, a planar photoelectrode has difficulty reconciling the depth of light absorption and diffusion length of minority carriers [127]. In view of this, Luo et al. demonstrated an efficient photocathode featuring coupling of coaxial NWs and a buried junction (Fig. 7e–h) [125]. Specifically, the authors stated that the radial heterojunction is beneficial to both enhancement of light absorption and transport of photogenerated carriers. Compared with AZO, the CB edge of Ga_2O_3 is close to that of Cu_2O in band alignment (Fig. 7e), which is beneficial for reducing the interface recombination and improving the photovoltage output (ca. 1 V vs. RHE) (Fig. 7f). A bias-free water splitting tandem system was constructed by using a Cu_2O photocathode (Cu/Cu_2O/Ga_2O_3/TiO_2/NiMo) coupled with a state-of-the-art molybdenum-doped $BiVO_4$ photoanode and achieved a record STH conversion efficiency as high as ca. 3%, rivalling the current all-oxide device (Fig. 7g). The authors stated that the stable operation of the tandem system for more than one week in alkaline electrolytes should be attributed to the superior durability of the photocathode (Fig. 7h).

Gold has been widely employed as the back contact of Cu_2O photocathodes due to its appropriate work function and VB edge [125, 126]. Compared with the base material nickel oxide, which is specialized for hole transport, the precious metal Au will result in a considerable amount of recombination since it is not a hole-selective contact [138]. On these grounds, Hagfeldt et al. developed an effective hole transport layer (HTL) of CuSCN for a Cu_2O photocathode (Fig. 7i) [138]. Compared with the conventional photocathode, the ameliorated photocathode with defective CuSCN (CuSCN-D) is uncompetitive in the onset potential of ca. 1 V vs. RHE and the current density of ca. 6.6 mA cm^{-2} at 0 V vs. RHE, but it exhibits a superior fill factor (Fig. 7j). An in-depth study of the band diagram revealed that the band-tail states, which reduce the hole injection barrier rather than shift the Fermi level via heavy doping, allow holes to be transported smoothly [138]. Meanwhile, the difference in the CB edges between Cu_2O and CuSCN-D as high as 2 eV results in a very large barrier for electron injection into CuSCN-D and inhibits recombination of photogenerated

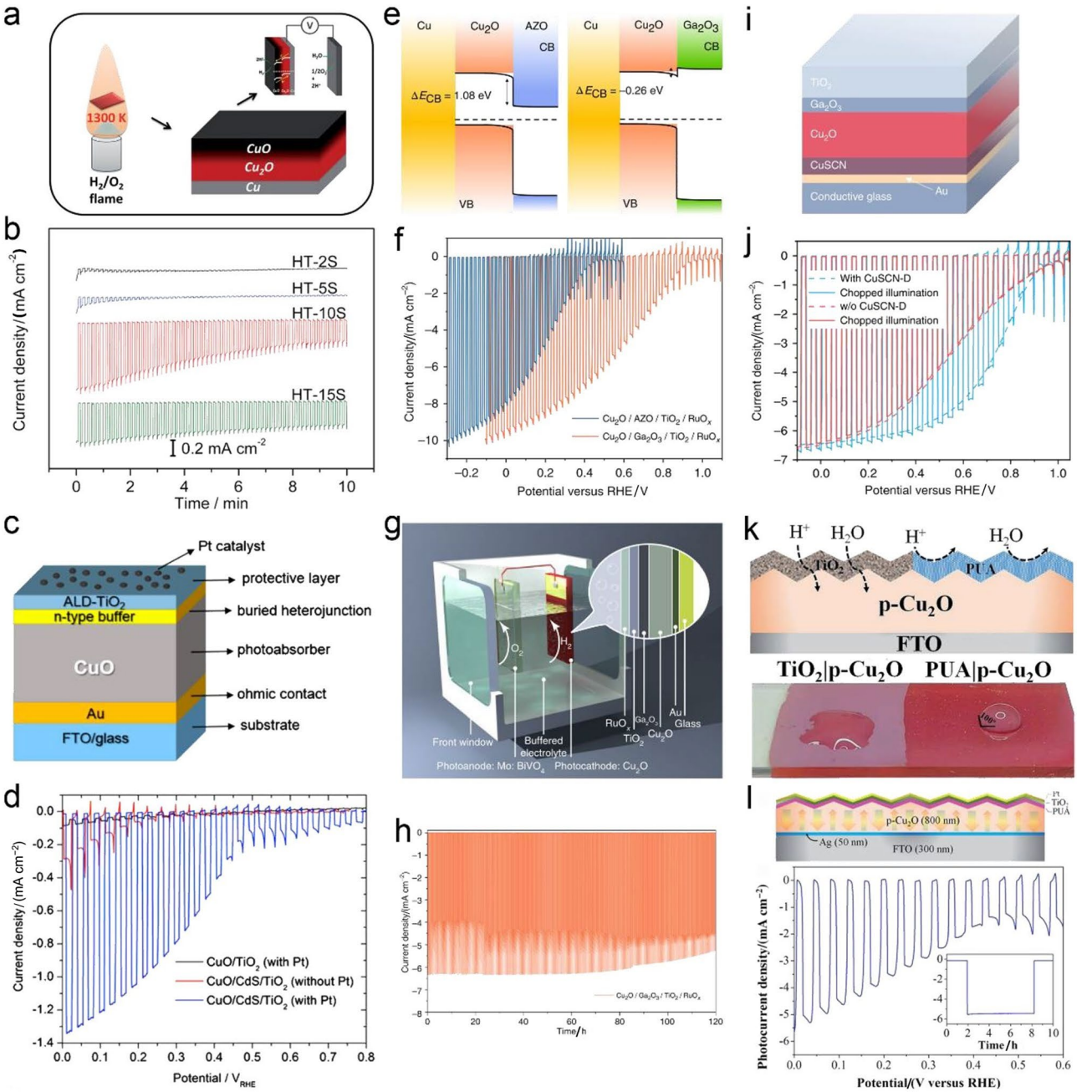

Fig. 7 Architecture, band diagram and performance of Cu-based photocathodes. **a** Preparation of a Cu_2O/CuO composite photocathode. **b** Current decay curves of composite Cu_2O/CuO photocathodes. Reprinted with permission from Ref. [117]. Copyright © 2015 The Royal Society of Chemistry. **c** The structure of a photocathode is related to the function of each layer. **d** Current density–potential curves of CuO/TiO_2 CuO/CdS/TiO_2 photocathodes. Reprinted with permission from Ref. [124]. Copyright © 2017 American Chemical Society. **e** Equilibrium band edge diagrams of Cu_2O/AZO and Cu_2O/Ga_2O_3 heterojunctions. **f** *J*–*E* response for Cu_2O-based photocathodes. **g** Illustration of the all-oxide tandem solar water splitting device. **h** Stability test of the photocathode at 0.5 V vs. RHE with chopped illumination. Reprinted with permission from Ref. [130]. Copyright © 2018 Macmillan Publishers Limited, part of Springer Nature. **i** Schematic diagram of the CuSCN-incorporated Cu_2O photocathode. **j** *J*–*E* responses of Cu_2O photocathodes with or without the CuSCN-D layer. Reprinted with permission from Ref. [137]. Copyright © 2020 The Author(s). **k** Schematic illumination of the TiO_2 and polyurethane acrylate (PUA)-protected Cu_2O photocathode. **l** Schematic illumination of the multilayered Cu_2O photocathode and *J*–*E* characteristics. Reprinted with permission from Ref. [142]. Copyright © 2019 The Royal Society of Chemistry

carriers [137]. Therefore, the construction of barrier-free energy level channels in the reciprocal space (*k*-space) for majority and minority carrier reverse transmission in the photoelectrode is the key factor for further improvement of the PEC performance.

Among all the current technologies for preparing inorganic oxide protective layers, the light absorber Cu_2O cannot be effectively protected for a long period of time. There are two main reasons: (i) the "penetration effect" formed by the island growth of the protective layer makes the absorber partially unprotected; (ii) the electrolyte and protons can reach the surface of the absorber via the micropores and grain boundaries through the "capillary effect". For this reason, Shao et al. reported a compact macromolecular polymer (solid polyurethane acrylate, PUA) as a hydrophobic layer, which was employed to prevent Cu_2O inactivation (Fig. 7k) [142]. Compared with classical TiO_2, PUA shows extreme hydrophobicity with a contact angle up to 100° (Fig. 7k). The multilayered Cu_2O photocathode with the configuration of Pt/n-TiO_2/PUA/p-Cu_2O/Ag exhibited an enhanced photocurrent density of ca. 5.5 mA cm^{-2} at 0 V vs. RHE and an IPCE peak of 68.3% at 415 nm (Fig. 7i) [142]. In addition, the retained 98% durability after 6 h highlights the promising application of this strategy in the further development of PEC systems for solar water splitting.

6.3 Sulphides and Selenides

The tunability of the band gap is the key to accurately designing a solar water splitting system with superior energy conversion efficiency. Benefiting from the development of the close cousins of kesterite Cu_2ZnSnS_4 (CZTS) and chalcopyrite $CuIn_{1-x}Ga_{1-x}Se_2$ (CIGS) with flexible crystal structures, the continuously tuneable band gap has been widely used in PEC systems [143–147]. In addition to the low toxicity and earth abundance that make CZTS competitive, the band gap is ca. 1.5 eV, with a CB position of − 0.8 V (vs. RHE), which is more negative than the hydrogen production voltage, rendering an ideal open-circuit photovoltage and a higher photocurrent for solar water splitting [148]. Since Domen and coworkers first demonstrated a CZTS-based photocathode in 2010 [149], its superior solar water splitting efficiency has attracted the attention of many scientists and led to follow-up studies. Sivula et al. reported that the incorporation of an AZO coating enhances the stability of the photocathode [150]. Subsequently, Domen et al. employed a feasible electroplating annealing method to prepare a photocathode by depositing CZTS onto Mo mesh, revealing that the photocathode with irregular hollow column CZTS exhibits the highest photocurrent density [149]. Ikeda et al. reported a photocathode with the configuration of Pt/In_2S_3/CdS/Cu_2ZnSnS_4, revealing that the deposition of In_2S_3 significantly enhances the stability [151]. Jooho Moon et al. developed a hybrid ink method via a molecular chemistry-controlled technique to prepare CZTS thin films with a conformal dual coating of TiO_2/CdS and a Pt electrocatalyst, achieving a remarkable photocurrent density as high as 13 mA cm^{-2} at − 0.2 V vs. RHE under simulated sunlight illumination (AM 1.5G) [151]. However, the significantly degenerated durability within 1 h needs to be further optimized. Minegishi and coworkers attempted to partially substitute Zn in CZTS with Cd and obtained a photocathode with the Pt/Tio/CdS/$Cu_2Cd_{0.4}Zn_{0.6}SnS_4$ configuration, delivering a superior photocurrent density as high as 17 mA cm^{-2} at 0 V vs. RHE under simulated sunlight irradiation of AM 1.5G [152]. However, the introduction of environmentally unfriendly toxic Cd is not conducive to its practical application. In addition, Mitzi and coworkers fabricated a Pt/TiO_2/CdS/$Cu_2BaSnS_{4-x}Se_x$ ($x \approx 3$) stacked film photocathode derived from CZTS, achieving a photocurrent density of ca. 12.1 mA cm^{-2} at 0 V vs. RHE under simulated sunlight of AM 1.5G [153].

At present, surface protection and passivation are key strategies to improve the performance of CZTS-based photocathodes. Jiang et al. developed a surface photocorrosion-resistant passivation film of HfO_2 with a thickness of 6 nm to enhance the PEC stability of CdS/Cu_2ZnSnS_4, revealing a photocurrent stability of over 10 h and a retained half-cell STH conversion efficiency of 2.7% [154]. After that, the authors constructed a bias-free tandem PEC system for solar water splitting based on a Pt/HfO_2/CdS/Cu_2ZnSnS_4 photocathode and a conventional $BiVO_4$ photoanode (Fig. 8a), achieving a full-cell STH conversion efficiency of approximately 1% and a long-term durability of over 10 h [154]. More specifically, an operating point with a photocurrent of approximately 0.64 mA and a cell voltage of approximately 0.57 V was obtained for the tandem system at the crossing point of two independent linear sweep voltammetry (LSV) curves (Fig. 8b) [154]. Following this research, Jiang et al. recently demonstrated a reformative bias-free integrated tandem PEC device with the configuration of a Pt-HfO_2/CdS/HfO_2/CZTS photocathode and a $BiVO_4$ photoanode for solar water splitting (Fig. 8c), revealing an STH conversion efficiency of approximately 3.7% and a superior durability of at least 20 h under simulated sunlight AM 1.5G irradiation [155]. Similarly, an operating point with a current density of approximately 2.6 mA cm^{-2} and a cell voltage of approximately 0.58 V was obtained at the crossing point of two individual LSV curves (Fig. 8d). Moreover, the CZTS-based photocathode exhibited a long-term durability of over 24 h and a remarkable ABPE of approximately 7.3%. This exemplary PEC device highlights the promising application potential of the CZTS light absorber [148, 156–158].

Benefiting from the in-depth study of CIGS-based solar cells, a record power conversion efficiency of over 21.5% was revealed [159]. Moreover, Mannstadt et al. reported

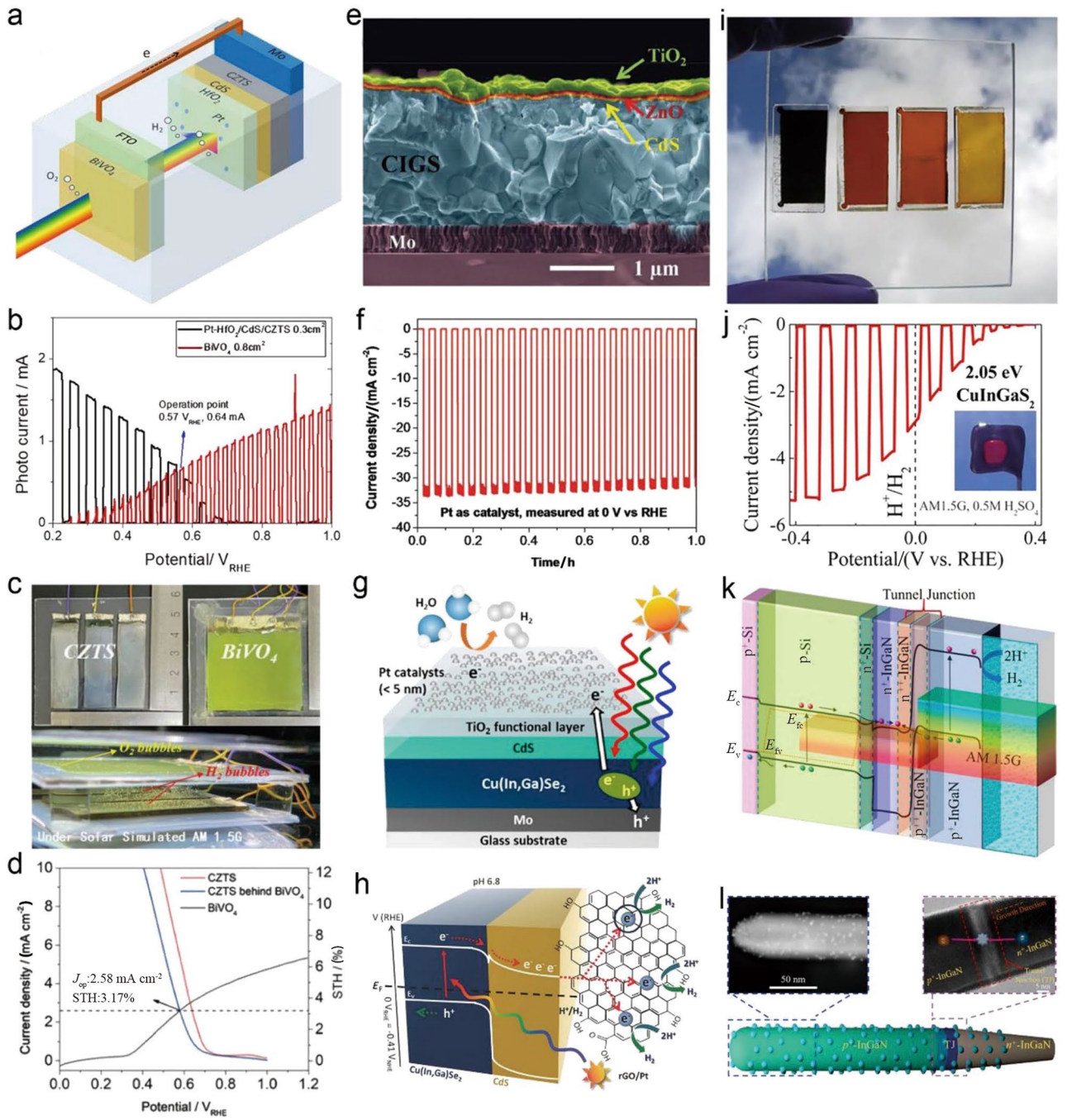

Fig. 8 Architecture and performance of group III and IV semiconductor-based photocathodes. **a** Diagram of the Pt/HfO_2(H6)/$BiVO_4$ tandem device for bias-free solar water splitting. **b** $J-E$ curves of the H6 photocathode and the $BiVO_4$ photoanode. Reprinted with permission from Ref. [154]. Copyright © 2018 American Chemical Society. **c** Cu_2ZnSnS_4(CZTS)–$BiVO_4$ tandem device under AM 1.5G solar simulated illumination. **d** *J–E* curves of series photoelectrodes. Reprinted with permission from Ref. [155]. Copyright © 2021 The Royal Society of Chemistry. **e** SEM image of the $CuIn_xGa_{1-x}Se_2$ photocathode. **f** Stability of the $CuIn_xGa_{1-x}Se_2$ photocathode with the overlayer and Pt catalyst coatings. Reprinted with permission from Ref. [168]. Copyright © 2015 WILEY–VCH Verlag GmbH & Co. KGaA, Weinheim. **g** Schematic illustration of the Cu(In,Ga)Se_2/CdS/TiO_2/Pt photocathode. Reprinted with permission from Ref. [169]. Copyright © 2017 American Chemical Society. **h** Proposed model and band diagram describing the working principles of the Cu(In,Ga)Se_2/CdS/rGO/Pt photocathode. Reprinted with permission from Ref. [170]. Copyright © 2018 WILEY–VCH Verlag GmbH & Co. KGaA, Weinheim. **i** Optical image of $CuGaSe_2$ (first) and $Cu(In_xGa_{1-x})S_2$ (the second to the fourth). **j** LSV measurement of a $CuInGaS_2$ photocathode. Reprinted with permission from ACS. [165]. Copyright © 2019 American Chemical Society. **k** Band diagram of the p^+-InGaN/TJ/n^+p-Si photocathode. **l** Schematic of the InGaN NW with Pt and Al_2O_3, the scanning transmission electron microscopy-high-angle annular dark-field (STEM-HAADF) image of the top p^+-InGaN segment, and the bright-field STEM image of the TJ region. Reprinted with permission from Ref. [180]. Copyright © 2020 American Chemical Society

another remarkable CIGS-based solar cell whose short-circuit photocurrent density reaches 80% of the theoretical limit [160]. The superior light absorption performance and tuneable band edge make CIGS promising for application in PEC systems for solar water splitting [161–163]. Gaillard et al. demonstrated a bare CIGS-based PEC device without an electrocatalyst, which exhibited a photocurrent density that rivalled that of the solar cell counterpart and an FE of approximately 86% [164]. Theoretically, the CIGS-based PEC device with a band gap of 1.13 eV should exhibit a maximum STH conversion efficiency of 17.5% and an outstanding photocurrent density of 42.6 mA cm^{-2} [165]. However, in previous reports, the CIGS-based standalone device with a coplanar architecture exhibited an STH conversion efficiency of approximately 3.7%–10% [166, 167]. Therefore, optimization of the photoelectrode configuration and interface protection are necessary to further improve the performance. Luo et al. demonstrated a remarkable PV-PEC tandem water splitting device with an organic–inorganic metal halide perovskite solar cell and a $Pt/TiO_2/ZnO/CdS/CIGS$ photocathode (Fig. 8e), achieving an STH conversion efficiency of approximately 6% [168]. Moreover, the multilayer photocathode exhibited stability for up to 1 h, but with significant degradation (Fig. 8f). Afterwards, Shin et al. reported a similar photocathode without ZnO (Fig. 8g), highlighting the positive effects of the n-type buffer layer (CdS) between CIGS and protective layer TiO_2 in enhancing the solar water splitting performance [169]. The shedding caused by poor electrocatalyst adhesion is an important factor for device performance degradation [169]. In view of this, Nam et al. introduced a reduced graphene oxide (rGO) layer to the photocathode as an electrocatalyst binder, revealing the multiple beneficial roles of rGO (Fig. 8h) [170]. More specifically, rGO not only contributes to electron transfer to the Pt electrocatalyst due to its superior in-plane conductivity but also anchors Pt to prevent agglomeration and shedding via defect sites and functional groups. Furthermore, rGO protects CdS and CIGS from photocorrosion in an aqueous electrolyte as a protective layer and then enhances the stability of the photocathode. Moreover, Choy et al. employed an environmentally friendly and cost-effective nonvacuum electrostatic spray-assisted vapour deposition method to prepare a CIGS photocathode. With cobalt sulphide (Co–S) as an electrocatalyst, a photocurrent density of approximately 19 mA cm^{-2} at − 0.34 V vs. RHE was achieved on this photocathode [171]. Yoon et al. confirmed that the photocurrent density depending on the Pt load can reach 37 mA cm^{-2} at − 0.7 V vs. RHE and attributed the outstanding performance to the effective separation of photogenerated carriers caused by the surface p–n junction [146]. Domen et al. developed a solid solution of $(ZnSe)_{0.85}(CIGS)_{0.15}$ prepared by a coevaporation method as a photocathode, delivering a photocurrent density of approximately 7.1 mA cm^{-2} and an STH conversion efficiency of 0.91% after coupling with a $BiVO_4$ photoanode [172]. After that, Nishikiori et al. highlighted the multiple functions of the Pt/TiO_2 layer in the $Pt/TiO_2/CdS/ZnSe:CIGS$ photocathode, including prevention of photocorrosion, surface wettability for hydrogen production and dependence of the surface potential on the Pt content [173]. Recently, a study on the optimal particle size of ZnSe:CIGS that composes the photocathode was reported by Nishikiori and coworkers, revealing a particle size-dependent solar water splitting performance that can be attributed to the synergistic effect of the specific surface area, carrier density and bulk resistance [174].

Chalcopyrite $CuInGaS_2$, whose crystal structure and optical properties are similar to those of CIGS, is also a superior light absorber with a flexible structure. Experiments and theoretical calculations have confirmed that $CuInGaS_2$ can achieve a tuneable band gap from 1.54 eV ($CuInS_2$) to 2.46 eV ($CuGaS_2$) [67, 68]. Gaillard and coworkers developed a feasible close-space sulphurization method to fabricate $Cu(In,Ga)S_2$ from CIGS precursors on FTO substrates at low temperature [165]. They obtained a series of $Cu(In,Ga)S_2$ with a variable band gap from approximately 2 to 2.5 eV by tuning the content of In and Ga in CIGS precursors (Fig. 8i). Among all the obtained samples, bare $CuInGaS_2$ with a band gap of 2.05 eV and a thickness of 800 nm exhibited a superior performance, achieving a saturation photocurrent density of approximately –5.2 mA cm^{-2}, corresponding to 38% of the theoretical limit [165]. Analogous to CIGS, if protective layers to prevent photocorrosion and heterojunctions that facilitate carrier separation and minority carrier transfer are constructed on $CuInGaS_2$, then its performance may be further optimized [175]. In addition, the optical band gap is approximately linearly dependent on the Ga or In content.

The InGaN absorber is another promising candidate material for photoelectrodes because of its composition-dependent tuneable band gap (0.6–3.4 eV) [176]. In particular, InGaN nanorods theoretically exhibit a superior STH conversion efficiency of approximately 27%, a shorter minority carrier diffusion distance and appropriate band edge levels for solar water splitting [177–179]. Mi et al. developed a double-junction photocathode with the configuration of $Al_2O_3/Pt/p^+p^{++}n^{++}n^+$–InGaN/$n^+pp^+$–Si (Fig. 8k), where n^{++}/p^{++} InGaN is the tunnel junction (TJ) (Fig. 8k and l) [180]. More specifically, p-type InGaN containing the TJ was monolithically integrated onto the bottom p–n junction of Si with a conformal surface passivation layer of Al_2O_3 and an electrocatalyst of Pt [180]. The authors stated that the top p^+–InGaN segment, TJ and surface modification promote electron extraction and reduce the recombination of photogenerated carriers [180]. Moreover, the double-junction photocathode exhibited a bias-free photocurrent of

approximately 8.4 mA cm^{-2}, an STH conversion efficiency of approximately 10.3% and a long-term durability of at least 100 h under simulated sunlight AM 1.5G irradiation in the 0.5 M H_2SO_4 electrolyte.

The p-type semiconductor $CuIn(S_{1-x}Se_x)_2$ derivative series of chalcopyrite $Cu(In,Ga)(S,Se)_2$ (CIGSSe) also exhibit a superior tuneable band gap and excellent light absorption properties [181–185]. Generally, the flat band potential derived from Mott–Schottky analysis and the VB spectrum obtained from X-ray or UV photoelectron spectroscopy (XPS or UPS) are used to determine the thermodynamic band edge of a semiconductor. Recently, Bocarsly and coworkers found that the flat band potentials derived from the two techniques of photocurrent onset under chopped-light irradiation and Mott–Schottky analysis are in good agreement for the $CuIn(S_{1-x}Se_x)_2$ semiconductor series (Fig. 9a) [186]. Calculating the band structure based on first principles is a commonly used method for material property prediction. However, compared to experimental facts, theoretical calculations generally offer a smaller band gap, and the positions of the Fermi level and the vacuum level are not accurate. The photocurrent onset technique has universal significance for quick, cost-effective and accurate determination of the band edge. In Fig. 9a, the variation in the CB edge is small, and the VB edge depends on the ratio of anions, delivering edges that all possess appropriate energetics for the thermodynamic requirement of water splitting [186]. However, the $CuIn(S_{1-x}Se_x)_2$ series exhibit superior HER performance when $x = 0.4$, indicating kinetic limitations. In view of this, according to the Gärtner model [187], the authors proposed a probability of the diffusion theoretical model ($P_D = e^{-b/L_n}$) related to the minority carrier diffusion length (L_n) and initial distance b (under illumination, R1 is the SCR, R2 is the diffusion region, and R3 is the dark region) (Fig. 9b) [187]. Generally, the R1 width decreases as the majority carrier concentration increases, and the decrement is ΔR1 in Fig. 9b, resulting in a decrease in P_D. The reason is attributed to photogenerated carrier recombination. Therefore, the performance of the photocathode for solar water splitting can be directly influenced by the majority carrier concentration.

In addition, the surface photovoltage (SPV) spectra represent the separation of photogenerated carriers in space [188]. Zhou et al. employed SPV technology to clarify the mechanisms of the NiO hole transfer layer and NiS catalyst in a photocathode with the $NiS/CuInS_2/NiO$ configuration (Fig. 9c) [189]. In their study, the positive (negative) signal of SPV spectra represents the photoinduced holes (electrons) in the bulk reaching the irradiation surface of the photocathode [189]. Back illumination showed an enhanced positive signal after introducing the NiO layer, indicating that $CuInS_2/NiO$ achieved effective charge separation (Fig. 9d). Similarly, front illumination exhibited a typical feature of p-type semiconductors in that the minority carriers (electrons) transferred to the NiS catalyst, while $NiS/CuInS_2/NiO$ showed a superior SPV compared to the other configurations (Fig. 9d). Note that this SPV technology criterion is only applicable to the study of a single solid photoelectrode and not to the two- or three-electrode configuration in a liquid electrolyte. In addition to NiO, FeOOH can also transport holes generated by the light absorber. Moreover, surface modification of $CuInS_2$ is also an effective method to improve the solar water splitting performance. Among all the reports, CdS and In_2S_3 are most commonly used as surface modification layers for chalcopyrite [190–193]. Ikeda et al. reported the band diagram of $CdS/CuInS_2$ (cliff–type CB offset) and $In_2S_3/CuInS_2$ (notch–type CB offset) heterojunctions, revealing that interface recombination is suppressed at the notch–type junction of $In_2S_3/CuInS_2$, which is favourable for solar water splitting [191]. CdS [193–196], In_2S_3 [197, 198], CuS_2 [199, 200], MoS_2 [201], SnS [202, 203], WS_2 [204], ReS_2 [205, 206], $CoSe_2$ [207] and $CdSe_2$ [208, 209] are widely used in photocathodes as modification layers, electrocatalysts or light absorbers. In particular, MoS_2 has attracted much attention as an excellent and cost-effective hydrogen evolution electrocatalyst that is most likely to replace state-of-the-art precious Pt [204].

Domen et al. demonstrated a photocathode with the typical $Pt/CdS/CuGaSe_2$ configuration [151, 210], achieving enhanced photocurrent density and onset potential after introducing the CdS surface modification layer and outstanding durability over 10 days (Fig. 9e) [151]. They proposed two reasons for the improved performance of $Pt/CdS/CuGaSe_2$. One is that the increased thickness of the SCR promotes the separation of photogenerated carriers, and the other is that the constructed p–n junction allows the minority carriers (electrons) in $CuGaSe_2$ to selectively diffuse into CdS (Fig. 9f) [151]. The nontoxic and cost-effective light absorber antimony selenide (Sb_2Se_3) exhibits a theoretical photocurrent density of approximately 40 mA cm^{-2} and a band gap of 1.2 eV [211].

Since Tang et al. successfully fabricated thin-film solar cells based on Sb_2Se_3 light absorbers [212–214], Sb_2Se_3 as a PEC photocathode for solar water splitting has achieved notable developments. Recently, Zhu et al. employed an antiphotocorrosive CdS/TiO_2 bilayer to enhance the performance of the Sb_2Se_3 photocathode, achieving a photocurrent density of approximately 8.6 mA cm^{-2} at 0 V vs. RHE and durability over 10 h under simulated sunlight AM 1.5G irradiation [215]. In addition, use of earth-abundant MoS_x as an electrocatalyst to replace precious Pt was reported by Tielly and Moon et al., resulting in a remarkable photocurrent

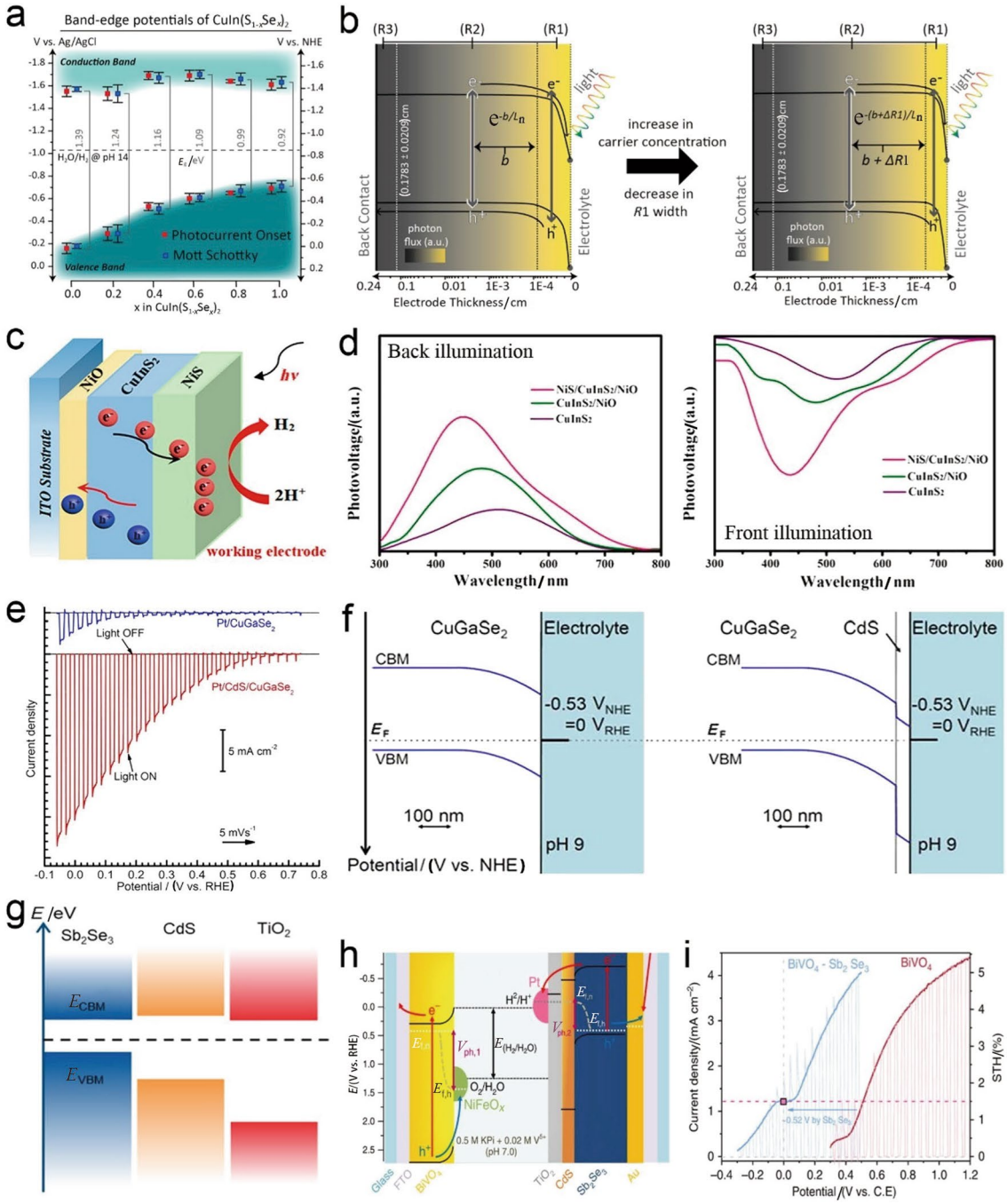

Fig. 9 Architecture, band diagram and performance of sulfide- and selenide-based photocathodes. **a** Schematic diagram of the electronic band positions of $CuIn(S_{1-x}Se_x)_2$. **b** Schematic of the three regions emerging in a semiconductor. Reprinted with permission from ACS. [186]. Copyright © 2018 American Chemical Society. **c** Schematic illustration of charge separation and transfer for the NiS/$CuInS_2$/NiO composite photocathode. **d** SPV spectra of photocathodes in (**c**). Reprinted with permission from Ref. [189]. Copyright © 2019 American Chemical Society. **e** $I-E$ curves for Pt/$CuGaSe_2$ and Pt/CdS/$CuGaSe_2$ photoelectrodes. **f** Calculated band alignment for $CuGaSe_2$ and CdS/$CuGaSe_2$ photoelectrodes. Reprinted with permission from ACS. [151]. Copyright © 2013 American Chemical Society. **g** Approximate energy diagram of Sb_2Se_3, CdS and TiO_2. Reprinted with permission from ACS. [217]. Copyright © 2019 American Chemical Society. **h** Scheme of the $NiFeO_x$/H,Mo:$BiVO_4$/FTO–Pt/TiO_2/CdS/Sb_2Se_3/Au/FTO tandem cell. **i** *JE* response for the photoanode and the photocathode. Reprinted with permission from Ref. [218]. Copyright © 2020 The Author(s)

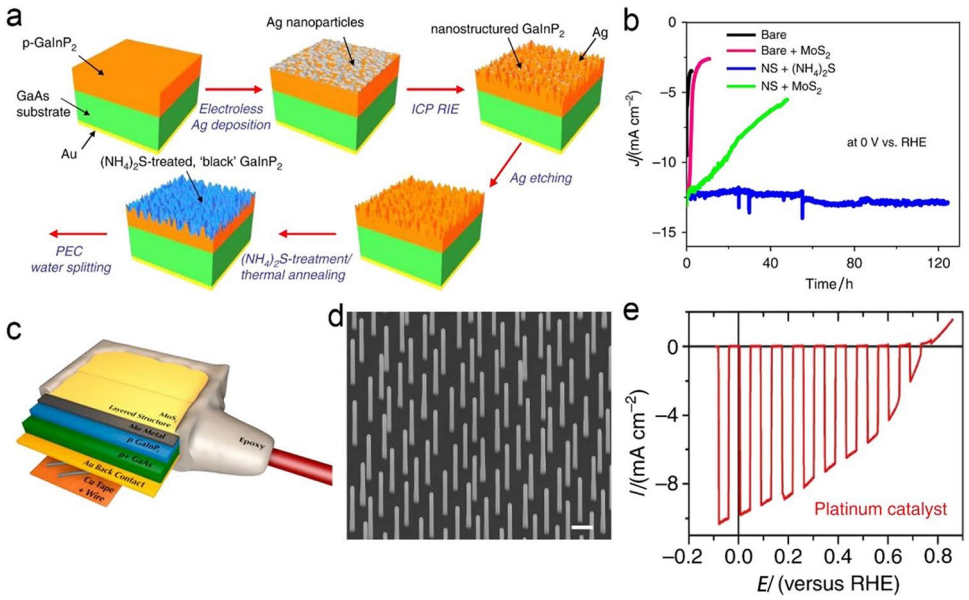

Fig. 10 Architecture and performance of nitride-, phosphide- and arsenide-based photocathodes. **a** Schematic illustration of the fabrication procedures for $GaInP_2$ photocathodes. **b** Long-term measurements under various material configurations. Reprinted with permission from Ref. [225]. Copyright © 2019 The Author(s). **c** Schematic of the synthesized p-$GaInP_2$/MoS_2 photocathode. Reprinted with permission from ACS. [226]. Copyright © 2016 American Chemical Society. **d** SEM image of a GaP NW array defined by nanoimprint lithography. The scale bar, 400 nm. **e** LSV curve of the GaP photocathode loaded with the platinum electrocatalyst. Reprinted with permission from Ref. [231]. Copyright © 2015 Macmillan Publishers Limited

density up to approximately 16 mA cm^{-2} at 0 V vs. RHE [216]. Moon et al. developed a facile spin-coating method to prepare self-oriented Sb_2Se_3 nanoneedle photocathodes [217]. Afterwards, they employed ultrafast terahertz (THz) spectroscopy, time-resolved photoluminescence (TRPL) and intensity-modulated photocurrent–photovoltage spectroscopy (IMPS/IMVS) to observe the photogenerated charge carrier dynamics in a photocathode with the $RuO_x/TiO_2/Sb_2Se_3$/Au/FTO configuration, revealing the dual functions of RuO_x in reducing surface recombination and accelerating charge transfer [211]. Then, they reported a photocathode with the Pt/TiO_2/CdS/Sb_2Se_3/Au/FTO configuration, achieving an outstanding photocurrent density of approximately 13.5 mA cm^{-2} at 0 V vs. RHE under simulated sunlight AM 1.5G irradiation in a pH 1 electrolyte (Fig. 9g) [217]. After optimization, they obtained a high-quality compact thin film with favourable crystallographic orientation by suppressing the growth kinetics via a close-space sublimation strategy, resulting in a benchmark photocurrent density of approximately 30 mA cm^{-2} at 0 V vs. RHE [218]. They constructed a tandem PEC device for bias-free solar water splitting with an optimized Pt/TiO_2/CdS/Sb_2Se_3/Au/FTO photocathode and a classic $BiVO_4$ photoanode, which exhibited an STH conversion efficiency of 1.5% with durability over 10 h (Fig. 9h) [218]. In addition, the voltage contribution of the photocathode to the bias-free PEC system was approximately 0.52 V (Fig. 9i). At present, the study of surface modification and heterostructures to enhance the performance of Sb_2Se_3 photocathodes has made remarkable progress [219, 220].

6.4 Nitrides, Phosphides and Arsenides

Gallium indium phosphide ($GaInP_2$) is a promising p-type semiconductor for application as a top light absorber of tandem PEC devices for solar water splitting [221–223]. The CB position is at − 0.6 V (vs. RHE). Benefiting from the high lattice matching, $GaInP_2$ with a band gap of approximately − 1.8 eV and gallium arsenide (GaAs) are suitable for constructing tandem photoelectrodes. A photocathode with the p–n–GaAs/p–$GaInP_2$ configuration has been demonstrated to exhibit a superior STH efficiency up to 12.4% [224]. However, the photocurrent density significantly decreased within 1 h due to the instability caused by photocorrosion. In view of this, Yoon et al. achieved an outstanding stability of over 120 h via a developed corrosion-resistant surface and a structure-tailored reactive interface (Fig. 9a and b) [225]. Specifically, $(NH_4)_2S$-treated nanostructured (NS) $GaInP_2$ photocathodes were fabricated by inductively coupled plasma reactive ion etching (ICP-RIE) and thermal annealing technologies (Fig. 10a), achieving ca. 91% FE and a photocurrent density of ca. −12.5 mA cm^{-2} (Fig. 10b). Moreover, Jaramillo and coworkers employed MoS_2 as an electrocatalyst and a surface protection layer to construct a

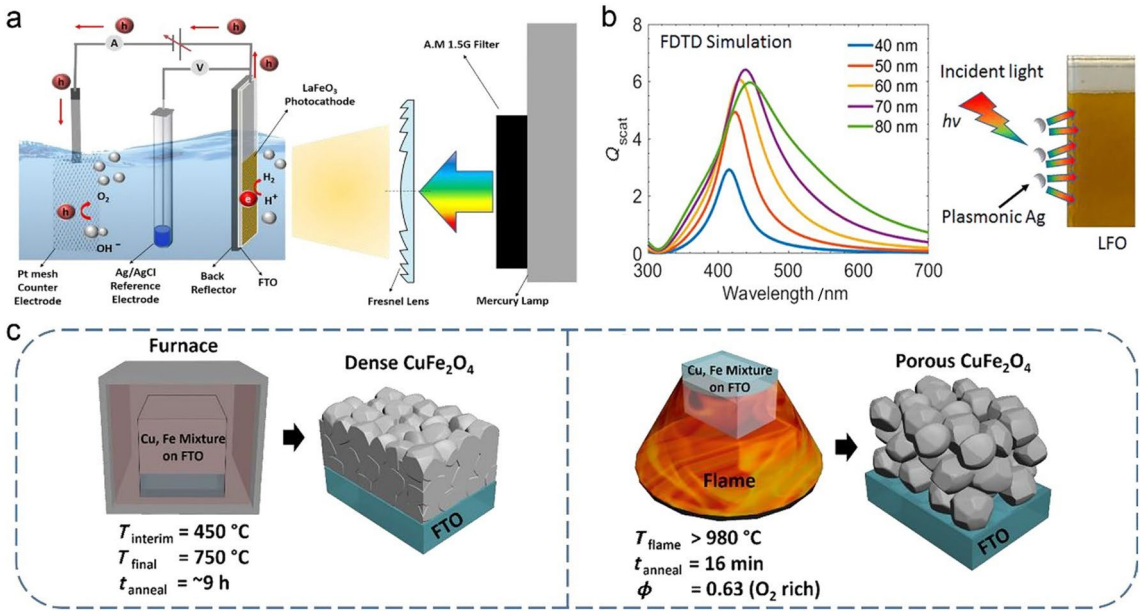

Fig. 11 Architecture and fabrication of Fe-based photocathodes. **a** Schematic of the experimental setup. A 350 W high-stability mercury (Hg) lamp with an AM 1.5G filter is used as the light source for the experiments, and a Fresnel lens is used to control the flux concentration of incident light. Reprinted with permission from Ref. [243]. Copyright © 2020 American Chemical Society. **b** Ag nanoparticles were modelled by using FDTD simulations, and the results show an optimal dimension of 50 − 80 nm for SPR enhancement. Reprinted with permission from Ref. [244]. Copyright © 2018 American Chemical Society. **c** Schematic of $CuFe_2O_4$ on FTO annealed by a furnace and a flame. Reprinted with permission from Ref. [254]. Copyright © 2019 American Chemical Society

photocathode with the MoS_2/Mo/$GaInP_2$/GaAs/Au configuration, resulting in a long-term stability of over 10 h without significant degradation (Fig. 10c) [226]. In addition, wurtzite p-type gallium phosphide (GaP) with a direct band gap of 2.1 eV exhibits reasonable stability in aqueous solution [227, 228]. The application of GaP to photocathodes has made considerable progress [229, 230]. Bakkers and coworkers reported a GaP NW photocathode for decoupling of light absorption (axial) and photogenerated carrier transfer (radial) (Fig. 10d), achieving a photocurrent density of approximately 9.5 mA cm^{-2} at 0 V vs. RHE (Fig. 10e) [231]. Furthermore, the p-type InP nanopillar photocathode with the Ru electrocatalyst reaches a photo-to-energy conversion efficiency of approximately 14% at a cell voltage of 0.5 V [232]. CoP and GaN are widely used in the electrocatalyst and protective layer of Si-based photocathodes [61, 96, 233, 234]. Jin et al. developed cost-effective ternary pyrite-type cobalt phosphosulphide (CoSP) as an electrocatalyst of a Si-based photocathode for solar water splitting, achieving a remarkable photocurrent density up to ca. 35 mA cm^{-2} at 0 V vs. RHE, rivalling the state-of-the-art precious Pt [235]. Furthermore, they highlighted that both the work function and light absorption of the overlayer in the integrated photocathode are crucial factors for achieving superior solar-driven water splitting [235].

6.5 Fe-Based Compounds

The p-type MFe_xO_y (M = La, Bi, Cu, Mn, Zn, Ca) series are promising photocathode candidates because of their superior photoelectric conversion properties and outstanding stability in aqueous electrolytes [236, 237, 238, 239]. The band gap of $LaFeO_3$ is approximately 2.1–2.6 eV, and the CB position is at − 0.6 V (vs. RHE), which allows absorption and utilization of most of the visible wavelengths of sunlight [236, 240, 241, 242]. However, the lower photocurrent density limits its large-scale application as a photocathode in PEC systems. In view of this, Tahir et al. recently demonstrated a strategy of concentrating the photon flux via a Fresnel lens and a back reflector to enhance the photocurrent density of the $LaFeO_3$ photocathode, revealing that the photocurrent density depends approximately linearly on the photon flux and is enhanced nine times under a flux of 18 sun (1 sun = 1 367 W m^{-2}) (Fig. 11a) [243]. Moreover, they employed Ag particles with the optimal dimension of 50–80 nm, screened by finite difference time domain (FDTD) simulations, to construct a photocathode, in which surface plasmon resonances (SPRs) enhanced $LaFeO_3$ light harvesting to promote PEC hydrogen evolution (Fig. 11b) [244]. In addition, the $LaFeO_3$ photocathode optimized by lithium doping and an Au buffer layer also showed promise for applications [240, 245, 246]. Recently, Yang and coworkers constructed a type-II heterojunction film photocathode with the Bi_2O_3/$BiFeO_3$

configuration on an indium tin oxide (ITO) substrate, resulting in a superior PEC response under AM 1.5G sunlight irradiation [247]. In addition to the TiO_2 protective layer and Au buffer layer used by Shen et al. [248, 249], use of the plasma effect of Au has also been attempted by Cheng et al. to enhance the performance of $BiFeO_3$-based photocathodes [250].

$CuFe_2O_4$ with a band gap of 1.54–1.95 eV exhibits a theoretical maximum photocurrent density of approximately 27 mA cm^{-2} and an STH conversion efficiency of approximately 33% [251–253]. Zheng and coworkers developed a superior rapid high-temperature flame annealing method (> 980 °C), which only takes 16 min to prepare crystalline and porous $CuFe_2O_4$ photocathodes (Fig. 11a) [254]. Compared with furnace-annealed dense $CuFe_2O_4$, the photocurrent density of the flame-annealed $CuFe_2O_4$ photocathode is increased by approximately 2.9 times, reaching 3.5 mA cm^{-2} at 0.4 V vs. RHE. In addition, the hybrid microwave annealing strategy, heterojunctions and three-dimensional ordered periodic macroporous structures have also been applied to improve the performance of $CuFe_2O_4$-based photocathodes [255–258]. $MnFe_2O_4$ and $ZnFe_2O_3$ are widely used in integrated composite photocathodes with superior solar water splitting performance [259, 260]. $CaFeO_3$ with a narrow band gap of 1.9 eV and a band edge across the redox potential of H_2O was first applied to photocathodes by Ida and coworkers in 2010 [261]. Afterwards, their optimized RuO_x/TiO_2/$CaFeO_3$ photocathode with TiO_2 as a protective layer and RuO_x as an electrocatalyst achieved a beneficial shift in the onset potential, delivering bias-free hydrogen evolution under 470 nm excitation [262].

6.6 Organic Polymers and Small Molecule Semiconductors

The light absorption and excitation mechanisms of organic small molecules and polymers, which are different from those of conventional inorganic absorbers, make them exhibit promise for application in the field of organic optoelectronics, such as in organic light-emitting diodes (OLEDs), organic solar cells, organic field-effect transistors (OFETs) and organic photocathodes [263–268]. Organic molecules or monomers exhibit the property of being an electron donor (D) or an acceptor (A) due to the difference in group electronegativity and energy levels [269]. Similar to band theory, the highest occupied molecular orbital (HOMO) in frontier (molecular) orbital theory of the excited state is widely accepted to be the electron-donating region, while the lowest unoccupied molecular orbital (LUMO) is the electron-accepting region [270, 271]. For polymers, precise control of the degree of polymerization (DP) is an effective way to directly tune the HOMO–LUMO gap and change the optical properties because generally, the HOMO–LUMO gap decreases with increase in DP [270, 271]. Eventually, if the material is polymerized into an ordered polymer such as a covalent organic framework (COF), then the periodicity will split the discrete energy levels into continuous energy bands, as in inorganic crystals [269]. Similarly, the degree of orderly self-assembly from small molecules to supramolecules will also affect the band gap [272].

Recently, Feng et al. demonstrated a practical strategy to modulate the band edge and optical gap by tailoring aromatic units of conjugated acetylenic polymers from benzene- to thiophene-based, resulting in the poly(2,5-diethynylthieno[3,2-b] thiophene) (pDET) photocathode exhibiting a benchmark HER performance with a photocurrent of 370 μA cm^{-2} and an IPCE of 12.6% under simulated sunlight illumination (Fig. 12a) [263]. Specifically, the evaluated HOMO and LUMO levels from the monomer to decamer of DET gradually approached the VB and CB edges of pDET, respectively (Fig. 12a) [263]. In addition, on the basis of conventional heterojunctions, including type-I, type-II and type-III heterojunctions, they developed a strategy for preparing a gradient homojunction by controlling the copolymerization of 1,4-diethynylbenzene (DEB) and 1,3,5-triethynylbenzene (TEB) (Fig. 12b) [273]. The highlight is that the gradient distribution of the TEB monomer in poly(DEB) leads to continuous band bending, producing a gradient homojunction. The organic gradient homojunction has far-reaching significance for the development of ideal solar spectrum absorbers with artificially tuned band structures Afterwards, they constructed a Z-scheme organic–inorganic hybrid photocathode by grafting pDET to cuprous oxide, achieving a carrier separation efficiency of approximately 16% and a photocurrent density of 370 μA cm^{-2} at 0.3 V vs. RHE under AM 1.5G irradiation in a 0.1 M Na_2SO_4 aqueous solution.

In addition to applications in the fields of catalysis, separation and storage, benefiting from the versatile optical and electronic properties based on the flexible building blocks and three-dimensional stacking, a COF was first applied to a PEC device as a photocathode in 2018 (Fig. 12c) [274]. If the influence of protonation and deprotonation on the COF levels is neglected [274], then the LUMO level is higher than the theoretical potential of the HER over the entire pH range of the electrolyte, indicating that photoexcited electrons can spontaneously participate in the three typical HER steps (Fig. 12d). Generally, PEDOT:PSS [275] is used as the HTL and fullerene (C_{60}, n-type) [276] is used as the electron collection layer in organic photoelectrodes. Artero et al. reported two innovative three-layer planar heterojunction (3-PHJ) and hybrid heterojunction (HHJ) photocathodes by employing the small molecules alpha-sexithiophene (α-6 T) as a donor and boron subphthalocyanine chloride (SubPc) and boron subnaphthalocyanine chloride (SubNc) as acceptors (Fig. 12e and f) [277].

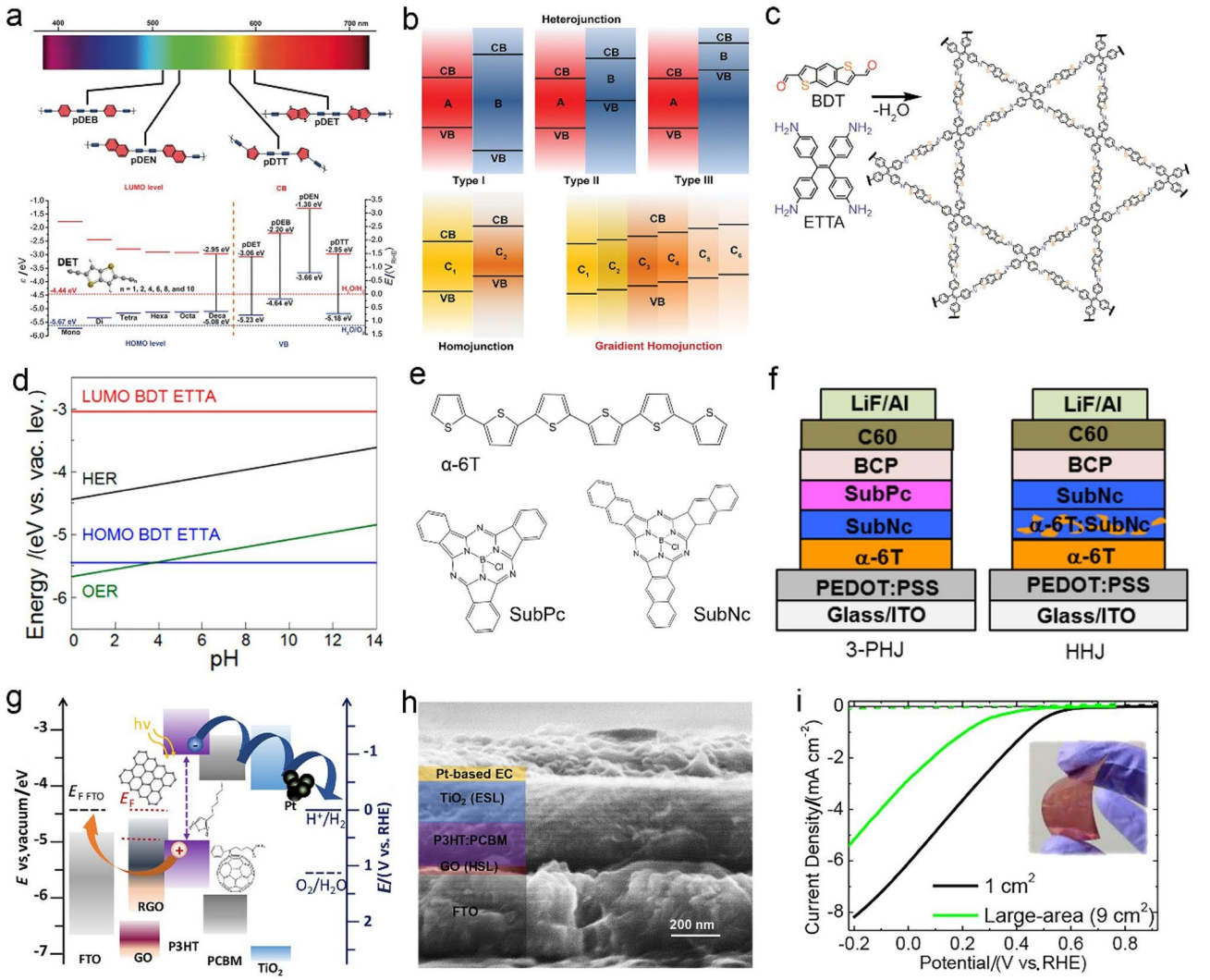

Fig. 12 Architecture, band diagram and performance of organic-based photocathodes. **a** Schematic illustrations of the absorption edges and energy diagram of pDEB, pDEN, pDTT and pDET. Reprinted with permission from Ref. [263]. Copyright © 2019 Wiley–VCH Verlag GmbH & Co. KGaA, Weinheim. **b** Band alignment in type-I/II/III heterojunctions, a homojunction and a gradient homojunction. Reprinted with permission from Ref. [273]. Copyright © 2019 WILEY–VCH Verlag GmbH & Co. KGaA, Weinheim. **c** Synthetic approach for the formation of a BDT-ETTA COF with a hexagonal AA eclipsed framework. **d** Calculated alignment between the HOMO and the LUMO of BDT-ETTA and the water splitting redox couples. Reprinted with permission from Ref. [274]. Copyright © 2017 American Chemical Society. **e** Molecular structures of α-6 T, SubPc and SubNc. **f** Schematic representation of the device architectures. Reprinted with permission from Ref. [277]. Copyright © 2016 IOP Publishing Ltd. **g** Scheme of the band edge positions of the materials assembled in the solution-processed organic photocathode. **h** High-resolution cross-sectional SEM image of the representative photocathode FTO/GO/rr-P3HT:PCBM/TiO_2/Pt-based electrocatalyst. **i** LSV curves of ITO-PET/GO/rr-P3HT:PCBM/TiO_2/Pt/C-Nafion photocathodes with different areas. Reprinted with permission from Ref. [288]. Copyright © 2017 American Chemical Society

Specifically, 2,9-dimethyl-4,7-diphenyl-1,10-phenantroline (BCP) was used as an exciton-blocking layer, and LiF/Al or amorphous molybdenum sulphide (a-MoS_x) was used as the electrocatalyst layer for the HER. In addition to the effective polymer bulk heterojunction (BHJ) photocathode with a donor–acceptor (D–A) configuration reported by Li and coworkers [278], Feng et al. demonstrated a thiophene-bridged D–A photocathode [279]. Moreover, thiophene derivatives and polymers are widely used in the surface protective layer of organic photocathodes due to the rather robust photocorrosion resistance feature [280–282].

Bonaccorso and Jousselme's groups reported another classic poly(3-hexylthiophene):phenyl-C_{61}-butyric-acid methyl ester (PCBM:P3HT) BHJ-based photocathode [283–287]. The photocathode with the Pt/TiO_2/P3HT:PCBM/GO/FTO configuration exhibits superior performance among all PCBM:P3HT-based systems (Fig. 12g and h), achieving an outstanding photocurrent density of

approximately 8.2 mA cm^{-2} at − 0.2 V vs. RHE (Fig. 12i) [288]. Furthermore, the multilayer composite photocathode constructed by the overlayer C_3N_4 and light absorbers such as Si NWs, CuO and $CoSe_2$ also shows promising application potential [289–291].

6.7 Dye Sensitization and Surface Grafted Molecular Catalysts

Compared with superior p-type light absorbers, such as Si, Cu_2O, CZTS and CIGS, whose performance is easily affected by the crystal structure degradation caused by photocorrosion, wide band gap semiconductors are more stable in aqueous electrolytes. Benefiting from the development of high-efficiency, tuneable electron transfer processes and cost-effective organic dyes for dye-sensitized solar cells (DSSCs) [292], similar dye-sensitized photoelectrodes (DSPEs) [293], which can compensate for the light-harvesting limitation of wide band gap semiconductors, are an attractive strategy for solar water splitting. Moreover, molecular electrocatalysts show great potential for development of photoelectrodes with high utilization of precious metals and low cost due to their fine-tuning in redox properties and structures and high catalytic efficiencies [294, 295, 296]. Sun et al. demonstrated a typical tandem dye-sensitized PEC system with mesoporous TiO_2 as a photoanode and nanostructured NiO as a photocathode, achieving bias-free solar water splitting under a neutral pH 7 electrolyte by visible light with an IPCE of 25% at 380 nm (Fig. 13a) [297]. More specifically, the two organic dyes L0 and P1 were used as photosensitizers, while the two molecular complexes Ru1 and Co1 were used as electrocatalysts for the OER and HER, respectively (Fig. 13a). The authors stated that L0 + Ru1@TiO_2 can convert more photons to electrons than P1 + Co1@NiO and exhibits a higher photocurrent [297], indicating that the photocathode is the bottleneck of this tandem system. In addition, Artero and coworkers recently constructed a push–pull $CuGaO_2$|RBG-174|CoHEC photocathode by employing the bithiophene-bridged organic dye RGB-174 as a photosensitizer and CoHEC as an electrocatalyst (Fig. 13b), achieving an FE of approximately 87% for hydrogen production after coupling with a TaON|CoO_x photoanode without any applied bias [298]. They also attempted the application of a photosensitizer with a similar structure on NiO [299].

Different from the above separation of catalysts and photosensitizers, Wu et al. demonstrated a photostable photocathode by grafting a bifunctional cyclometalated ruthenium photosensitizer (O22) and a cobaloxime catalyst ($CodmgBF_2$) onto NiO (Fig. 13c) [300]. After the photosensitizer is excited by photons with energy greater than the HOMO–LUMO gap of approximately 1.96 eV, electrons are transferred to $CodmBF_2$ for the HER, and holes are reversely transferred to NiO. The authors highlighted that the strong binding of O22 and the metal oxide endows the photocathode with outstanding stability and promising application potential. Moreover, Moutet et al. prepared a composite photocathode with MoS_x as an electrocatalyst and a poly[tris(bipyridyl)ruthenium(II)] film as a photosensitizer by electropolymerization for the first time [301]. Coutsolelos and coworkers reported a noble metal-free covalent porphyrin-cobalt diimine-dioxime dyad (ZnP-Co) for sensitizing NiO film photocathodes (Fig. 13d) [302]. Similar to the thiophene described in the previous section, triazole bridges have also been widely used to enhance electron transfer [303, 304]. A photophysical investigation performed by the authors revealed sufficient electronic communication between the thiophene-bridged photosensitizer and catalyst in the excited state (Fig. 13d) [302]. Increasing the activity of the catalyst grafted on the photocathode is generally believed to be a beneficial way to enhance the performance of a PEC system [60, 305, 306]. However, Rose et al. have different opinions on this and recently proposed that the dominant HER-beneficial effect is the thermodynamic p-type band bending induced by ligand attachment and metal binding, rather than the kinetic catalytic benefit [307]. Specifically, they designed a Si|BisPNP macrochelate surface for binding of Ni(II) and used it to evaluate the beneficial thermodynamic effects (band bending) versus kinetic effects (catalysis) for the HER (Fig. 13e) [307]. They employed equivalent circuit parameters from electrochemical impedance spectroscopy (EIS) and the onset potential of the HER to quantify the flat band potential of the photocathode, revealing that the band bending induced by metal ion binding is a dominant factor for HER benefits, while the catalytic effects of PNP-Ni(II) are minimal [307]. Therefore, the design concept of the semiconductor and molecular hybrid photocathode is to maximize the p-type band bending to increase the driving force for the separation of excitons and photogenerated carriers, thereby enhancing the HER performance.

6.8 Perovskites and Quantum Dots

Organic–inorganic hybrid halide perovskites exhibit superior optoelectronic performance, rivalling all the current light absorbers, and they are widely applied in solar cells due to their tuneable direct band gap, long carrier lifetime and appropriate exciton binding energy [308, 309, 310]. However, some macroencapsulation and passivation strategies are commonly used to enhance the stability and performance of light absorbers since halide perovskites are sensitive to oxygen and humidity in the environment [311–314]. Similarly, Martinson et al. reported a stable triple-cation halide perovskite $Cs_{0.05}(MA_{0.7}FA_{0.83})_{0.95}Pb(I_{0.83}Br_{0.17})_3$ photocathode with an HTL of PEDOT:PSS and an electron

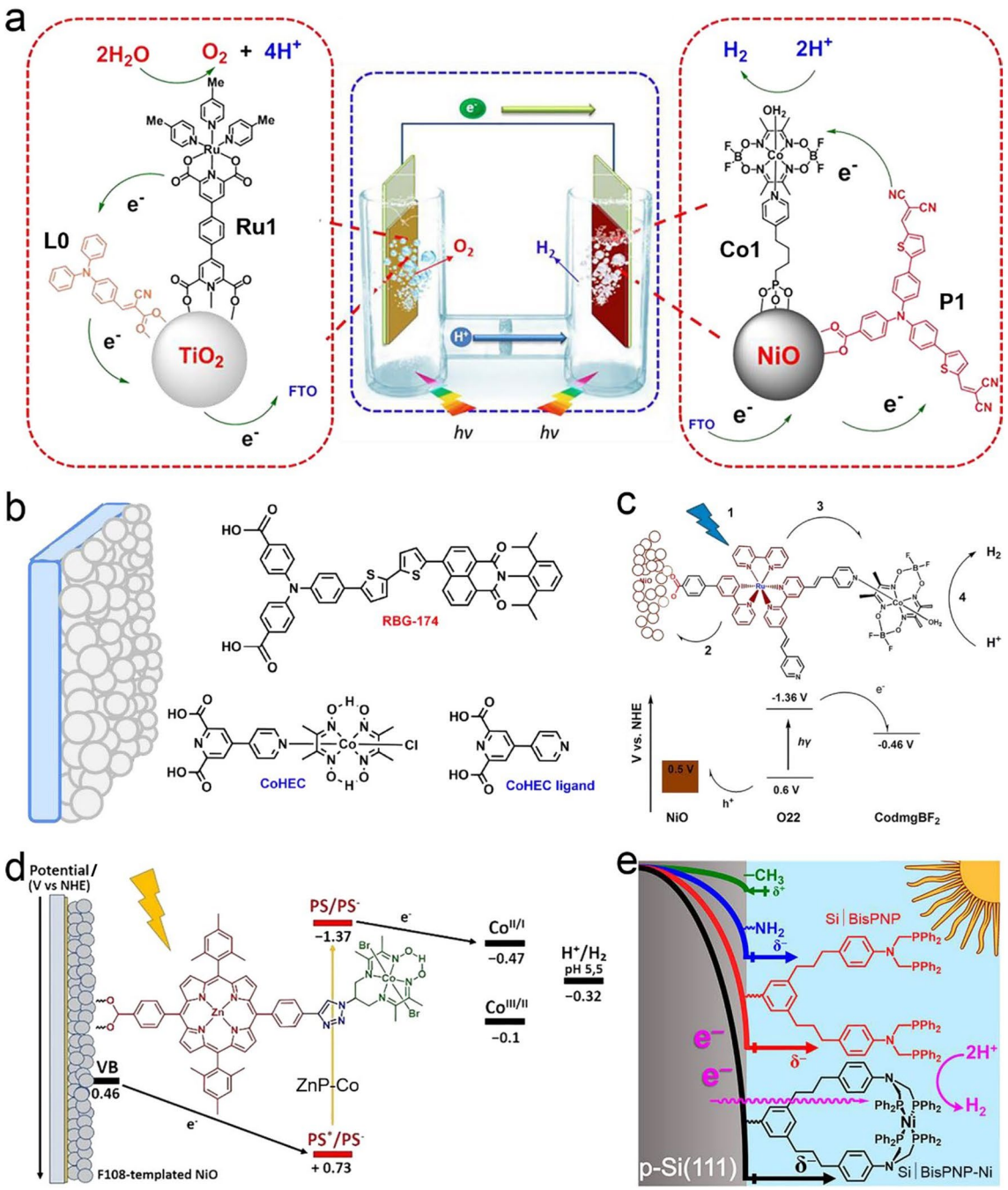

Fig. 13 Architecture and energy diagram of sensitizing dyes and grafted molecular catalysts. **a** Schematic diagram of the tandem dye-sensitized PEC (DS-PEC) cell. Reprinted with permission from Ref. [297]. Copyright © 2015 American Chemical Society. **b** Molecular structures of the $CuGaO_2$|RBG-174|CoHEC photocathode. Reprinted with permission from Ref. [298]. Copyright © 2019 American Chemical Society. **c** Schematic and energy diagram of the NiO DS–PEC electrode. Reprinted with permission from Ref. [300]. Copyright © 2013 American Chemical Society. **d** Energy diagram at pH 5.5 and the working principle of the NiO photocathode based on ZnP-Co. Reprinted with permission from Ref. [302]. Copyright © 2021 Wiley–VCH GmbH. **e** The band bending of the substrate depends on the molecular structure of the sensitizing dye. Reprinted with permission from Ref. [307]. Copyright © 2020 American Chemical Society

transport layer (ETL) of PCBM + ALD-TiO_2 (Fig. 14a), achieving a remarkable photocurrent density of at least 10 mA cm^{-2} at 0 V vs. RHE under 0.5 sun illumination in 0.5 M H_2SO_4 (Fig. 14b) [315]. However, the stability dropped by more than 20% within 2 h, which is far from practical applications. Li and coworkers proposed a similar strategy to enhance the stability and performance of a sandwich-like organolead halide $CH_3NH_3PbI_3$ perovskite

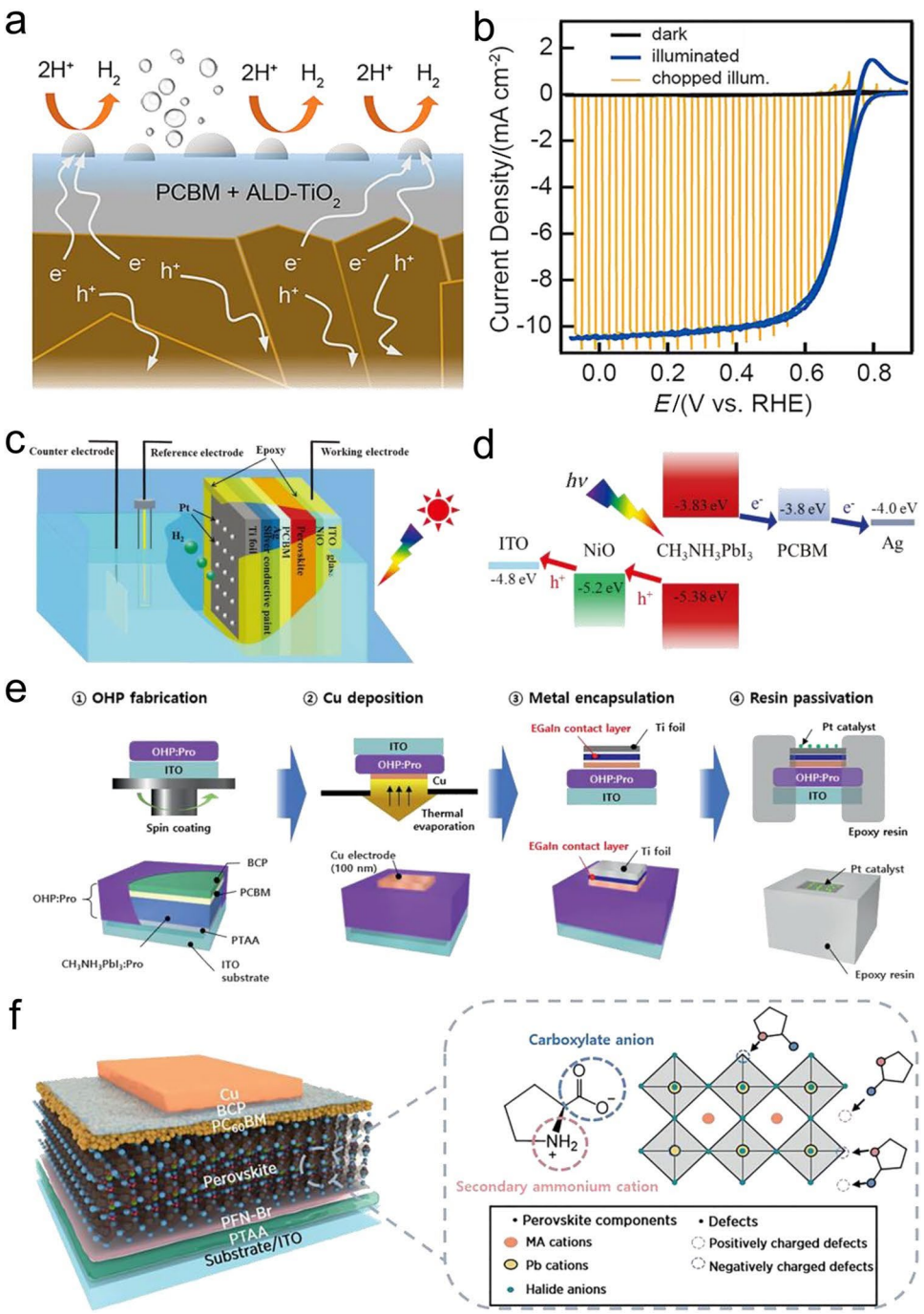

Fig. 14 Schematic diagram, performance and preparation processes of perovskite-based photocathodes. **a** Cross-sectional schematic of a photocathode stabilized against corrosion via a hybrid ETL comprising PC61BM with TiO_2 deposited by ALD. **b** PEC behaviour of the photocathode in the dark and under continuous and chopped illumination. Reprinted with permission from Ref. [315]. Copyright © 2019 American Chemical Society. **c** Schematic illustration of the sandwich-like $CH_3NH_3PbI_3$-based photocathode. **d** Schematic energy diagram of each component in the inverted $CH_3NH_3PbI_3$ solar cell. Reprinted with permission from Ref. [316]. Copyright © 2018 WILEY-VCH Verlag GmbH & Co. KGaA, Weinheim. **e** Fabrication sequence of the EGaIn–OHP photocathode. **f** Schematic of the OHP solar cell device architecture and the possible passivation mechanism of the L-Proline molecule at perovskite defects. Reprinted with permission from Ref. [317]. Copyright © 2021 Wiley–VCH GmbH

photocathode (Fig. 14c), reaching an ameliorated stability with a degradation of approximately 10% within 12 h over a wide range [316]. Benefiting from the reasonable band alignment of the photocathode (Fig. 14d), the perovskite-based photocathode delivers a superior photocurrent density of 18 mA cm^{-2} at 0 V vs. RHE under AM 1.5G illumination in 0.5 M H_2SO_4 [316]. Recently, Lee reported a high-efficiency photocathode based on the organometal halide perovskite (OHP) methylammonium lead triiodide ($MAPbI_3$), which employed L-proline (Pro) with a zwitterion molecular structure to effectively passivate both positively and negatively charged defects in the light absorber $MAPbI_3$ (Fig. 14e and f) [317]. The configuration of the solar cell is Cu/BCP/$PC_{60}BM$(PCBM)/$MaPbI_3$(OHP:Pro)/PFN-Br/PTAA/ITO, where PTAA and PFN-Br represent poly[bis(4-phenyl)(2,4,6-tri-methylphenyl)amine] as an HTL and poly(9,9-bis(3′-(*N*,*N*-dimethyl)-*N*-ethylammonium-propyl-2,7-fluorene)-alt-2,7-(9,9-dioctylfluorene)) dibromide as an interfacial layer, respectively (Fig. 14f) [317]. Eutectic gallium indium alloy (EGaIn) and Ti foil were employed

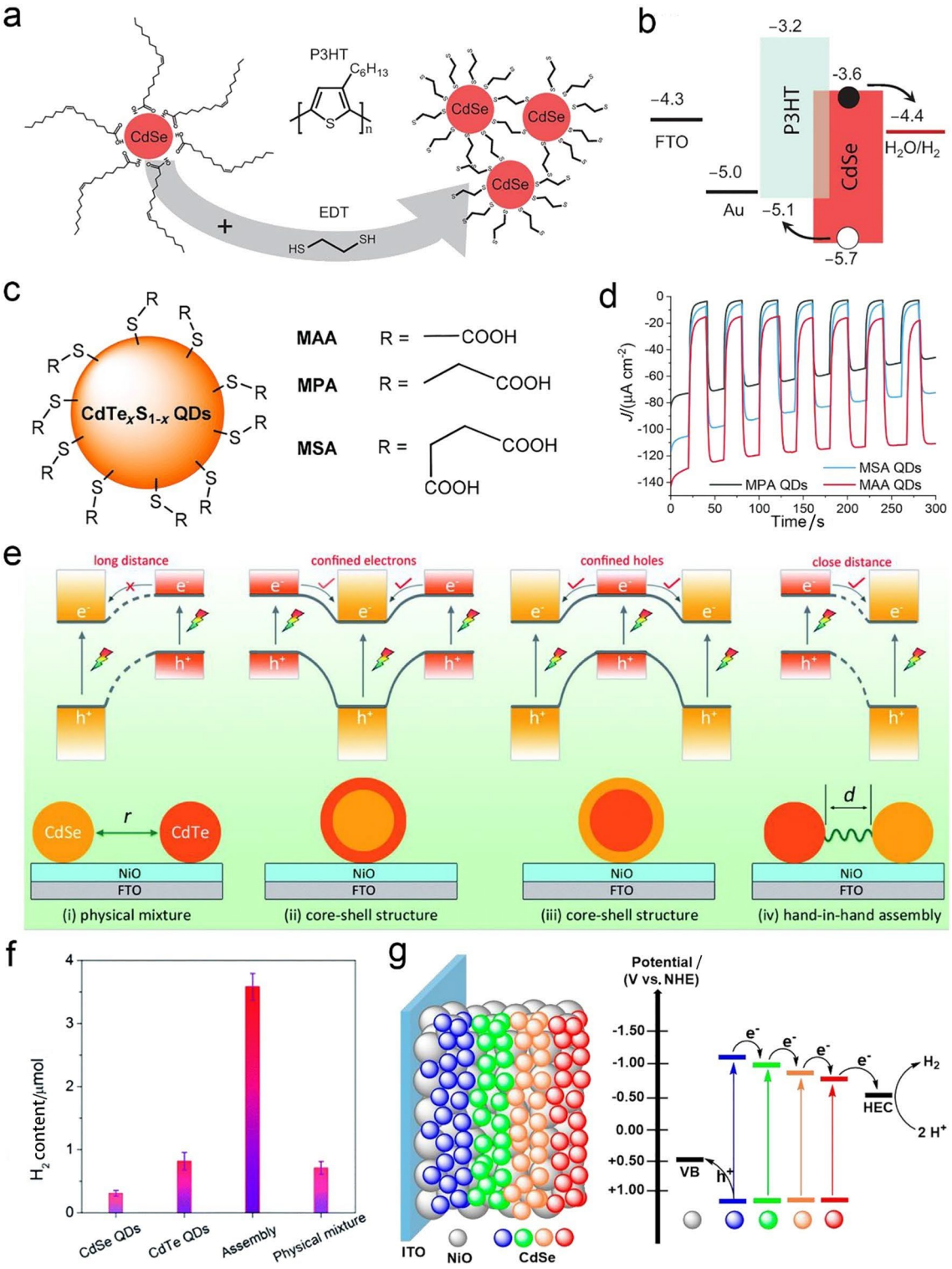

to encapsulate the OHP:Pro-based photocathode (Fig. 14e), while Pt was used as an electrocatalyst, achieving a remarkable photocurrent density of approximately 21 mA cm^{-2} and a long-term durability of over 54 h under AM 1.5G illumination in a sulphuric acid electrolyte [317]. In addition, perovskite-based solar cells are commonly applied to drive PEC and electrochemical (EC) devices for solar water splitting [168, 318, 319].

Quantum dots (QDs) exhibit superior optoelectronic properties, which benefit from the quantum confinement effect [320, 321]. As efficient luminescent materials, QDs have achieved many in-depth research results [322–324] and

◂**Fig. 15** Structural features, performance and band diagrams of QD-based photocathodes. **a** Chemical structure of P3HT and EDT; schematics of CdSe QDs with oleic acid ligands and after cross-linking using EDT. **b** Energy diagram of the hybrid photocathode. Reprinted with permission from Ref. [339]. Copyright © 2015 American Chemical Society. **c** Structural representation of $CdTe_xS_{1-x}$ QDs. **d** Chronoamperometry test of a $CdTe_xS_{1-x}$ QD-based photocathode at 0 V vs. NHE under chopped irradiation. Reprinted with permission from Ref. [345]. Copyright © 2021 The Royal Society of Chemistry. **e** Schematic illustration of QD-sensitized electrodes with different structures (below) and the corresponding charge transfer processes on the electrode surface (above). **f** Photocatalytic H_2 evolution in aqueous solution. Reprinted with permission from Ref. [349]. Copyright © 2019 The Royal Society of Chemistry. **g** Schematic illustration of a different-sized CdSe QD-sensitized NiO/ITO rainbow photocathode as well as the energy diagrams of different-sized CdSe QDs and the electron transfer process between them. Reprinted with permission from Ref. [332]. Copyright © 2017 National Academy of Sciences, USA

extensive applications [325–328]. Moreover, in recent years, the application of QDs as light absorbers or sensitizers in PEC systems has also shown an upward trend due to their tuneable light absorption, large extinction coefficients over a broad spectral region and rich surface binding features [275, 329–332]. Carbon and graphene QDs are commonly used to enhance the broadband solar absorption [333, 334] of photocathodes and as the support for electrocatalysts [334, 335], and CdS QDs were employed by Yang et al. as a sensitizer for NiO photocathodes [194]. The photocathode based on CdSe QDs with a flexible and tuneable band gap is the research frontier among all the current QD materials applied in PEC systems [336–338]. Loi et al. reported an effective photocathode with a type-II heterojunction based on an organic–inorganic hybrid composed of CdSe QDs and P3HT (Fig. 15a and b) [339], where 1,2-ethanedithiol (EDT) was employed to replace long and insulating oleic acid molecules to encapsulate and functionalize CdSe QDs (Fig. 15a) [339]. The small molecule EDT shortens the distance between P3HT and the CdSe QD absorber [340–342], which is beneficial to charge transfer [343, 344], resulting in a photocurrent density of 1.24 mA cm^{-2} at 0 V vs. RHE and an external quantum efficiency (EQE) of 15% under AM 1.5G illumination [339]. In addition, Natali and coworkers recently demonstrated a series of NiO photocathodes with $CdTe_xS_{1-x}$ QDs featuring different capping agents, including mercaptopropionic acid (MPA), mercaptoacetic acid (MAA) and mercaptosuccinic acid (MSA), as sensitizers (Fig. 15c) [345]. The MAA-capped QDs exhibit a superior photocurrent density of 100 μA cm^{-2} compared to the others in the presence of $[Co^{III}(NH_3)_5Cl]Cl_2$ as an irreversible electron acceptor under chopped AM 1.5G irradiation (Fig. 15d) [345]. The above and similar works [346–348] again proved that short-chain surface-encapsulated molecules are conducive to charge transfer and thus enhanced photocurrent.

In view of the favourably oriented charge migration in the QD-based photocathode, Wu and coworkers constructed a hand-in-hand assembly of CdSe and CdTe QDs for solar water splitting (Fig. 15e), where the linker molecule between CdSe and CdTe can facilitate electronic coupling by shortening the distance between the two components [349]. Different from the physically mixed structure, which makes effective separation of photogenerated carriers difficult, and the conventional core–shell structure, which confines charge carriers, this assembled type-II hand-in-hand QD system with oriented charge migration exhibits much higher photocurrent density of up to 140 μA cm^{-2} and hydrogen production rates (Fig. 15f) [349]. In addition, Eisenberg et al. constructed a rainbow photocathode with good light-harvesting ability by spin-coating different-sized CdSe QD sensitizers on a NiO substrate (Fig. 15g) [332]. The forward energetic gradient is beneficial to photogenerated carrier separation and subsequent electron transfer, producing a photocurrent density as high as 115 μA cm^{-2} and an FE of 99.5% under white LED light illumination of 350 mW [349]. However, in the development of QDs applied to PEC devices in the future, the configuration of photoelectrodes must be optimized, efficient and water-stable QD materials must be expanded, and the dependence on hole sacrificial agents must be gradually eliminated.

6.9 Metal–Insulator–Semiconductor (MIS) Photoelectrode Architecture and Its Application

Similar to p–n junctions, TJs are also widely used in PV devices [350–352] and electronic industries [353, 354], where the physical principle is the quantum tunnelling effect [355–357]. The wave function is the mathematical expression of the quantum state of particles such as electrons and photons. We can predict the probability of particles appearing in any space at any time by employing the amplitude of the wave function in time and space. This probability can have nonzero values at multiple spatial locations at the same time. Therefore, although the probability of quantum tunnelling that depends on the height or thickness of the barrier will decay exponentially, the probability of reaching the other side of the barrier will not decay to zero under certain restrictions or conditions. Consequently, particles have a probability of tunnelling through the barrier in theory. Recently, MIS architectures based on the quantum tunnelling effect have been commonly applied to decouple the trade-off between the light-harvesting efficiency and stability of photoelectrodes in a PEC system [358, 359]. Specifically, the aforementioned absorbers with superior light absorption ability are susceptible to corrosion by electrolytes and photogenerated carriers, and protective coatings are commonly used to enhance the stability and performance in aqueous solutions. Early attempts were made to deposit

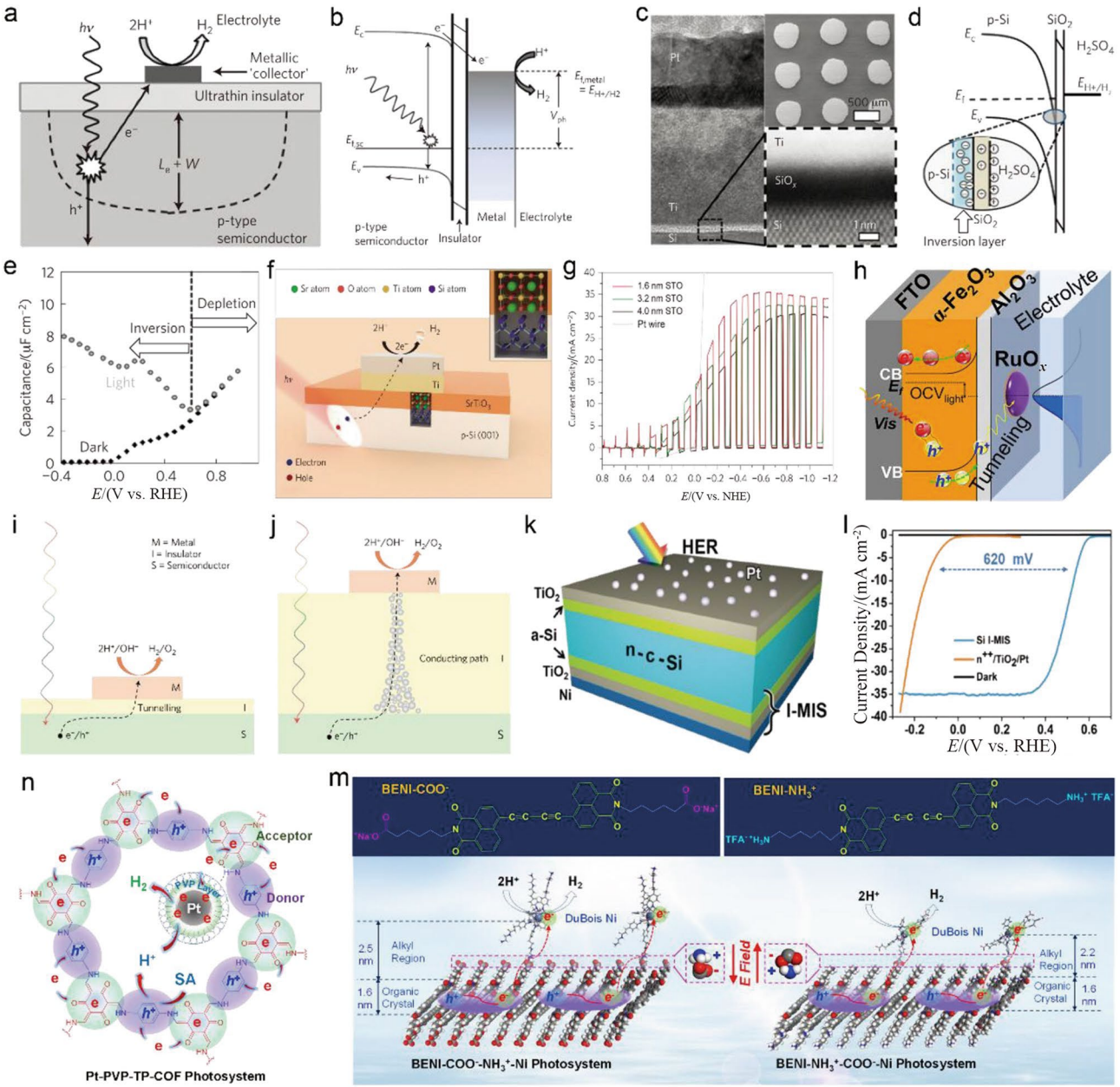

electrocatalysts such as Pt and other metals directly on the surface of light absorbers [360]. However, the Fermi-level pinning induced by the direct metal/semiconductor contact will reduce band bending and then decrease the photovoltage, but inserting a thin metal oxide can reduce or eliminate the Fermi-level pinning [361]. Thus, MIS architectures have been widely used for solar water splitting.

A typical MIS photocathode reported by Talin and coworkers is shown in Fig. 16a, where the electrocatalyst for the HER acts as the metallic collector of electrons [362]. The minority carriers of narrow band gap semiconductors, which are well suited for absorbing sunlight, tunnel through the insulating layer to the collector [362]. The requirement for insulators, which are generally oxides, is not only to protect the light absorbers from the corrosion by electrolytes but also to effectively mediate minority carrier tunnelling through the MIS junction with minimal recombination. Only the photogenerated electrons created within the sum of the depletion width (W) and the effective diffusion length (L_e) of minority carriers are generally accepted to be able to contribute to the photocurrent (Fig. 16a) [362]. Based on the band diagram of the p-type MIS photocathode (Fig. 16b), the photogenerated minority electrons can directly tunnel from the semiconductor CB edge (E_c) to the Fermi level of the metallic collector ($E_{F,metal}$) for the HER [362]. According to this mechanism, Talin et al. constructed an MIS-type

◂**Fig. 16** Mechanism and application expansion of photoelectrodes based on the MIS architecture. **a** Schematic side view of an MIS photoelectrode with a metallic collector situated on an insulator-covered p-type semiconductor. **b** Band diagram for a standard MIS junction with a p-type semiconductor. **c** Cross-sectional high-resolution transmission electron microscopy (HR-TEM) image (left) of a 20/30 nm Pt/Ti bilayer collector deposited on SiO_2|p-Si(100), HAADF-TEM image (lower right) of the tunnelling oxide, and the top-view SEM image (upper right) of 500 µm diameter PtTi collectors. **d** Energy band diagram and schematic of a p-Si/SiO_2/electrolyte junction in a state of inversion. **e** Capacitance–voltage curves recorded for a 2 nm SiO_2/p-Si(100) electrode in the dark with a 50 Hz a.c. frequency and under simulated AM1.5G illumination. Reprinted with permission from Ref. [362]. Copyright © 2013 Macmillan Publishers Limited. **f** Schematic structure of the $SiTO_3$ (STO)-protected Si photocathode showing that light is absorbed by the p-Si substrate and the photogenerated electrons tunnel to the surface metallic dots, at which H_2 is produced. **g** LSV measurement with chopped illumination of Pt/Ti/STO/p-Si(001) for various STO thicknesses. Reprinted with permission from Ref. [363]. Copyright © 2014 Macmillan Publishers Limited. **h** Schematic of the MIS Fe_2O_3-based photoelectrode with a tunnelling layer of 3 nm Al_2O_3. Reprinted with permission from Ref. [364]. Copyright © 2021 Wiley–VCH GmbH. Schematics of the MIS photoelectrode for water reduction/oxidation with **i** an ultrathin tunnelling layer and **j** a thick insulating layer with a localized conducting path. Reprinted with permission from Ref. [365]. Copyright ©2016 Macmillan Publishers limited, part of Springer Nature. **k** Schematic of the Si I-MIS photocathode. **l** *J*–*E* curves of the Si I-MIS-based photocathode under simulated AM 1.5G illumination. Reprinted with permission from Ref. [59]. Copyright © 2020 The Royal Society of Chemistry. **m** Schematic illustration of the MIS Pt-PVP-COF photosystem for hydrogen production. Reprinted with permission from Ref. [272]. Copyright © 2020 Wiley–VCH GmbH. **n** Molecular structure of BENI-COO^- and BENI-NH_3^+, and illustration of the supramolecular MIS photosystems for biomimetic hydrogen production. Reprinted with permission from Ref. [269]. Copyright © 2019 Wiley–VCH Verlag GmbH & Co. KGaA, Weinheim

photocathode with a Pt/Ti bilayer collector with a thickness of 20/30 nm deposited on a SiO_2(2 nm)|Si(110) substrate, where Pt/Ti collectors with a diameter of 500 µm were arranged in a square lattice with an 850 µm pitch (Fig. 16c) [362]. The authors proposed a negatively charged minority carrier inversion layer next to the p-type Si/SiO_2 interface to explain the observation of a photocurrent without a collector under illumination and a negative bias (Fig. 16d) [362]. The synergistic effect of the electrolyte and the negative bias will induce a greater degree of band bending, and an inversion layer dominated by minority electrons will appear in the depletion region when the Fermi level traverses the CB. The authors stated that the inversion layer not only reduces the recombination of photogenerated carriers but also allows lateral electron transport over a longer distance, $2\ \mathrm{cm} >> (L_e + D)$ [362]. Furthermore, a capacitance–voltage measurement revealed that the light-driven transition from depletion to inversion conditions occurred at approximately 0.6 V vs. RHE (Fig. 16e) [362]. These findings are valuable for the optimal design of MIS-type photoelectrode structures, the management of carrier transport and the selection of operating potentials.

Note that n-type semiconductors with wide band gaps, such as $SrTiO_3$ (STO) and TiO_2, can also be used as insulator components in MIS systems. Benefiting from the CB alignment and lattice matching between $SrTiO_3$ and Si, Ji et al. reported that a thin epitaxial layer of single-crystalline $SrTiO_3$ grown directly on Si(001) was used as an insulator in an MIS photocathode (Fig. 16f) [363]. The Pt/Ti/$SrTiO_3$/p-Si(001) photocathode has been proven to exhibit a much superior performance when the thickness of the insulator is 1.6 nm (Fig. 16g), achieving a remarkable photocurrent density of 35 mA cm^{-2} at 0.5 V vs. normal hydrogen electrode (NHE), an OCP of 450 mV and a long-term stability of over 35 h under AM 1.5G illumination [363]. Similarly, our group recently reported an efficient MIS-type photoanode with the RuO_x/Al_2O_3/Sn-doped Fe_2O_3 configuration (Fig. 16h), in which amorphous Al_2O_3 is used as an insulating layer and RuO_x as a hole collector, producing a superior IPCE of 52.0% under 370 nm irradiation at − 1.2 V vs. Ag/AgCl and a QE of 5.7% under 450 nm irradiation [364]. The photoanode was proven to have the optimal performance when the thickness of Al_2O_3 is 3 nm. However, the ultrathin insulating layer is detrimental to the long-term stability of the photoelectrode. Therefore, different from the ultrathin tunnelling layer (Fig. 16i), Li et al. applied a thick insulating layer with localized dielectric breakdown to the MIS-type photoelectrode (Fig. 16j), achieving decoupling of the trade-off between stability and low-resistance carrier transport as required for efficiency [365]. Great enhancement of the photocurrent after dielectric breakdown was proven to be possible. This approach effectively reduces the threshold for preparing MIS-type photoelectrodes and shows promise for applications.

McIntyre et al. reported a MIS-type photoanode with TiO_2 as a tunnel oxide and metallic Ir as an electrocatalyst for the OER, achieving an inferred photovoltage of approximately 550 mV [71]. Afterwards, Wang and coworkers constructed a modified inverted-MIS (I-MIS) architecture to reduce or eliminate detrimental parasitic light absorption by employing a bifacial passivation strategy with a long minority carrier lifetime (2 360 µs) (Fig. 16k) [59]. Compared with the onset potential of conventional n^{++}/TiO_2/Pt, the photovoltage of the Si I-MIS photocathode is enhanced by 620 mV (Fig. 16l), achieving an outstanding ABPE of 12.66% and a long-term operation stability of at least 108 h [59]. Our group expanded the effective application of the MIS architecture in organic semiconductors, such as the COFs and small molecules reviewed in the above section. We employed the self-assembly strategy induced by an electrostatic field to construct an MIS photosystem with polyvinylpyrrolidone (PVP)-capped Pt nanoparticles and a D-A-type TP-COF configuration, where the ultrathin PVP layer was used as an organic polymer insulator and Pt as an electron collector (Fig. 16m) [269]. Furthermore, we

recently reported another MIS-type photosystem based on electrostatic self-assembly of supramolecular bis(4-ethynyl-bridging (*N*-sodium hexanoate) 1,8-naphthalimide) bolaamphiphile (BENI-COO^- and BENI-NH_3^+) semiconductors and an opposite-charged DuBois-Ni catalyst for the HER (Fig. 16n) [272]. More specifically, the electrons tunnel from the semiconducting BENI-based light absorbers to the DuBois-Ni collector across the long-distance (2.2–2.5 nm) insulator that is provided by the alkyl region (Fig. 16n). These expanded studies of organic semiconductor photosystems based on the MIS architecture are conducive to wider and deeper applications of the quantum tunnelling effect in artificial photoelectrodes.

6.10 Benchmark Principles for the Design of Tandem Photoelectrodes and PEC Systems

Efficient light absorption of PEC devices is a prerequisite for converting dispersed low-quality solar energy into high-energy-density hydrogen energy. Generally, there is a trade-off between the narrow band gap semiconductor that is conducive to light absorption and the wide band gap semiconductor that is favourable for delivering a higher photovoltage. Fabricating efficient tandem photoelectrodes with a broad absorption range by compounding gradient band gap semiconductors is a common strategy. Since the incident light rapidly decays with the layers and thicknesses of the semiconductors it passes through, optimizing the band gap gradient, thicknesses and interface of the top and bottom junction semiconductors is key to achieving effective light absorption of tandem photoelectrodes. In this regard, Deutsch et al. demonstrated a classic design procedure with III–V compounds [366]. The theoretical STH isoefficiency contour plot of the top and bottom junction band gaps is shown in Fig. 17a, assuming ideal light absorption, 800 mV total overvoltage loss and a 0.2-cm-thick water film [366]. For example, the top/bottom photocathode configuration with 1.8/1.2 eV band gaps can achieve a remarkable η_{STH} of ca. 24% (orange dot), while the typical $Ga_{0.51}In_{0.49}P$/GaAs tandem can reach $\eta_{STH} = 15\%$ (black dot) (Fig. 17a). Note that, benefiting from the flexible structure of phosphide ($Ga_xIn_{1-x}P$) and arsenide ($Ga_xIn_{1-x}As$, $Al_xGa_{1-x}As$), $Ga_{0.51}In_{0.49}P$ and GaAs exhibit excellent lattice matching (Fig. 17b). The tandem heterojunction with superior lattice matching cannot only reduce the interface impedance and capacitive reactance but also contribute to elimination of interface recombination of photogenerated carriers. Theoretically, the maximum $\eta_{STH} = 27\%$ at 1.7 and 1.05 eV can potentially be achieved by tuning the band gaps of $Al_xGa_{1-x}As$ (top absorber) and $Ga_xIn_{1-x}As$ (bottom absorber), but lattice mismatch may be the dominant factor limiting the practical application (Fig. 17a and b) [366]. In view of this, they constructed an exemplary tandem photocathode with a $Ga_{0.51}In_{0.49}P/Ga_{0.89}In_{0.11}As$ (GaInP/GaInAs, the band gaps are 1.8/1.2 eV) architecture and a lattice mismatch of 0.8% (Fig. 17b and c), featuring a transparent graded buffer layer to allow the band gaps of each junction to be independently varied and a transparent TJ to connect the GaInP photovoltage (V_{ph1}) and GaInAs photovoltage (V_{ph2}) in series [366]. More specifically, the incident photons with $h\nu > 1.8$ eV are absorbed by top GaInP, while the photons with $1.8\,eV > h\nu > 1.2$ eV are absorbed by bottom GaInAs, where the holes in the GaInAs VB recombine (yellow dot) with the electrons in the GaInAs CB at the TJ (Fig. 17c) [366]. The overall photovoltage of the tandem photocathode with the *Z*-scheme junction is the sum of V_{ph1} and V_{ph2}. Notably, the contribution of the *Z*-scheme heterojunction to PVs is superior to that of the type-II heterojunction because of its smaller PV loss.

In addition to the band gap and lattice matching discussed above, the gradient and alignment of the band edges should be considered for multilayer tandem photoelectrodes. Generally, in a typical multilayer type-II heterojunction tandem photoelectrode (Fig. 18d and e), the CB electrons are transmitted from the bottom semiconductor to the top semiconductor under the driving force of a band edge difference or an applied bias, while the VB holes are transmitted in the opposite direction. However, the effective separation of photogenerated carriers in this architecture comes at the expense of photovoltage because both electrons and holes migrate in the direction of decreasing electric potential or chemical potential. The most ideal method is *Z*-scheme recombination at heterointerfaces without sacrificing the photovoltage, such as the recombination at the TJ discussed above (Fig. 18c) and the recombination in $TiO_2/MAPbI_3$/Spiro-MeOTAD-based tandem perovskite solar cells used by Moon et al. (Fig. 17e) [367]. Therefore, the band gaps and band edges of the current semiconductors commonly used in photocathodes must be tuned to simultaneously obtain high photovoltage and efficient photogenerated carrier separation (Fig. 18).

For the tandem solar water splitting system composed of a photocathode and a photoanode, in principle, each photoelectrode must exhibit a superior onset potential and a high photocurrent density. Only in this way can an outstanding performance of the tandem system for water splitting be achieved because the operating point is jointly determined by the performance of the two photoelectrodes. In this regard, Reisner et al. recently demonstrated a valuable example: an integrated bias-free tandem PEC system was constructed by coupling a perovskite-hydrogenase (H_2ase) photocathode and a classical $BiVO_4$ photoanode (Fig. 17f) [368]. The photocurrent density at the operating point obtained by coupling a photocathode with a positive onset potential of + 0.8 V vs. RHE and a photoanode with a relatively negative onset potential of + 0.2 V vs. RHE was 1.4 mA cm^{-2}, achieving an STH conversion efficiency of 1.1% (Fig. 17g)

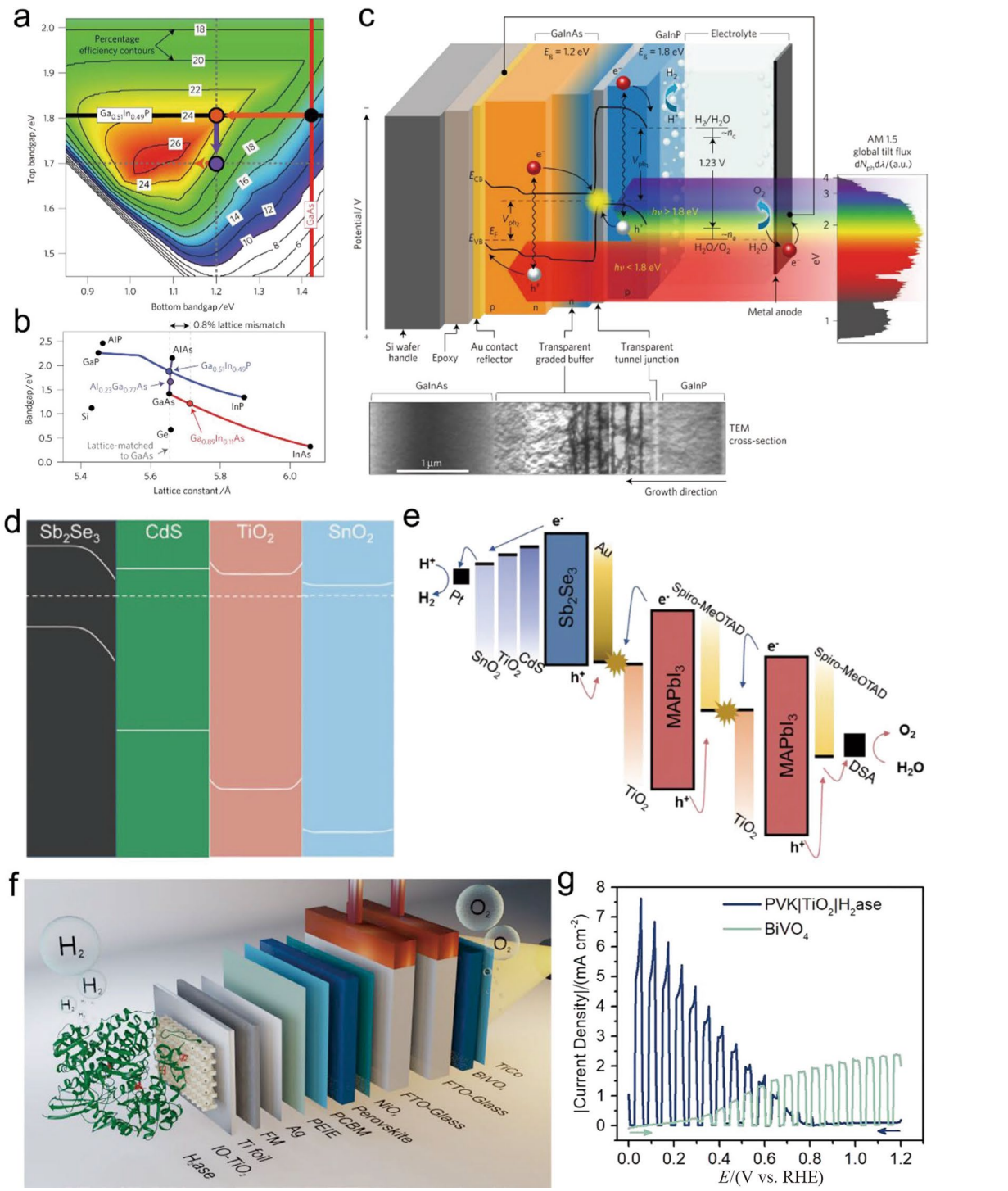

Fig. 17 Tandem photoelectrode and PEC systems. **a** STH isoefficiency contour plot of tandem photoelectrodes with the top and bottom junction band gaps. **b** Band gap versus lattice constant for various III–V alloys (1 Å = 1×10^{-10} m). **c** Architecture of a multijunction tandem photocathode configured for water splitting, and the cross-sectional TEM image of the active layers. Reprinted with permission from Ref. [366]. Copyright © 2017 Macmillan Publishers Limited, part of Springer Nature. **d** Equilibrium band alignment diagram of the Sb_2Se_3/CdS/TiO_2/SnO_2 heterojunction. **e** Energy potential diagram of the tandem device with the two PV cells and the PEC photocathode. Reprinted with permission from Ref. [367]. Copyright © 2020 The Royal Society of Chemistry. **f** Schematic representation of the tandem PEC cell consisting of an encapsulated perovskite photocathode with H_2ase integrated into an inverse opal (IO)-TiO_2 layer and a $BiVO_4$ photoanode. **g** Representative LSV curve of PVK|TiO_2|H_2ase (blue) and $BiVO_4$ (green) electrodes with chopped illumination. Reprinted with permission from Ref. [368]. Copyright © 2019 American Chemical Society

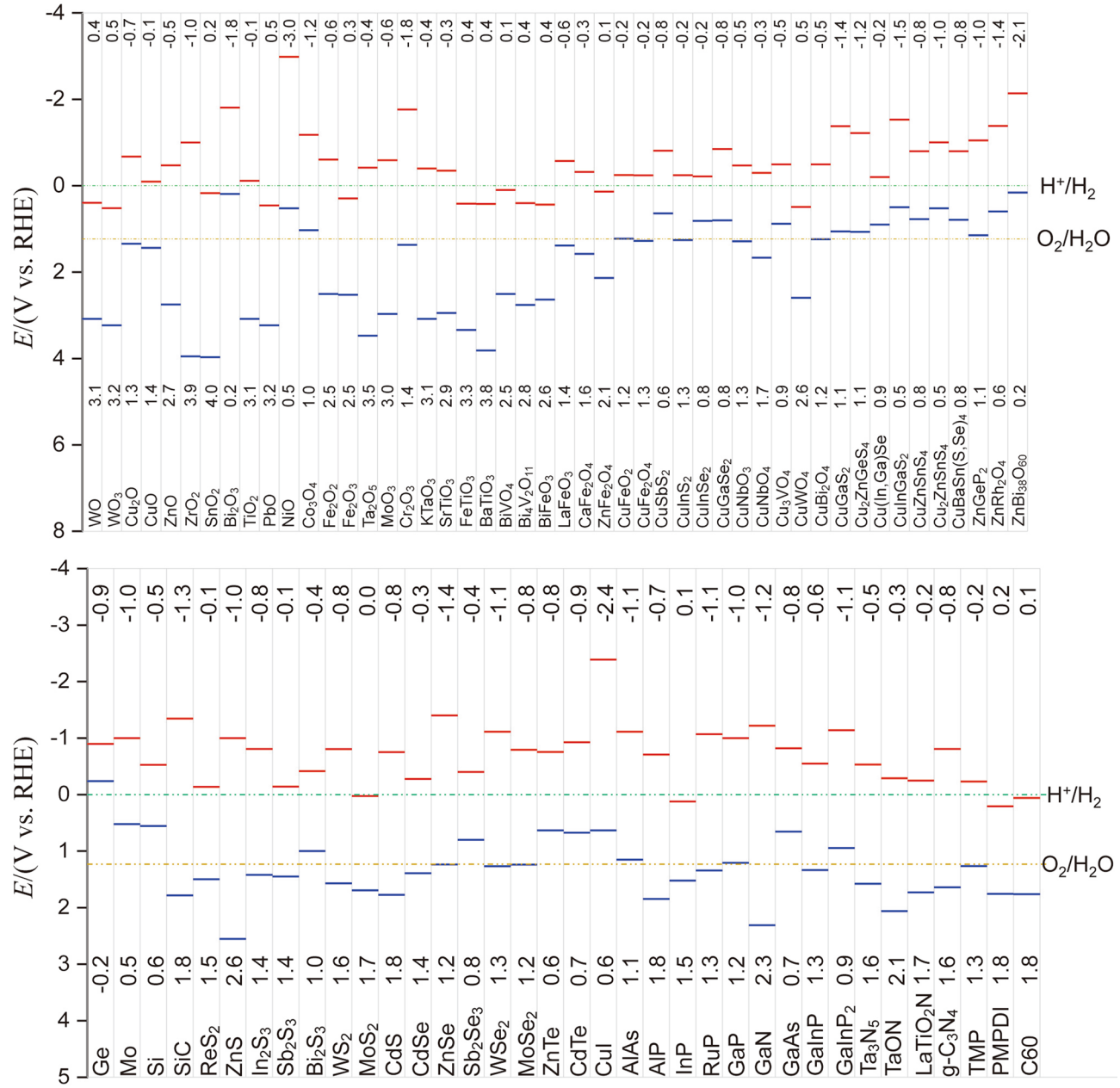

Fig. 18 Band diagram of semiconductors commonly used in photoelectrodes; note that the band edge error is ± 0.1 V, and the band gap error is ± 0.2 V

[368]. However, the energy conversion efficiency of 1.1% is still far from industrial application. The sustainable and efficient conversion of solar energy into hydrogen with industrial relevance in a low-cost and profitable way is the future development trend of tandem PEC systems (Table 1).

7 Conclusion and Outlook

This review summarized the state-of-the-art APSs for solar water splitting based on common and latest photocathode materials. Specifically, we focused on recent developments in photocathode architectures, semiconductor light absorbers and performance optimization strategies. The design cases of organic semiconductor photoelectrodes based on frontier (molecular) orbital theory and semiconductor energy band theory were elaborated in detail, suggesting that organic

Table 1 Series of recent devices used for unbiased water splitting and their η_{STH}

Device	Structural configuration	η_{STH} /(%)	Reference
IMM	GaInP/GaInAs	16.2	[361]
$MAPbI_3$; $MAPbBr_3$	$CH_3NH_3PbI_3$; $CH_3NH_3PbBr_3$	2.6; 6.3	[362]
Hydrogenase-Perovskite||$BiVO_4$	$BiVO_4$||PVK|TiO_2|H_2ase	1.1	[363]
CIGS	$CuIn_xGa_{1-x}Se_2$	6	[369]
PEC	Cu_2O/Ga_2O_3	3	[370]
PEC	$BiVO_4$–Sb_2Se_3	1.5	[219]
D_4-type	Mo:$BiVO_4$–SnS	1.7	[371]
PEC-PV	MoS_2/TiO_2	6.6	[372]
PEC-PV	NiFe/$BiVO_4/SnO_2$	7.3	[373]
PV-PEC	Ni NPs/$Ni(OH)_2$/n-Si	12	[374]

semiconductors with flexible structures and tuneable band gaps and band edges have promising application potential in APSs. Because insulators and wide band gap semiconductors are commonly used to decouple the trade-off between the stability and performance of light absorbers, we reviewed the application frontiers of MIS photoelectrodes that realize electron transfer through quantum tunnelling and believe that the performance of MIS photoelectrodes has much room for improvement via optimization of the architecture. The tandem photoelectrodes and PEC systems conforming to the solar spectrum nature are considered to be a cost-effective avenue with industrial relevance for solar-to-hydrogen conversion via solar water splitting. Therefore, we discussed the design benchmarks and protocols for integrated tandem photoelectrodes and PEC systems based on semiconductor energy band theory and engineering. Finally, we foresee that in the future, integrated unbiased solar-driven PEC water splitting for the production of renewable hydrogen will become an ideal option for sustainable solar storage.

Possible solutions to the current challenges in PEC hydrogen production include the following.

1. For Si and cuprous oxide with outstanding light capture ability and a high current density but an unstable photocathode, interface protection materials and electrode testing and packaging technology must be developed.
2. Tandem electrodes and systems are possible solutions to further improve the STH efficiency. For them, the matching of the band structure is a key factor, and it may be developed towards the Z-scheme heterojunction configuration with the lowest energy loss and the highest utilization efficiency.
3. Separation technology of photoabsorbers and electrodes may be one of the directions to further improve the energy conversion efficiency, such as constructing a system with high-efficiency solar cells as light absorbers and the most superior Pt as the electric cathode.
4. Optimizing the reactor design and enhancing the mass transfer and energy transfer capacity of the reactor is an effective way to further improve the energy conversion efficiency.
5. Based on the big data information of physics, chemistry and material properties, the construction of intelligent material screening systems and simulation assembly systems is one of the possible directions for further development of PEC hydrogen production.

Acknowledgements This work was supported by the National Key R&D Program of China (2018YFE0208500) and the National Natural Science Foundation of China (Grant Nos. 22072022, 21773031 and 22011530144).

References

1. Miller, E.L., Thompson, S.T., Randolph, K., et al.: US Department of Energy hydrogen and fuel cell technologies perspectives. MRS Bull. **45**, 57–64 (2020). https://doi.org/10.1557/mrs.2019.312
2. Kim, J.H., Hansora, D., Sharma, P., et al.: Toward practical solar hydrogen production–an artificial photosynthetic leaf-to-farm challenge. Chem. Soc. Rev. **48**, 1908–1971 (2019). https://doi.org/10.1039/c8cs00699g
3. Nikolaidis, P., Poullikkas, A.: A comparative overview of hydrogen production processes. Renew. Sustain. Energy Rev. **67**, 597–611 (2017). https://doi.org/10.1016/j.rser.2016.09.044
4. Dincer, I.: Green methods for hydrogen production. Int. J. Hydrog. Energy **37**, 1954–1971 (2012). https://doi.org/10.1016/j.ijhydene.2011.03.173
5. Lewis, N.S., Nocera, D.G.: Powering the planet: chemical challenges in solar energy utilization. Proc. Natl. Acad. Sci. U. S. A. **103**, 15729–15735 (2006). https://doi.org/10.1073/pnas.0603395103
6. Gray, H.B.: Powering the planet with solar fuel. Nat. Chem. **1**, 7–7 (2009). https://doi.org/10.1038/nchem.141
7. Nocera, D.G.: Solar fuels and solar chemicals industry. Acc. Chem. Res. **50**, 616–619 (2017). https://doi.org/10.1021/acs.accounts.6b00615
8. Stone, D.: Global warming: understanding the forecast. Bull. Am. Meteorol. Soc. **89**, 1381 (2008)
9. Looney, B.: Full report–BP statistical review of world energy 2021. (2021) https://www.bp.com/en/global/corporate/energy-economics/statistical-review-of-world-energy.html. Accessed 28 Feb 2022
10. Li, X.B., Tung, C.H., Wu, L.Z.: Semiconducting quantum dots for artificial photosynthesis. Nat. Rev. Chem. **2**, 160–173 (2018). https://doi.org/10.1038/s41570-018-0024-8
11. Blankenship, R.E., Tiede, D.M., Barber, J., et al.: Comparing photosynthetic and photovoltaic efficiencies and recognizing the potential for improvement. Science **332**, 805–809 (2011). https://doi.org/10.1126/science.1200165
12. Armaroli, N., Balzani, V.: Solar electricity and solar fuels: status and perspectives in the context of the energy transition. Chem. Eur. J. **22**, 32–57 (2016). https://doi.org/10.1002/chem.201503580
13. Roger, I., Shipman, M.A., Symes, M.D.: Earth-abundant catalysts for electrochemical and photoelectrochemical water

splitting. Nat. Rev. Chem. **1**, 0003 (2017). https://doi.org/10.1038/s41570-016-0003
14. Trasatti, S.: Work function, electronegativity, and electrochemical behaviour of metals: III. Electrolytic hydrogen evolution in acid solutions. J. Electroanal. Chem. Interfacial Electrochem. **39**, 163–184 (1972). https://doi.org/10.1016/S0022-0728(72)80485-6
15. Nørskov, J.K., Bligaard, T., Logadottir, A., et al.: Trends in the exchange current for hydrogen evolution. J. Electrochem. Soc. **152**, J23 (2005). https://doi.org/10.1149/1.1856988
16. Zhou, Y.G., Zhang, Z.Z., Fang, Z.W., et al.: Defect engineering of metal–oxide interface for proximity of photooxidation and photoreduction. Proc. Natl. Acad. Sci. U. S. A. **116**, 10232–10237 (2019). https://doi.org/10.1073/pnas.1901631116
17. Ma, R., Sun, J., Li, D.H., et al.: Review of synergistic photothermo-catalysis: mechanisms, materials and applications. Int. J. Hydrog. Energy **45**, 30288–30324 (2020). https://doi.org/10.1016/j.ijhydene.2020.08.127
18. Wang, Z., Roberts, R.R., Naterer, G.F., et al.: Comparison of thermochemical, electrolytic, photoelectrolytic and photochemical solar-to-hydrogen production technologies. Int. J. Hydrog. Energy **37**, 16287–16301 (2012). https://doi.org/10.1016/j.ijhydene.2012.03.057
19. Keller, N., Ivanez, J., Highfield, J., et al.: Photo-/ thermal synergies in heterogeneous catalysis: towards low-temperature (solar-driven) processing for sustainable energy and chemicals. Appl. Catal. B Environ. **296**, 120320 (2021). https://doi.org/10.1016/j.apcatb.2021.120320
20. Zeng, G., Pham, T.A., Vanka, S., et al.: Development of a photoelectrochemically self-improving Si/GaN photocathode for efficient and durable H_2 production. Nat. Mater. **20**, 1130–1135 (2021). https://doi.org/10.1038/s41563-021-00965-w
21. Siavash Moakhar, R., Hosseini-Hosseinabad, S.M., Masudy-Panah, S., et al.: Photoelectrochemical water-splitting using CuO-based electrodes for hydrogen production: a review. Adv. Mater. **33**, 2007285 (2021). https://doi.org/10.1002/adma.202007285
22. Pan, S.J., Li, R.J., Zhang, Q.X., et al.: An over 20% solar-to-hydrogen efficiency system comprising a self-reconstructed NiCoFe-based hydroxide nanosheet electrocatalyst and monolithic perovskite/silicon tandem solar cell. J. Mater. Chem. A **9**, 14085–14092 (2021). https://doi.org/10.1039/d1ta03126k
23. Guo, S., Li, X., Li, J., et al.: Boosting photocatalytic hydrogen production from water by photothermally induced biphase systems. Nat. Commun. **12**, 1343 (2021). https://doi.org/10.1038/s41467-021-21526-4
24. Rao, C.N.R., Dey, S.: Solar thermochemical splitting of water to generate hydrogen. Proc. Natl. Acad. Sci. U. S. A. **114**, 13385–13393 (2017). https://doi.org/10.1073/pnas.1700104114
25. White, J.L., Baruch, M.F., Pander Iii, J.E., et al.: Light-driven heterogeneous reduction of carbon dioxide: photocatalysts and photoelectrodes. Chem. Rev. **115**, 12888–12935 (2015). https://doi.org/10.1021/acs.chemrev.5b00370
26. He, Y., He, Q., Wang, L., et al.: Self-gating in semiconductor electrocatalysis. Nat. Mater. **18**, 1098–1104 (2019). https://doi.org/10.1038/s41563-019-0426-0
27. Jang, Y.J., Lee, J.S.: Photoelectrochemical water splitting with p-type metal oxide semiconductor photocathodes. Chemsuschem **12**, 1835–1845 (2019). https://doi.org/10.1002/cssc.201802596
28. Gelderman, K., Lee, L., Donne, S.W.: Flat-band potential of a semiconductor: using the Mott-Schottky equation. J. Chem. Educ. **84**, 685 (2007). https://doi.org/10.1021/ed084p685
29. Arbring Sjöström, T., Berggren, M., Gabrielsson, E.O., et al.: Iontronics: a decade of iontronic delivery devices. Adv. Mater. Technol. **3**, 1870018 (2018). https://doi.org/10.1002/admt.201870018
30. Varadhan, P., Fu, H.C., Kao, Y.C., et al.: An efficient and stable photoelectrochemical system with 9% solar-to-hydrogen conversion efficiency via InGaP/GaAs double junction. Nat. Commun. **10**, 5282 (2019). https://doi.org/10.1038/s41467-019-12977-x
31. Kibsgaard, J., Chorkendorff, I.: Considerations for the scaling-up of water splitting catalysts. Nat. Energy **4**, 430–433 (2019). https://doi.org/10.1038/s41560-019-0407-1
32. Andrei, V., Reuillard, B., Reisner, E.: Bias-free solar syngas production by integrating a molecular cobalt catalyst with perovskite–$BiVO_4$ tandem. Nat. Mater. **19**, 189–194 (2020). https://doi.org/10.1038/s41563-019-0501-6
33. Landman, A., Dotan, H., Shter, G.E., et al.: Photoelectrochemical water splitting in separate oxygen and hydrogen cells. Nat. Mater. **16**, 646–651 (2017). https://doi.org/10.1038/nmat4876
34. Kuhlmann, A.M.: The second most abundant element in the Earth's crust. JOM **15**, 502–505 (1963). https://doi.org/10.1007/BF03378936
35. Liu, C., Dasgupta, N.P., Yang, P.D.: Semiconductor nanowires for artificial photosynthesis. Chem. Mater. **26**, 415–422 (2014). https://doi.org/10.1021/cm4023198
36. Sim, U., Moon, J., Lee, J., et al.: Double-layer graphene outperforming monolayer as catalyst on silicon photocathode for hydrogen production. ACS Appl. Mater. Interfaces **9**, 3570–3580 (2017). https://doi.org/10.1021/acsami.6b11750
37. Lee, K., Hwang, I., Kim, N., et al.: 17.6%-Efficient radial junction solar cells using silicon nano/micro hybrid structures. Nanoscale **8**, 14473–14479 (2016). https://doi.org/10.1039/c6nr04611h
38. Vijselaar, W., Kunturu, P.P., Moehl, T., et al.: Tandem cuprous oxide/silicon microwire hydrogen-evolving photocathode with photovoltage exceeding 1.3 V. ACS Energy Lett. **4**, 2287–2294 (2019). https://doi.org/10.1021/acsenergylett.9b01402
39. Sagar, R., Rao, A.S.: Nanoscale TiO_2 and Ta_2O_5 as efficient antireflection coatings on commercial monocrystalline silicon solar cell. J. Alloys Compd. **862**, 158464 (2021). https://doi.org/10.1016/j.jallcom.2020.158464
40. Thalluri, S.M., Borme, J., Xiong, D.H., et al.: Highly-ordered silicon nanowire arrays for photoelectrochemical hydrogen evolution: an investigation on the effect of wire diameter, length and inter-wire spacing. Sustain. Energy Fuels **2**, 978–982 (2018). https://doi.org/10.1039/c7se00591a
41. Chen, C.J., Yeh, C.Y., Chen, C.H., et al.: Molybdenum tungsten disulfide with a large number of sulfur vacancies and electronic unoccupied states on silicon micropillars for solar hydrogen evolution. ACS Appl. Mater. Interfaces **12**, 54671–54682 (2020). https://doi.org/10.1021/acsami.0c15905
42. Kunturu, P.P., Zachariadis, C., Witczak, L., et al.: Tandem Si micropillar array photocathodes with conformal copper oxide and a protection layer by pulsed laser deposition. ACS Appl. Mater. Interfaces **11**, 41402–41414 (2019). https://doi.org/10.1021/acsami.9b14408
43. Liu, F., Thalluri, S.M.: Conformal and continuous deposition of bifunctional cobalt phosphide layers on p-silicon photocathodes for improved solar hydrogen evolution. ECS Meet. Abstr. **MA2019-01**, 1640 (2019). https://doi.org/10.1149/ma2019-01/31/1640
44. Shaner, M.R., McKone, J.R., Gray, H.B., et al.: Functional integration of Ni–Mo electrocatalysts with Si microwire array photocathodes to simultaneously achieve high fill factors and light-limited photocurrent densities for solar-driven hydrogen evolution. Energy Environ. Sci. **8**, 2977–2984 (2015). https://doi.org/10.1039/C5EE01076D
45. Su, Y., Liu, C., Brittman, S., et al.: Single-nanowire photoelectrochemistry. Nat. Nanotechnol. **11**, 609–612 (2016). https://doi.org/10.1038/nnano.2016.30
46. Sim, U., Moon, J., An, J., et al.: N-doped graphene quantum sheets on silicon nanowire photocathodes for hydrogen

production. Energy Environ. Sci. **8**, 1329–1338 (2015). https://doi.org/10.1039/C4EE03607G
47. Jia, Q., Yu, C., Liu, W., et al.: High performance n^+p-Si/Ti/NiS_xO_y photocathode for photoelectrochemical hydrogen evolution in alkaline solution. J. Energy Chem. **30**, 101–107 (2019). https://doi.org/10.1016/j.jechem.2018.04.004
48. Morales-Guio, C.G., Thorwarth, K., Niesen, B., et al.: Solar hydrogen production by amorphous silicon photocathodes coated with a magnetron sputter deposited Mo_2C catalyst. J. Am. Chem. Soc. **137**, 7035–7038 (2015). https://doi.org/10.1021/jacs.5b03417
49. Fan, R., Dong, W., Fang, L., et al.: More than 10% efficiency and one-week stability of Si photocathodes for water splitting by manipulating the loading of the Pt catalyst and TiO_2 protective layer. J. Mater. Chem. A **5**, 18744–18751 (2017). https://doi.org/10.1039/C7TA04986B
50. Fan, R., Tang, C., Xin, Y., et al.: Surface passivation and protection of Pt loaded multicrystalline pn^+ silicon photocathodes by atmospheric plasma oxidation for improved solar water splitting. Appl. Phys. Lett. **109**, 233901 (2016). https://doi.org/10.1063/1.4971359
51. Chen, F.J., Zhu, Q.S., Wang, Y.Y., et al.: Efficient photoelectrochemical hydrogen evolution on silicon photocathodes interfaced with nanostructured NiP_2 cocatalyst films. ACS Appl. Mater. Interfaces **8**, 31025–31031 (2016). https://doi.org/10.1021/acsami.6b11197
52. Edwards, M., Bowden, S., Das, U., et al.: Effect of texturing and surface preparation on lifetime and cell performance in heterojunction silicon solar cells. Sol. Energy Mater. Sol. Cells **92**, 1373–1377 (2008). https://doi.org/10.1016/j.solmat.2008.05.011
53. Hu, D., Xiang, J., Zhou, Q., et al.: One-step chemical vapor deposition of MoS_2 nanosheets on SiNWs as photocathodes for efficient and stable solar-driven hydrogen production. Nanoscale **10**, 3518–3525 (2018). https://doi.org/10.1039/C7NR09235K
54. Hellstern, T.R., Nielander, A.C., Chakthranont, P., et al.: Nanostructuring strategies to increase the photoelectrochemical water splitting activity of silicon photocathodes. ACS Appl. Nano Mater. **2**, 6–11 (2019). https://doi.org/10.1021/acsanm.8b01966
55. Yu, Y., Zhang, Z., Yin, X., et al.: Enhanced photoelectrochemical efficiency and stability using a conformal TiO_2 film on a black silicon photoanode. Nat. Energy **2**, 17045 (2017). https://doi.org/10.1038/nenergy.2017.45
56. Kang, D., Young, J.L., Lim, H., et al.: Printed assemblies of GaAs photoelectrodes with decoupled optical and reactive interfaces for unassisted solar water splitting. Nat. Energy **2**, 17043 (2017). https://doi.org/10.1038/nenergy.2017.43
57. Wang, Y., Schwartz, J., Gim, J., et al.: Stable unassisted solar water splitting on semiconductor photocathodes protected by multifunctional GaN nanostructures. ACS Energy Lett. **4**, 1541–1548 (2019). https://doi.org/10.1021/acsenergylett.9b00549
58. Choi, M.J., Jung, J.Y., Park, M.J., et al.: Long-term durable silicon photocathode protected by a thin Al_2O_3/SiO_x layer for photoelectrochemical hydrogen evolution. J. Mater. Chem. A **2**, 2928–2933 (2014). https://doi.org/10.1039/C3TA14443G
59. Liu, B., Feng, S., Yang, L., et al.: Bifacial passivation of n-silicon metal–insulator–semiconductor photoelectrodes for efficient oxygen and hydrogen evolution reactions. Energy Environ. Sci. **13**, 221–228 (2020). https://doi.org/10.1039/C9EE02766A
60. Liu, R., Zheng, Z., Spurgeon, J., et al.: Enhanced photoelectrochemical water-splitting performance of semiconductors by surface passivation layers. Energy Environ. Sci. **7**, 2504–2517 (2014). https://doi.org/10.1039/C4EE00450G
61. Thalluri, S.M., Wei, B., Welter, K., et al.: Inverted pyramid textured p-silicon covered with Co_2P as an efficient and stable solar hydrogen evolution photocathode. ACS Energy Lett. **4**, 1755–1762 (2019). https://doi.org/10.1021/acsenergylett.9b00964
62. Vijselaar, W., Tiggelaar, R.M., Gardeniers, H., et al.: Efficient and stable silicon microwire photocathodes with a nickel silicide interlayer for operation in strongly alkaline solutions. ACS Energy Lett. **3**, 1086–1092 (2018). https://doi.org/10.1021/acsenergylett.8b00267
63. Ku, C.K., Wu, P.H., Chung, C.C., et al.: Creation of 3D textured graphene/Si Schottky junction photocathode for enhanced photoelectrochemical efficiency and stability. Adv. Energy Mater. **9**, 1901022 (2019). https://doi.org/10.1002/aenm.201901022
64. Jun, S.E., Choi, S., Choi, S., et al.: Direct synthesis of molybdenum phosphide nanorods on silicon using graphene at the heterointerface for efficient photoelectrochemical water reduction. Nano-Micro Lett. **13**, 81 (2021). https://doi.org/10.1007/s40820-021-00605-7
65. Wu, Y., Gong, M., Lin, M.C., et al.: 3D graphitic foams derived from chloroaluminate anion intercalation for ultrafast aluminum-ion battery. Adv. Mater. **28**, 9218–9222 (2016). https://doi.org/10.1002/adma.201602958
66. Zheng, J., Lyu, Y., Wang, R., et al.: Crystalline TiO_2 protective layer with graded oxygen defects for efficient and stable silicon-based photocathode. Nat. Commun. **9**, 3572 (2018). https://doi.org/10.1038/s41467-018-05580-z
67. Wang, Q., Hisatomi, T., Jia, Q., et al.: Scalable water splitting on particulate photocatalyst sheets with a solar-to-hydrogen energy conversion efficiency exceeding 1%. Nat. Mater. **15**, 611–615 (2016). https://doi.org/10.1038/nmat4589
68. Dominey, R.N., Lewis, N.S., Bruce, J.A., et al.: Improvement of photoelectrochemical hydrogen generation by surface modification of p-type silicon semiconductor photocathodes. J. Am. Chem. Soc. **104**, 467–482 (1982). https://doi.org/10.1021/ja00366a016
69. Wang, T., Liu, S., Li, H., et al.: Transparent Ta_2O_5 protective layer for stable silicon photocathode under full solar spectrum. Ind. Eng. Chem. Res. **58**, 5510–5515 (2019). https://doi.org/10.1021/acs.iecr.9b00147
70. Lin, Y., Battaglia, C., Boccard, M., et al.: Amorphous Si thin film based photocathodes with high photovoltage for efficient hydrogen production. Nano Lett. **13**, 5615–5618 (2013). https://doi.org/10.1021/nl403265k
71. Chen, Y.W., Prange, J.D., Dühnen, S., et al.: Atomic layer-deposited tunnel oxide stabilizes silicon photoanodes for water oxidation. Nat. Mater. **10**, 539–544 (2011). https://doi.org/10.1038/nmat3047
72. Fan, R., Mao, J., Yin, Z., et al.: Efficient and stable silicon photocathodes coated with vertically standing nano-MoS_2 films for solar hydrogen production. ACS Appl. Mater. Interfaces **9**, 6123–6129 (2017). https://doi.org/10.1021/acsami.6b15854
73. Fan, R., Dong, W., Fang, L., et al.: Stable and efficient multicrystalline n^+p silicon photocathode for H_2 production with pyramid-like surface nanostructure and thin Al_2O_3 protective layer. Appl. Phys. Lett. **106**, 013902 (2015). https://doi.org/10.1063/1.4905511
74. Oh, S., Kim, J.B., Song, J.T., et al.: Atomic layer deposited molybdenum disulfide on Si photocathodes for highly efficient photoelectrochemical water reduction reaction. J. Mater. Chem. A **5**, 3304–3310 (2017). https://doi.org/10.1039/C6TA10707A
75. Yang, C., Barrelet, C.J., Capasso, F., et al.: Single p-type/intrinsic/n-type silicon nanowires as nanoscale avalanche photodetectors. Nano Lett. **6**, 2929–2934 (2006). https://doi.org/10.1021/nl062314b
76. Lehmann, V., Ronnebeck, S.: The physics of macropore formation in low-doped p-type silicon. J. Electrochem. Soc. **146**, 2968–2975 (1999). https://doi.org/10.1149/1.1392037
77. Hijazi, H., Monier, G., Gil, E., et al.: Si doping of vapor–liquid–solid GaAs nanowires: n-type or p-type? Nano Lett. **19**, 4498–4504 (2019). https://doi.org/10.1021/acs.nanolett.9b01308

78. Jiang, C., Moniz, S.J.A., Wang, A., et al.: Photoelectrochemical devices for solar water splitting–materials and challenges. Chem. Soc. Rev. **46**, 4645–4660 (2017). https://doi.org/10.1039/C6CS00306K
79. Chu, S., Li, W., Yan, Y., et al.: Roadmap on solar water splitting: current status and future prospects. Nano Futures **1**, 022001 (2017). https://doi.org/10.1088/2399-1984/aa88a1
80. Hu, S., Shaner, M.R., Beardslee, J.A., et al.: Amorphous TiO_2 coatings stabilize Si, GaAs, and GaP photoanodes for efficient water oxidation. Science **344**, 1005 (2014). https://doi.org/10.1126/science.1251428
81. Benck, J.D., Lee, S.C., Fong, K.D., et al.: Designing active and stable silicon photocathodes for solar hydrogen production using molybdenum sulfide nanomaterials. Adv. Energy Mater. **4**, 1400739 (2014). https://doi.org/10.1002/aenm.201400739
82. Boettcher, S.W., Warren, E.L., Putnam, M.C., et al.: Photoelectrochemical hydrogen evolution using Si microwire arrays. J. Am. Chem. Soc. **133**, 1216–1219 (2011). https://doi.org/10.1021/ja108801m
83. Zhang, D., Du, M., Wang, P., et al.: Hole-storage enhanced a-Si photocathodes for efficient hydrogen production. Angew. Chem. Int. Ed. **60**, 11966–11972 (2021). https://doi.org/10.1002/anie.202100078
84. Oyama, K., Ri, S.G., Kato, H., et al.: High performance of diamond p^+-i-n^+ junction diode fabricated using heavily doped p^+ and n^+ layers. Appl. Phys. Lett. **94**, 152109 (2009). https://doi.org/10.1063/1.3120560
85. Huang, W.C., Lei, T.F., Lee, C.L.: PtGe ohmic contact to n-type InP. J. Appl. Phys. **78**, 6108–6112 (1995). https://doi.org/10.1063/1.360552
86. Zeng, A., Yin, Y., Bilek, M., et al.: Ohmic contact to nitrogen doped amorphous carbon films. Surf. Coat. Technol. **198**, 202–205 (2005). https://doi.org/10.1016/j.surfcoat.2004.10.038
87. Wang, X., Jie, W., Li, H., et al.: Effects of low-temperature annealing on ohmic contact of Au/p-CdZnTe. Nucl. Instrum. Methods. Phys. Res. B **560**, 409–412 (2006). https://doi.org/10.1016/j.nima.2005.12.251
88. Alarawi, A., Ramalingam, V., Fu, H.C., et al.: Enhanced photoelectrochemical hydrogen production efficiency of MoS_2-Si heterojunction. Opt. Express **27**, A352–A363 (2019). https://doi.org/10.1364/OE.27.00A352
89. Cui, W., Niu, W., Wick-Joliat, R., et al.: Operando deconvolution of photovoltaic and electrocatalytic performance in ALD TiO_2 protected water splitting photocathodes. Chem. Sci. **9**, 6062–6067 (2018). https://doi.org/10.1039/C8SC01453A
90. Laskowski, F.A.L., Nellist, M.R., Qiu, J., et al.: Metal oxide/(oxy)hydroxide overlayers as hole collectors and oxygen-evolution catalysts on water-splitting photoanodes. J. Am. Chem. Soc. **141**, 1394–1405 (2019). https://doi.org/10.1021/jacs.8b09449
91. Wick-Joliat, R., Musso, T., Prabhakar, R.R., et al.: Stable and tunable phosphonic acid dipole layer for band edge engineering of photoelectrochemical and photovoltaic heterojunction devices. Energy Environ. Sci. **12**, 1901–1909 (2019). https://doi.org/10.1039/C9EE00748B
92. Ma, Q., Li, M., Pang, L., et al.: Solar-to-hydrogen efficiency of 9.5% by using a thin-layer platinum catalyst and commercial amorphous silicon solar cells. ChemCatChem **8**, 1713–1717 (2016). https://doi.org/10.1002/cctc.201600170
93. Reece, S.Y., Hamel, J.A., Sung, K., et al.: Wireless solar water splitting using silicon-based semiconductors and earth-abundant catalysts. Science **334**, 645–648 (2011). https://doi.org/10.1126/science.1209816
94. Liang, J.H., Tan, H.R., Liu, M., et al.: A thin-film silicon based photocathode with a hydrogen doped TiO_2 protection layer for solar hydrogen evolution. J. Mater. Chem. A **4**, 16841–16848 (2016). https://doi.org/10.1039/c6ta07701c
95. Fu, H.C., Varadhan, P., Lin, C.H., et al.: Spontaneous solar water splitting with decoupling of light absorption and electrocatalysis using silicon back-buried junction. Nat. Commun. **11**, 3930 (2020). https://doi.org/10.1038/s41467-020-17660-0
96. Vanka, S., Arca, E., Cheng, S., et al.: High efficiency Si photocathode protected by multifunctional GaN nanostructures. Nano Lett. **18**, 6530–6537 (2018). https://doi.org/10.1021/acs.nanolett.8b03087
97. Wu, L.L., Tsui, L.K., Swami, N., et al.: Photoelectrochemical stability of electrodeposited Cu_2O films. J. Phys. Chem. C **114**, 11551–11556 (2010). https://doi.org/10.1021/jp103437y
98. Paracchino, A., Laporte, V., Sivula, K., et al.: Highly active oxide photocathode for photoelectrochemical water reduction. Nat. Mater. **10**, 456–461 (2011). https://doi.org/10.1038/nmat3017
99. Nakaoka, K., Ueyama, J., Ogura, K.: Photoelectrochemical behavior of electrodeposited CuO and Cu_2O thin films on conducting substrates. J. Electrochem. Soc. **151**, C661 (2004). https://doi.org/10.1149/1.1789155
100. Nozik, A.J., Memming, R.: Physical chemistry of semiconductor–liquid interfaces. J. Phys. Chem. **100**, 13061–13078 (1996). https://doi.org/10.1021/jp953720e
101. Nozik, A.J.: Photochemical diodes. Appl. Phys. Lett. **30**, 567–569 (1977). https://doi.org/10.1063/1.89262
102. Tsubomura, H., Nakato, Y., Hiramoto, M., et al.: Metal oxide coated p–n junction silicon electrodes for photoelectrochemical solar energy conversion. Can. J. Chem. **63**, 1759–1762 (1985). https://doi.org/10.1139/v85-295
103. Mei, B., Seger, B., Pedersen, T., et al.: Protection of p^+-n-Si photoanodes by sputter-deposited Ir/IrO_x thin films. J. Phys. Chem. Lett. **5**, 1948–1952 (2014). https://doi.org/10.1021/jz500865g
104. Nakato, Y., Hiramoto, M., Iwakabe, Y., et al.: ESCA and photoelectrochemical studies of p–n junction silicon electrodes protected by platinum deposition for use in solar energy conversion. J. Electrochem. Soc. **132**, 330–334 (1985). https://doi.org/10.1149/1.2113832
105. Nakato, Y., Tsubomura, H.: Structures and functions of thin metal layers on semiconductor electrodes. J. Photochem. **29**, 257–266 (1985). https://doi.org/10.1016/0047-2670(85)87076-3
106. Mubeen, S., Lee, J., Singh, N., et al.: Stabilizing inorganic photoelectrodes for efficient solar-to-chemical energy conversion. Energy Environ. Sci. **6**, 1633–1639 (2013). https://doi.org/10.1039/c3ee40258d
107. Bansal, A., Lewis, N.S.: Stabilization of Si photoanodes in aqueous electrolytes through surface alkylation. J. Phys. Chem. B **102**, 4058–4060 (1998). https://doi.org/10.1021/jp980679h
108. Noufi, R., Frank, A.J., Nozik, A.J.: Stabilization of n-type silicon photoelectrodes to surface oxidation in aqueous electrolyte solution and mediation of oxidation reaction by surface-attached organic conducting polymer. J. Am. Chem. Soc. **103**, 1849–1850 (1981). https://doi.org/10.1021/ja00397a050
109. Ghijsen, J., Tjeng, L.H., van Elp, J., et al.: Electronic structure of Cu_2O and CuO. Phys. Rev. B Condens. Matter **38**, 11322–11330 (1988). https://doi.org/10.1103/physrevb.38.11322
110. Meyer, B.K., Polity, A., Reppin, D., et al.: Binary copper oxide semiconductors: from materials towards devices. Phys. Status Solidi B **249**, 1487–1509 (2012). https://doi.org/10.1002/pssb.201248128
111. Wang, Y., Lany, S., Ghanbaja, J., et al.: Electronic structures of Cu_2O, Cu_4O_3 and CuO: a joint experimental and theoretical study. Phys. Rev. B **94**, 245418 (2016). https://doi.org/10.1103/PhysRevB.94.245418
112. Li, Y., Luo, K.: Flexible cupric oxide photocathode with enhanced stability for renewable hydrogen energy production from solar water splitting. RSC Adv. **9**, 8350–8354 (2019). https://doi.org/10.1039/C9RA00865A

113. Jang, Y.J., Jang, J.W., Choi, S.H., et al.: Tree branch-shaped cupric oxide for highly effective photoelectrochemical water reduction. Nanoscale **7**, 7624–7631 (2015). https://doi.org/10.1039/C5NR00208G
114. Lee, J.G., Kim, D.Y., Lee, J.H., et al.: Scalable binder-free supersonic cold spraying of nanotextured cupric oxide (CuO) films as efficient photocathodes. ACS Appl. Mater. Interfaces **8**, 15406–15414 (2016). https://doi.org/10.1021/acsami.6b03968
115. Masudy-Panah, S., Siavash Moakhar, R., Chua, C.S., et al.: Nanocrystal engineering of sputter-grown CuO photocathode for visible-light-driven electrochemical water splitting. ACS Appl. Mater. Interfaces **8**, 1206–1213 (2016). https://doi.org/10.1021/acsami.5b09613
116. Han, J.F., Zong, X., Zhou, X., et al.: Cu_2O/CuO photocathode with improved stability for photoelectrochemical water reduction. RSC Adv. **5**, 10790–10794 (2015). https://doi.org/10.1039/c4ra13896a
117. Yang, Y., Xu, D., Wu, Q., et al.: Cu_2O/CuO bilayered composite as a high-efficiency photocathode for photoelectrochemical hydrogen evolution reaction. Sci. Rep. **6**, 35158 (2016). https://doi.org/10.1038/srep35158
118. Dubale, A.A., Pan, C.J., Tamirat, A.G., et al.: Heterostructured Cu_2O/CuO decorated with nickel as a highly efficient photocathode for photoelectrochemical water reduction. J. Mater. Chem. A **3**, 12482–12499 (2015). https://doi.org/10.1039/c5ta01961c
119. Guo, X., Diao, P., Xu, D., et al.: CuO/Pd composite photocathodes for photoelectrochemical hydrogen evolution reaction. Int. J. Hydrog. Energy **39**, 7686–7696 (2014). https://doi.org/10.1016/j.ijhydene.2014.03.084
120. Zhang, Z.H., Wang, P.: Highly stable copper oxide composite as an effective photocathode for water splitting via a facile electrochemical synthesis strategy. J. Mater. Chem. **22**, 2456–2464 (2012). https://doi.org/10.1039/c1jm14478b
121. Huang, Q., Kang, F., Liu, H., et al.: Highly aligned Cu_2O/CuO/TiO_2 core/shell nanowire arrays as photocathodes for water photoelectrolysis. J. Mater. Chem. A **1**, 2418–2425 (2013). https://doi.org/10.1039/c2ta00918h
122. Wang, P., Ng, Y.H., Amal, R.: Embedment of anodized p-type Cu_2O thin films with CuO nanowires for improvement in photoelectrochemical stability. Nanoscale **5**, 2952–2958 (2013). https://doi.org/10.1039/c3nr34012k
123. Lumley, M., Radmilovic, A., Jang, Y.J., et al.: Perspectives on the development of oxide-based photocathodes for solar fuel production. J. Am. Chem. Soc. **141**, 18358–18369 (2019). https://doi.org/10.1021/jacs.9b07976
124. Emin, S., Abdi, F.F., Fanetti, M., et al.: A novel approach for the preparation of textured CuO thin films from electrodeposited CuCl and CuBr. J. Electroanal. Chem. **717**(718), 243–249 (2014). https://doi.org/10.1016/j.jelechem.2014.01.038
125. Septina, W., Prabhakar, R.R., Wick, R., et al.: Stabilized solar hydrogen production with CuO/CdS heterojunction thin film photocathodes. Chem. Mater. **29**, 1735–1743 (2017). https://doi.org/10.1021/acs.chemmater.6b05248
126. Tilley, S.D., Schreier, M., Azevedo, J., et al.: Ruthenium oxide hydrogen evolution catalysis on composite cuprous oxide water-splitting photocathodes. Adv. Funct. Mater. **24**, 303–311 (2014). https://doi.org/10.1002/adfm.201301106
127. Luo, J.S., Steier, L., Son, M.K., et al.: Cu_2O nanowire photocathodes for efficient and durable solar water splitting. Nano Lett. **16**, 1848–1857 (2016). https://doi.org/10.1021/acs.nanolett.5b04929
128. Minami, T., Nishi, Y., Miyata, T.: Effect of the thin Ga_2O_3 layer in n^+-ZnO/n-Ga_2O_3/p-Cu_2O heterojunction solar cells. Thin Solid Films **549**, 65–69 (2013). https://doi.org/10.1016/j.tsf.2013.06.038
129. Minami, T., Nishi, Y., Miyata, T.: High-efficiency Cu_2O-based heterojunction solar cells fabricated using a Ga_2O_3Thin film as N-type layer. Appl. Phys. Express **6**, 044101 (2013). https://doi.org/10.7567/apex.6.044101
130. Lee, Y.S., Chua, D., Brandt, R.E., et al.: Atomic layer deposited gallium oxide buffer layer enables 1.2 V open-circuit voltage in cuprous oxide solar cells. Adv. Mater. **26**, 4704–4710 (2014). https://doi.org/10.1002/adma.201401054
131. Pan, L., Kim, J.H., Mayer, M.T., et al.: Boosting the performance of Cu_2O photocathodes for unassisted solar water splitting devices. Nat. Catal. **1**, 412–420 (2018). https://doi.org/10.1038/s41929-018-0077-6
132. Son, M.K., Steier, L., Schreier, M., et al.: A copper nickel mixed oxide hole selective layer for Au-free transparent cuprous oxide photocathodes. Energy Environ. Sci. **10**, 912–918 (2017). https://doi.org/10.1039/c6ee03613a
133. Azevedo, J., Steier, L., Dias, P., et al.: On the stability enhancement of cuprous oxide water splitting photocathodes by low temperature steam annealing. Energy Environ. Sci. **7**, 4044–4052 (2014). https://doi.org/10.1039/c4ee02160f
134. Azevedo, J., Tilley, S.D., Schreier, M., et al.: Tin oxide as stable protective layer for composite cuprous oxide water-splitting photocathodes. Nano Energy **24**, 10–16 (2016). https://doi.org/10.1016/j.nanoen.2016.03.022
135. Paracchino, A., Mathews, N., Hisatomi, T., et al.: Ultrathin films on copper(I) oxide water splitting photocathodes: a study on performance and stability. Energy Environ. Sci. **5**, 8673–8681 (2012). https://doi.org/10.1039/C2EE22063F
136. Stern, L.A., Liardet, L., Mayer, M.T., et al.: Photoelectrochemical deposition of CoP on cuprous oxide photocathodes for solar hydrogen production. Electrochim. Acta **235**, 311–316 (2017). https://doi.org/10.1016/j.electacta.2017.03.074
137. Morales-Guio, C.G., Tilley, S.D., Vrubel, H., et al.: Hydrogen evolution from a copper(I) oxide photocathode coated with an amorphous molybdenum sulphide catalyst. Nat. Commun. **5**, 3059 (2014). https://doi.org/10.1038/ncomms4059
138. Pan, L., Liu, Y., Yao, L., et al.: Cu_2O photocathodes with band-tail states assisted hole transport for standalone solar water splitting. Nat. Commun. **11**, 318 (2020). https://doi.org/10.1038/s41467-019-13987-5
139. Niu, W., Moehl, T., Cui, W., et al.: Extended light harvesting with dual Cu_2O-based photocathodes for high efficiency water splitting. Adv. Energy Mater. **8**, 1702323 (2018). https://doi.org/10.1002/aenm.201702323
140. Wang, Y.C., Qin, C., Lou, Z.-R., et al.: Cu_2O photocathodes for unassisted solar water-splitting devices enabled by noble-metal cocatalysts simultaneously as hydrogen evolution catalysts and protection layers. Nanotechnology **30**, 495407 (2019). https://doi.org/10.1088/1361-6528/ab40e8
141. Li, C., Hisatomi, T., Watanabe, O., et al.: Positive onset potential and stability of Cu_2O-based photocathodes in water splitting by atomic layer deposition of a Ga_2O_3 buffer layer. Energy Environ. Sci. **8**, 1493–1500 (2015). https://doi.org/10.1039/C5EE00250H
142. Li, C., Hisatomi, T., Watanabe, O., et al.: Simultaneous enhancement of photovoltage and charge transfer in Cu_2O-based photocathode using buffer and protective layers. Appl. Phys. Lett. **109**, 033902 (2016). https://doi.org/10.1063/1.4959098
143. Li, Y., Zhong, X.L., Luo, K., et al.: A hydrophobic polymer stabilized p-Cu_2O nanocrystal photocathode for highly efficient solar water splitting. J. Mater. Chem. A **7**, 15593–15598 (2019). https://doi.org/10.1039/c9ta04822g
144. Kobayashi, H., Sato, N., Orita, M., et al.: Development of highly efficient $CuIn_{0.5}Ga_{0.5}Se_2$-based photocathode and application to overall solar driven water splitting. Energy Environ. Sci. **11**, 3003–3009 (2018). https://doi.org/10.1039/c8ee01783b
145. Yang, W., Oh, Y., Kim, J., et al.: Molecular chemistry-controlled hybrid ink-derived efficient Cu_2ZnSnS_4 photocathodes

for photoelectrochemical water splitting. ACS Energy Lett. **1**, 1127–1136 (2016). https://doi.org/10.1021/acsenergylett.6b00453
146. Chen, M.X., Liu, Y., Li, C.C., et al.: Spatial control of cocatalysts and elimination of interfacial defects towards efficient and robust CIGS photocathodes for solar water splitting. Energy Environ. Sci. **11**, 2025–2034 (2018). https://doi.org/10.1039/c7ee03650g
147. Mali, M.G., Yoon, H., Joshi, B.N., et al.: Enhanced photoelectrochemical solar water splitting using a platinum-decorated CIGS/CdS/ZnO photocathode. ACS Appl. Mater. Interfaces **7**, 21619–21625 (2015). https://doi.org/10.1021/acsami.5b07267
148. Kim, B., Park, G.S., Hwang, Y.J., et al.: Cu(In, Ga)$(S, Se)_2$ photocathodes with a grown-in Cu_xS catalyst for solar water splitting. ACS Energy Lett. **4**, 2937–2944 (2019). https://doi.org/10.1021/acsenergylett.9b01816
149. Tay, Y.F., Kaneko, H., Chiam, S.Y., et al.: Solution-processed Cd-substituted CZTS photocathode for efficient solar hydrogen evolution from neutral water. Joule **2**, 537–548 (2018). https://doi.org/10.1016/j.joule.2018.01.012
150. Yokoyama, D., Minegishi, T., Jimbo, K., et al.: H_2 evolution from water on modified Cu_2ZnSnS_4 photoelectrode under solar light. Appl. Phys. Express **3**, 101202 (2010). https://doi.org/10.1143/apex.3.101202
151. Rovelli, L., Tilley, S.D., Sivula, K.: Optimization and stabilization of electrodeposited Cu_2ZnSnS_4 photocathodes for solar water reduction. ACS Appl. Mater. Interfaces **5**, 8018–8024 (2013). https://doi.org/10.1021/am402096r
152. Moriya, M., Minegishi, T., Kumagai, H., et al.: Stable hydrogen evolution from CdS-modified $CuGaSe_2$ photoelectrode under visible-light irradiation. J. Am. Chem. Soc. **135**, 3733–3735 (2013). https://doi.org/10.1021/ja312653y
153. Jiang, F., Gunawan, Harada, T., et al.: Pt/In_2S_3/CdS/Cu_2ZnSnS_4 thin film as an efficient and stable photocathode for water reduction under sunlight radiation. J. Am. Chem. Soc. **137**, 13691–13697 (2015). https://doi.org/10.1021/jacs.5b09015
154. Zhou, Y.H., Shin, D., Ngaboyamahina, E., et al.: Efficient and stable Pt/TiO_2/CdS/$Cu_2BaSn(S, Se)_4$ photocathode for water electrolysis applications. ACS Energy Lett. **3**, 177–183 (2018). https://doi.org/10.1021/acsenergylett.7b01062
155. Huang, D.W., Wang, K., Yu, L., et al.: Over 1% efficient unbiased stable solar water splitting based on a sprayed Cu_2ZnSnS_4 photocathode protected by a HfO_2 photocorrosion-resistant film. ACS Energy Lett. **3**, 1875–1881 (2018). https://doi.org/10.1021/acsenergylett.8b01005
156. Huang, D.W., Wang, K., Li, L.T., et al.: 3.17% Efficient Cu_2ZnSnS_4–$BiVO_4$ integrated tandem cell for standalone overall solar water splitting. Energy Environ. Sci. **14**, 1480–1489 (2021). https://doi.org/10.1039/d0ee03892j
157. Feng, K., Huang, D.W., Li, L.T., et al.: MoS_x-CdS/Cu_2ZnSnS_4-based thin film photocathode for solar hydrogen evolution from water. Appl. Catal. B Environ. **268**, 118438 (2020). https://doi.org/10.1016/j.apcatb.2019.118438
158. Guijarro, N., Prévot, M.S., Sivula, K.: Enhancing the charge separation in nanocrystalline Cu_2ZnSnS_4 photocathodes for photoelectrochemical application: the role of surface modifications. J Phys Chem Lett **5**, 3902–3908 (2014). https://doi.org/10.1021/jz501996s
159. Feng, K., Cai, Z.W., Huang, D.W., et al.: Near-infrared-driven water splitting for hydrogen evolution using a Cu_2ZnSnS_4-based photocathode by the application of upconversion nanoparticles. Sustain. Energy Fuels **4**, 2669–2674 (2020). https://doi.org/10.1039/d0se00152j
160. Jackson, P., Hariskos, D., Wuerz, R., et al.: Properties of Cu(In, Ga)Se_2 solar cells with new record efficiencies up to 21.7%. Phys. Stat. Sol. (RRL) **9**, 28–31 (2015). https://doi.org/10.1002/pssr.201409520
161. Contreras, M.A., Mansfield, L.M., Egaas, B., et al.: Improved energy conversion efficiency in wide bandgap Cu(In, Ga)Se_2 solar cells. 2011 37th IEEE Photovoltaic Specialists Conference. Seattle, WA, USA. IEEE, 026–031 (2011). https://doi.org/10.1109/PVSC.2011.6185837
162. Chae, S.Y., Park, S.J., Han, S.G., et al.: Enhanced photocurrents with ZnS passivated Cu(In, Ga)$(Se, S)_2$ photocathodes synthesized using a nonvacuum process for solar water splitting. J. Am. Chem. Soc. **138**, 15673–15681 (2016). https://doi.org/10.1021/jacs.6b09595
163. Baek, M., Zafar, M., Kim, S., et al.: Enhancing durability and photoelectrochemical performance of the earth abundant Ni-Mo/TiO_2/CdS/ClGS photocathode under various pH conditions. Chemsuschem **11**, 3679–3688 (2018). https://doi.org/10.1002/cssc.201801211
164. Kumagai, H., Minegishi, T., Sato, N., et al.: Efficient solar hydrogen production from neutral electrolytes using surface-modified Cu(In, Ga)Se_2 photocathodes. J. Mater. Chem. A **3**, 8300–8307 (2015). https://doi.org/10.1039/c5ta01058f
165. Gaillard, N., Prasher, D., Kaneshiro, J., et al.: Development of chalcogenide thin film materials for photoelectrochemical hydrogen production. MRS Proc. **1558**, 207 (2013). https://doi.org/10.1557/opl.2013.1084
166. Gaillard, N., Prasher, D., Chong, M., et al.: Wide-bandgap Cu(In, Ga)S_2 photocathodes integrated on transparent conductive F:SnO_2 substrates for chalcopyrite-based water splitting tandem devices. ACS Appl. Energy Mater. **2**, 5515–5524 (2019). https://doi.org/10.1021/acsaem.9b00690
167. Gaillard, N., Deangelis, A.: Photoelectrochemical water splitting using photovoltaic materials. In: Sugiyama M., Fujii K., Nakamura S. (eds.) Solar to Chemical Energy Conversion: Theory and Application. Springer International Publishing, New York (2016)
168. Jacobsson, T.J., Fjällström, V., Sahlberg, M., et al.: A monolithic device for solar water splitting based on series interconnected thin film absorbers reaching over 10% solar-to-hydrogen efficiency. Energy Environ. Sci. **6**, 3676–3683 (2013). https://doi.org/10.1039/c3ee42519c
169. Luo, J.S., Li, Z., Nishiwaki, S., et al.: Targeting ideal dual-absorber tandem water splitting using perovskite photovoltaics and $CuIn_xGa_{1-x}Se_2$ photocathodes. Adv. Energy Mater. **5**, 1501520 (2015). https://doi.org/10.1002/aenm.201501520
170. Koo, B., Nam, S.W., Haight, R., et al.: Tailoring photoelectrochemical performance and stability of Cu(In, Ga)Se_2 photocathode via TiO_2-coupled buffer layers. ACS Appl. Mater. Interfaces **9**, 5279–5287 (2017). https://doi.org/10.1021/acsami.6b15168
171. Koo, B., Byun, S., Nam, S.W., et al.: Reduced graphene oxide as a catalyst binder: greatly enhanced photoelectrochemical stability of Cu(In, Ga)Se_2 photocathode for solar water splitting. Adv. Funct. Mater. **28**, 1705136 (2018). https://doi.org/10.1002/adfm.201705136
172. Wang, M.Q., Chang, Y.S., Tsao, C.W., et al.: Enhanced photoelectrochemical hydrogen generation in neutral electrolyte using non-vacuum processed ClGS photocathodes with an earth-abundant cobalt sulfide catalyst. Chem. Commun. **55**, 2465–2468 (2019). https://doi.org/10.1039/c8cc09426h
173. Kaneko, H., Minegishi, T., Nakabayashi, M., et al.: A novel photocathode material for sunlight-driven overall water splitting: solid solution of ZnSe and Cu(In, Ga)Se_2. Adv. Funct. Mater. **26**, 4570–4577 (2016). https://doi.org/10.1002/adfm.201600615
174. Kageshima, Y., Fujita, T., Takagi, F., et al.: Electrochemical evaluation for multiple functions of Pt-loaded TiO_2 nanoparticles deposited on a photocathode. ChemElectroChem **6**, 4859–4866 (2019). https://doi.org/10.1002/celc.201901453
175. Takagi, F., Kageshima, Y., Teshima, K., et al.: Enhanced photoelectrochemical performance from particulate ZnSe: Cu(In, Ga)Se_2 photocathodes during solar hydrogen production via particle

size control. Sustain. Energy Fuels **5**, 412–423 (2021). https://doi.org/10.1039/d0se00998a
176. Septina, W., Gunawan, Ikeda, S., et al.: Photosplitting of water from wide-gap Cu(In, Ga)S_2 thin films modified with a CdS layer and Pt nanoparticles for a high-onset-potential photocathode. J. Phys. Chem. C **119**, 8576–8583 (2015). https://doi.org/10.1021/acs.jpcc.5b02068
177. Lin, J., Zhang, Z., Chai, J., et al.: Highly efficient InGaN nanorods photoelectrode by constructing Z-scheme charge transfer system for unbiased water splitting. Small **17**, e2006666 (2021). https://doi.org/10.1002/smll.202006666
178. Chu, S., Vanka, S., Wang, Y.C., et al.: Solar water oxidation by an InGaN nanowire photoanode with a bandgap of 1.7 eV. ACS Energy Lett. **3**, 307–314 (2018). https://doi.org/10.1021/acsenergylett.7b01138
179. Zheng, Y., Wang, W., Li, Y., et al.: Self-integrated hybrid ultraviolet photodetectors based on the vertically aligned InGaN nanorod array assembly on graphene. ACS Appl. Mater. Interfaces **11**, 13589–13597 (2019). https://doi.org/10.1021/acsami.9b00940
180. Lin, J., Yu, Y.F., Zhang, Z.J., et al.: A novel approach for achieving high-efficiency photoelectrochemical water oxidation in InGaN nanorods grown on Si system: MXene nanosheets as multifunctional interfacial modifier. Adv. Funct. Mater. **30**, 1910479 (2020). https://doi.org/10.1002/adfm.201910479
181. Vanka, S., Zhou, B.W., Awni, R.A., et al.: InGaN/Si double-junction photocathode for unassisted solar water splitting. ACS Energy Lett. **5**, 3741–3751 (2020). https://doi.org/10.1021/acsenergylett.0c01583
182. Yang, F., Kuznietsov, V., Lublow, M., et al.: Solar hydrogen evolution using metal-free photocatalytic polymeric carbon nitride/$CuInS_2$ composites as photocathodes. J. Mater. Chem. A **1**, 6407–6415 (2013). https://doi.org/10.1039/c3ta10360a
183. Kumagai, H., Minegishi, T., Moriya, Y., et al.: Photoelectrochemical hydrogen evolution from water using copper gallium selenide electrodes prepared by a particle transfer method. J. Phys. Chem. C **118**, 16386–16392 (2014). https://doi.org/10.1021/jp409921f
184. Hellstern, T.R., Palm, D.W., Carter, J., et al.: Molybdenum disulfide catalytic coatings via atomic layer deposition for solar hydrogen production from copper gallium diselenide photocathodes. ACS Appl. Energy Mater. **2**, 1060–1066 (2019). https://doi.org/10.1021/acsaem.8b01562
185. Muzzillo, C.P., Klein, W.E., Li, Z., et al.: Low-cost, efficient, and durable H_2 production by photoelectrochemical water splitting with $CuGa_3Se_5$ photocathodes. ACS Appl. Mater. Interfaces **10**, 19573–19579 (2018). https://doi.org/10.1021/acsami.8b01447
186. Chae, S.Y., Kim, S., Joo, O.S.: Design of an amorphous TaO_x multifunctional interfacial layer on photocathodes for photoelectrochemical H_2 evolution. J. Mater. Chem. A **7**, 2041–2047 (2019). https://doi.org/10.1039/c8ta10738f
187. Frick, J.J., Cava, R.J., Bocarsly, A.B.: Chalcopyrite $CuIn(S_{1-x}Se_x)_2$ for photoelectrocatalytic H_2 evolution: unraveling the energetics and complex kinetics of photogenerated charge transfer in the semiconductor bulk. Chem. Mater. **30**, 4422–4431 (2018). https://doi.org/10.1021/acs.chemmater.8b01827
188. Gärtner, W.W.: Depletion-layer photoeffects in semiconductors. Phys. Rev. **116**, 84–87 (1959). https://doi.org/10.1103/physrev.116.84
189. Mora-Seró, I., Dittrich, T., Garcia-Belmonte, G., et al.: Determination of spatial charge separation of diffusing electrons by transient photovoltage measurements. J. Appl. Phys. **100**, 103705 (2006). https://doi.org/10.1063/1.2361158
190. Liu, Z., Zhou, M.: Co-modification with cost-effective nickel oxides and nickel sulfides on $CuInS_2$ nanosheets photocathode for enhanced photoelectrochemical performance. ACS Sustain. Chem. Eng. **8**, 512–519 (2020). https://doi.org/10.1021/acssuschemeng.9b05936
191. Guijarro, N., Prévot, M.S., Yu, X.Y., et al.: A bottom-up approach toward all-solution-processed high-efficiency Cu(In, Ga)S_2 photocathodes for solar water splitting. Adv. Energy Mater. **6**, 1501949 (2016). https://doi.org/10.1002/aenm.201501949
192. Gunawan, Septina, W., Harada, T., et al.: Investigation of the electric structures of heterointerfaces in Pt- and In_2S_3-modified $CuInS_2$ photocathodes used for sunlight-induced hydrogen evolution. ACS Appl. Mater. Interfaces **7**, 16086–16092 (2015). https://doi.org/10.1021/acsami.5b04634
193. Li, M., Chen, L., Su, Y.J., et al.: Hexagonally ordered microbowl arrays decorated with ultrathin $CuInS_2$ nanosheets for enhanced photoelectrochemical performance. J. Energy Chem. **51**, 134–142 (2020). https://doi.org/10.1016/j.jechem.2020.03.070
194. Zhang, L., Minegishi, T., Nakabayashi, M., et al.: Durable hydrogen evolution from water driven by sunlight using (Ag, Cu)$GaSe_2$ photocathodes modified with CdS and $CuGa_3Se_5$. Chem. Sci. **6**, 894–901 (2015). https://doi.org/10.1039/c4sc02346c
195. Na, Y., Hu, B., Yang, Q.L., et al.: CdS quantum dot sensitized p-type NiO as photocathode with integrated cobaloxime in photoelectrochemical cell for water splitting. Chin. Chem. Lett. **26**, 141–144 (2015). https://doi.org/10.1016/j.cclet.2014.09.011
196. Liu, S.S., Luo, Z.B., Li, L.L., et al.: Multifunctional TiO_2 overlayer for p-Si/n-CdS heterojunction photocathode with improved efficiency and stability. Nano Energy **53**, 125–129 (2018). https://doi.org/10.1016/j.nanoen.2018.08.024
197. Yan, J., Li, X., Yang, S.Y., et al.: Design and preparation of CdS/H-3D-TiO_2/Pt-wire photocatalysis system with enhanced visible-light driven H_2 evolution. Int. J. Hydrog. Energy **42**, 928–937 (2017). https://doi.org/10.1016/j.ijhydene.2016.08.188
198. Wei, L., Zhang, J., Ruan, M.N.: Combined CdS/In_2S_3 heterostructures with cocatalyst for boosting carriers separation and photoelectrochemical water splitting. Appl. Surf. Sci. **541**, 148431 (2021). https://doi.org/10.1016/j.apsusc.2020.148431
199. Meng, L.X., He, J.L., Tian, W., et al.: Ni/Fe codoped In_2S_3 nanosheet arrays boost photo-electrochemical performance of planar Si photocathodes. Adv. Energy Mater. **9**, 1902135 (2019). https://doi.org/10.1002/aenm.201902135
200. Bai, Z.M., Zhang, Y.H.: A Cu_2O/Cu_2S-ZnO/CdS tandem photoelectrochemical cell for self-driven solar water splitting. J. Alloys Compd. **698**, 133–140 (2017). https://doi.org/10.1016/j.jallcom.2016.12.261
201. Ye, Z., Hu, Z.F., Yang, L.X., et al.: Stable p-type Cu: $CdS_{1-x}Se_x$/Pt thin-film photocathodes with fully tunable bandgap for scavenger-free photoelectrochemical water splitting. Sol. RRL **4**, 1900567 (2020). https://doi.org/10.1002/solr.201900567
202. Sheng, W.H., Song, Y., Dou, M.L., et al.: Constructing 1D hierarchical heterostructures of MoS_2/In_2S_3 nanosheets on CdS nanorod arrays for enhanced photoelectrocatalytic H_2 evolution. Appl. Surf. Sci. **436**, 613–623 (2018). https://doi.org/10.1016/j.apsusc.2017.11.281
203. Cheng, W., Singh, N., Elliott, W., et al.: Earth-abundant tin sulfide-based photocathodes for solar hydrogen production. Adv. Sci. **5**, 1700362 (2018). https://doi.org/10.1002/advs.201700362
204. Patel, M., Kumar, M., Kim, J., et al.: Photocurrent enhancement by a rapid thermal treatment of nanodisk-shaped SnS photocathodes. J. Phys. Chem. Lett. **8**, 6099–6105 (2017). https://doi.org/10.1021/acs.jpclett.7b02998
205. Li, X.T., Liu, B., Chen, Y., et al.: Decoration of Cu_2O photocathode with protective TiO_2 and active WS_2 layers for enhanced photoelectrochemical hydrogen evolution. Nanotechnology **29**, 505603 (2018). https://doi.org/10.1088/1361-6528/aae569
206. Zhao, H., Dai, Z.Y., Xu, X.Y., et al.: Integrating semiconducting catalyst of ReS_2 nanosheets into p-silicon photocathode for

enhanced solar water reduction. ACS Appl. Mater. Interfaces **10**, 23074–23080 (2018). https://doi.org/10.1021/acsami.8b04740
207. Ran, J.R., Zhang, H.P., Qu, J.T., et al.: Atomic-level insights into the edge active ReS_2 ultrathin nanosheets for high-efficiency light-to-hydrogen conversion. ACS Mater. Lett. **2**, 1484–1494 (2020). https://doi.org/10.1021/acsmaterialslett.0c00205
208. Basu, M., Zhang, Z.W., Chen, C.J., et al.: Heterostructure of Si and $CoSe_2$: a promising photocathode based on a non-noble metal catalyst for photoelectrochemical hydrogen evolution. Angew. Chem. Int. Ed. **54**, 6211–6216 (2015). https://doi.org/10.1002/anie.201502573
209. Wang, K., Huang, D.W., Li, L.T., et al.: Three-dimensional GeSe microstructured air brick photocathode for advanced solar water splitting. Sol. RRL **4**, 1900559 (2020). https://doi.org/10.1002/solr.201900559
210. Wang, K., Huang, D.W., Yu, L., et al.: Promising GeSe nanosheet-based thin-film photocathode for efficient and stable overall solar water splitting. ACS Catal. **9**, 3090–3097 (2019). https://doi.org/10.1021/acscatal.9b00035
211. Wu, F.L., Tian, W., Cao, F.R., et al.: Loading amorphous $NiMoO_{4-x}S_x$ nanosheet cocatalyst to improve performance of p-silicon wafer photocathode. ACS Appl. Energy Mater. **1**, 1286–1293 (2018). https://doi.org/10.1021/acsaem.8b00017
212. Yang, W., Lee, S., Kwon, H.C., et al.: Time-resolved observations of photo-generated charge-carrier dynamics in Sb_2Se_3 photocathodes for photoelectrochemical water splitting. ACS Nano **12**, 11088–11097 (2018). https://doi.org/10.1021/acsnano.8b05446
213. Chen, C., Zhao, Y., Lu, S.C., et al.: Accelerated optimization of TiO_2/Sb_2Se_3 thin film solar cells by high-throughput combinatorial approach. Adv. Energy Mater. **7**, 1700866 (2017). https://doi.org/10.1002/aenm.201700866
214. Zhou, Y., Wang, L., Chen, S., et al.: Thin-film Sb_2Se_3 photovoltaics with oriented one-dimensional ribbons and benign grain boundaries. Nat. Photonics **9**, 409–415 (2015). https://doi.org/10.1038/nphoton.2015.78
215. Wang, L., Li, D.B., Li, K.H., et al.: Stable 6%-efficient Sb_2Se_3 solar cells with a ZnO buffer layer. Nat. Energy **2**, 17046 (2017). https://doi.org/10.1038/nenergy.2017.46
216. Zhang, L., Li, Y.B., Li, C.L., et al.: Scalable low-band-gap Sb_2Se_3 thin-film photocathodes for efficient visible–near-infrared solar hydrogen evolution. ACS Nano **11**, 12753–12763 (2017). https://doi.org/10.1021/acsnano.7b07512
217. Prabhakar, R.R., Septina, W., Siol, S., et al.: Photocorrosion-resistant Sb_2Se_3 photocathodes with earth abundant MoS_x hydrogen evolution catalyst. J. Mater. Chem. A **5**, 23139–23145 (2017). https://doi.org/10.1039/C7TA08993G
218. Park, J., Yang, W., Oh, Y., et al.: Efficient solar-to-hydrogen conversion from neutral electrolytes using morphology-controlled Sb_2Se_3 light absorbers. ACS Energy Lett. **4**, 517–526 (2019). https://doi.org/10.1021/acsenergylett.8b02323
219. Yang, W., Kim, J.H., Hutter, O.S., et al.: Benchmark performance of low-cost Sb_2Se_3 photocathodes for unassisted solar overall water splitting. Nat. Commun. **11**, 861 (2020). https://doi.org/10.1038/s41467-020-14704-3
220. Tan, J., Yang, W., Lee, H., et al.: Surface restoration of polycrystalline Sb_2Se_3 thin films by conjugated molecules enabling high-performance photocathodes for photoelectrochemical water splitting. Appl. Catal. B Environ. **286**, 119890 (2021). https://doi.org/10.1016/j.apcatb.2021.119890
221. Liu, C., Liu, T., Li, Y.Z., et al.: A dendritic Sb_2Se_3/In_2S_3 heterojunction nanorod array photocathode decorated with a MoS_x catalyst for efficient solar hydrogen evolution. J. Mater. Chem. A **8**, 23385–23394 (2020). https://doi.org/10.1039/d0ta08874a
222. Gu, J., Aguiar, J.A., Ferrere, S., et al.: A graded catalytic–protective layer for an efficient and stable water-splitting photocathode. Nat. Energy **2**, 16192 (2017). https://doi.org/10.1038/nenergy.2016.192
223. Pinaud, B.A., Benck, J.D., Seitz, L.C., et al.: Technical and economic feasibility of centralized facilities for solar hydrogen production via photocatalysis and photoelectrochemistry. Energy Environ. Sci. **6**, 1983–2002 (2013). https://doi.org/10.1039/c3ee40831k
224. Döscher, H., Geisz, J.F., Deutsch, T.G., et al.: Sunlight absorption in water-efficiency and design implications for photoelectrochemical devices. Energy Environ. Sci. **7**, 2951–2956 (2014). https://doi.org/10.1039/c4ee01753f
225. Khaselev, O., Turner, J.A.: A monolithic photovoltaic-photoelectrochemical device for hydrogen production via water splitting. Science **280**, 425–427 (1998). https://doi.org/10.1126/science.280.5362.425
226. Lim, H., Young, J.L., Geisz, J.F., et al.: High performance III-V photoelectrodes for solar water splitting via synergistically tailored structure and stoichiometry. Nat. Commun. **10**, 3388 (2019). https://doi.org/10.1038/s41467-019-11351-1
227. Britto, R.J., Benck, J.D., Young, J.L., et al.: Molybdenum disulfide as a protection layer and catalyst for gallium indium phosphide solar water splitting photocathodes. J. Phys. Chem. Lett. **7**, 2044–2049 (2016). https://doi.org/10.1021/acs.jpclett.6b00563
228. Tomkiewicz, M., Woodall, J.M.: Photoassisted electrolysis of water by visible irradiation of a p-type gallium phosphide electrode. Science **196**, 990–991 (1977). https://doi.org/10.1126/science.196.4293.990
229. Assali, S., Zardo, I., Plissard, S., et al.: Direct band gap wurtzite gallium phosphide nanowires. Nano Lett. **13**, 1559–1563 (2013). https://doi.org/10.1021/nl304723c
230. Malizia, M., Seger, B., Chorkendorff, I., et al.: Formation of a p–n heterojunction on GaP photocathodes for H_2 production providing an open-circuit voltage of 710 mV. J. Mater. Chem. A **2**, 6847–6853 (2014). https://doi.org/10.1039/c4ta00752b
231. Liu, C., Sun, J.W., Tang, J.Y., et al.: Zn-doped p-type gallium phosphide nanowire photocathodes from a surfactant-free solution synthesis. Nano Lett. **12**, 5407–5411 (2012). https://doi.org/10.1021/nl3028729
232. Standing, A., Assali, S., Gao, L., et al.: Efficient water reduction with gallium phosphide nanowires. Nat. Commun. **6**, 7824 (2015). https://doi.org/10.1038/ncomms8824
233. Lee, M.H., Takei, K., Zhang, J.J., et al.: p-Type InP nanopillar photocathodes for efficient solar-driven hydrogen production. Angew. Chem. Int. Ed. **51**, 10760–10764 (2012). https://doi.org/10.1002/anie.201203174
234. Hellstern, T.R., Benck, J.D., Kibsgaard, J., et al.: Engineering cobalt phosphide (CoP) thin film catalysts for enhanced hydrogen evolution activity on silicon photocathodes. Adv. Energy Mater. **6**, 1501758 (2016). https://doi.org/10.1002/aenm.201501758
235. Zhou, B., Kong, X., Vanka, S., et al.: Gallium nitride nanowire as a linker of molybdenum sulfides and silicon for photoelectrocatalytic water splitting. Nat. Commun. **9**, 3856 (2018). https://doi.org/10.1038/s41467-018-06140-1
236. Cabán-Acevedo, M., Stone, M.L., Schmidt, J.R., et al.: Efficient hydrogen evolution catalysis using ternary pyrite-type cobalt phosphosulphide. Nat. Mater. **14**, 1245–1251 (2015). https://doi.org/10.1038/nmat4410
237. Tijare, S.N., Joshi, M.V., Padole, P.S., et al.: Photocatalytic hydrogen generation through water splitting on nano-crystalline $LaFeO_3$ perovskite. Int. J. Hydrog. Energy **37**, 10451–10456 (2012). https://doi.org/10.1016/j.ijhydene.2012.01.120
238. Scafetta, M.D., Cordi, A.M., Rondinelli, J.M., et al.: Band structure and optical transitions in $LaFeO_3$: theory and experiment. J. Phys. Condens. Matter **26**, 505502 (2014). https://doi.org/10.1088/0953-8984/26/50/505502

239. Prévot, M.S., Guijarro, N., Sivula, K.: Enhancing the performance of a robust sol-gel-processed p-type delafossite $CuFeO_2$ photocathode for solar water reduction. Chemsuschem **8**, 1359–1367 (2015). https://doi.org/10.1002/cssc.201403146
240. Read, C.G., Park, Y., Choi, K.S.: Electrochemical synthesis of p-type $CuFeO_2$ electrodes for use in a photoelectrochemical cell. J. Phys. Chem. Lett. **3**, 1872–1876 (2012). https://doi.org/10.1021/jz300709t
241. Li, Y., Wang, T., Gao, B., et al.: Efficient photocathode performance of lithium ion doped $LaFeO_3$ nanorod arrays in hydrogen evolution. New J. Chem. **45**, 3463–3468 (2021). https://doi.org/10.1039/d0nj05788f
242. Wheeler, G.P., Choi, K.S.: Photoelectrochemical properties and stability of nanoporous p-type $LaFeO_3$ photoelectrodes prepared by electrodeposition. ACS Energy Lett. **2**, 2378–2382 (2017). https://doi.org/10.1021/acsenergylett.7b00642
243. Parida, K.M., Reddy, K.H., Martha, S., et al.: Fabrication of nanocrystalline $LaFeO_3$: an efficient sol-gel auto-combustion assisted visible light responsive photocatalyst for water decomposition. Int. J. Hydrog. Energy **35**, 12161–12168 (2010). https://doi.org/10.1016/j.ijhydene.2010.08.029
244. Gupta, M.V.N.S., Baig, H., Reddy, K.S., et al.: Photoelectrochemical water splitting using a concentrated solar flux-assisted $LaFeO_3$ photocathode. ACS Appl. Energy Mater. **3**, 9002–9009 (2020). https://doi.org/10.1021/acsaem.0c01428
245. Pawar, G.S., Elikkottil, A., Seetha, S., et al.: Enhanced photoactivity and hydrogen generation of $LaFeO_3$ photocathode by plasmonic silver nanoparticle incorporation. ACS Appl. Energy Mater. **1**, 3449–3456 (2018). https://doi.org/10.1021/acsaem.8b00628
246. Son, M.K., Seo, H., Watanabe, M., et al.: Characteristics of crystalline sputtered $LaFeO_3$ thin films as photoelectrochemical water splitting photocathodes. Nanoscale **12**, 9653–9660 (2020). https://doi.org/10.1039/d0nr01762k
247. Wang, P.P., He, Y.F., Mi, Y., et al.: Enhanced photoelectrochemical performance of $LaFeO_3$ photocathode with Au buffer layer. RSC Adv. **9**, 26780–26786 (2019). https://doi.org/10.1039/c9ra05521e
248. Yan, X.Y., Pu, R.H., Xie, R.J., et al.: Design and fabrication of $Bi_2O_3/BiFeO_3$ heterojunction film with improved photoelectrochemical performance. Appl. Surf. Sci. **552**, 149442 (2021). https://doi.org/10.1016/j.apsusc.2021.149442
249. Shen, H.Y., Zhou, X.X., Dong, W., et al.: Dual role of TiO_2 buffer layer in Pt catalyzed $BiFeO_3$ photocathodes: efficiency enhancement and surface protection. Appl. Phys. Lett. **111**, 123901 (2017). https://doi.org/10.1063/1.4999969
250. Cheng, X.R., Shen, H.Y., Dong, W., et al.: Nano-Au and ferroelectric polarization mediated Si/ITO/$BiFeO_3$ tandem photocathode for efficient H_2 production. Adv. Mater. Interfaces **3**, 1600485 (2016). https://doi.org/10.1002/admi.201600485
251. Cheng, X., Gu, S., Centeno, A., et al.: Plasmonic enhanced Cu_2O-Au-BFO photocathodes for solar hydrogen production. Sci. Rep. **9**, 5140 (2019). https://doi.org/10.1038/s41598-019-41613-3
252. Zhao, W., Jin, Y., Gao, C.H., et al.: A simple method for fabricating p–n junction photocatalyst $CuFe_2O_4/Bi_4Ti_3O_{12}$ and its photocatalytic activity. Mater. Chem. Phys. **143**, 952–962 (2014). https://doi.org/10.1016/j.matchemphys.2013.10.026
253. Helaïli, N., Bessekhouad, Y., Bachari, K., et al.: Synthesis and physical properties of the $CuFe_{2-x}Mn_xO_4$ ($0 \leqslant x \leqslant 2$) solid solution. Mater. Chem. Phys. **148**, 734–743 (2014). https://doi.org/10.1016/j.matchemphys.2014.08.042
254. Dillert, R., Taffa, D.H., Wark, M., et al.: Research update: photoelectrochemical water splitting and photocatalytic hydrogen production using ferrites (MFe_2O_4) under visible light irradiation. APL Mater. **3**, 104001 (2015). https://doi.org/10.1063/1.4931763
255. Park, S., Baek, J.H., Zhang, L., et al.: Rapid flame-annealed $CuFe_2O_4$ as efficient photocathode for photoelectrochemical hydrogen production. ACS Sustainable Chem. Eng. **7**, 5867–5874 (2019). https://doi.org/10.1021/acssuschemeng.8b05824
256. Jang, Y.J., Park, Y.B., Kim, H.E., et al.: Oxygen-intercalated $CuFeO_2$ photocathode fabricated by hybrid microwave annealing for efficient solar hydrogen production. Chem. Mater. **28**, 6054–6061 (2016). https://doi.org/10.1021/acs.chemmater.6b00460
257. Oh, Y., Yang, W., Tan, J., et al.: Boosting visible light harvesting in p-type ternary oxides for solar-to-hydrogen conversion using inverse opal structure. Adv. Funct. Mater. **29**, 1900194 (2019). https://doi.org/10.1002/adfm.201900194
258. Cots, A., Bonete, P., Gómez, R.: Improving the stability and efficiency of CuO photocathodes for solar hydrogen production through modification with iron. ACS Appl. Mater. Interfaces **10**, 26348–26356 (2018). https://doi.org/10.1021/acsami.8b09892
259. Tapia, C., Bellet-Amalric, E., Aldakov, D., et al.: Achieving visible light-driven hydrogen evolution at positive bias with a hybrid copper–iron oxide|TiO_2-cobaloxime photocathode. Green Chem. **22**, 3141–3149 (2020). https://doi.org/10.1039/d0gc00979b
260. Atacan, K., Güy, N., Boutra, B., et al.: Enhancement of photoelectrochemical hydrogen production by using a novel ternary Ag_2CrO_4/GO/$MnFe_2O_4$ photocatalyst. Int. J. Hydrog. Energy **45**, 17453–17467 (2020). https://doi.org/10.1016/j.ijhydene.2020.04.268
261. Chen, Y.J., Jiang, H.Y., Li, L.G., et al.: Hierarchical NiS decorated CuO@$ZnFe_2O_4$ nanoarrays as advanced photocathodes for hydrogen evolution reaction. Int. J. Hydrog. Energy **45**, 6174–6183 (2020). https://doi.org/10.1016/j.ijhydene.2019.12.170
262. Ida, S., Yamada, K., Matsunaga, T., et al.: Preparation of p-type $CaFe_2O_4$ photocathodes for producing hydrogen from water. J. Am. Chem. Soc. **132**, 17343–17345 (2010). https://doi.org/10.1021/ja106930f
263. Ida, S., Kearney, K., Futagami, T., et al.: Photoelectrochemical H_2 evolution using TiO_2-coated $CaFe_2O_4$ without an external applied bias under visible light irradiation at 470 nm based on device modeling. Sustain. Energy Fuels **1**, 280–287 (2017). https://doi.org/10.1039/c7se00084g
264. Sun, H.J., Öner, I.H., Wang, T., et al.: Molecular engineering of conjugated acetylenic polymers for efficient cocatalyst-free photoelectrochemical water reduction. Angew. Chem. Int. Ed. **58**, 10368–10374 (2019). https://doi.org/10.1002/anie.201904978
265. Liu, Y., Li, C., Ren, Z., et al.: All-organic thermally activated delayed fluorescence materials for organic light-emitting diodes. Nat. Rev. Mater. **3**, 18020 (2018). https://doi.org/10.1038/natrevmats.2018.20
266. Gather, M.C., Köhnen, A., Meerholz, K.: White organic light-emitting diodes. Adv. Mater. **23**, 233–248 (2011). https://doi.org/10.1002/adma.201002636
267. Torsi, L., Magliulo, M., Manoli, K., et al.: Organic field-effect transistor sensors: a tutorial review. Chem. Soc. Rev. **42**, 8612–8628 (2013). https://doi.org/10.1039/c3cs60127g
268. Günes, S., Neugebauer, H., Sariciftci, N.S.: Conjugated polymer-based organic solar cells. Chem. Rev. **107**, 1324–1338 (2007). https://doi.org/10.1021/cr050149z
269. Cheng, Y.J., Yang, S.H., Hsu, C.S.: Synthesis of conjugated polymers for organic solar cell applications. Chem. Rev. **109**, 5868–5923 (2009). https://doi.org/10.1021/cr900182s
270. Ming, J.T., Liu, A., Zhao, J.W., et al.: Hot π-electron tunneling of metal–insulator–COF nanostructures for efficient hydrogen production. Angew. Chem. Int. Ed. **58**, 18290–18294 (2019). https://doi.org/10.1002/anie.201912344

271. Huang, T., Lin, X., Liu, Y., et al.: Molecular engineering of fully conjugated sp^2 carbon-linked polymers for high-efficiency photocatalytic hydrogen evolution. Chemsuschem **13**, 672–676 (2020). https://doi.org/10.1002/cssc.201903334
272. Han, S.T., Huang, T., Pan, Y., et al.: Tunable linear donor–π–acceptor conjugated polymers with a vinylene linkage for visible-light driven hydrogen evolution. Catal. Sci. Technol. **11**, 4021–4025 (2021). https://doi.org/10.1039/d1cy00535a
273. Lin, H., Ma, Z.Y., Zhao, J.W., et al.: Electric-field-mediated electron tunneling of supramolecular naphthalimide nanostructures for biomimetic H_2 production. Angew. Chem. Int. Ed. **60**, 1235–1243 (2021). https://doi.org/10.1002/anie.202009267
274. Sun, H.J., Neumann, C., Zhang, T., et al.: Poly(1, 4-diethynylbenzene) gradient homojunction with enhanced charge carrier separation for photoelectrochemical water reduction. Adv. Mater. **31**, 1900961 (2019). https://doi.org/10.1002/adma.201900961
275. Sick, T., Hufnagel, A.G., Kampmann, J., et al.: Oriented films of conjugated 2D covalent organic frameworks as photocathodes for water splitting. J. Am. Chem. Soc. **140**, 2085–2092 (2018). https://doi.org/10.1021/jacs.7b06081
276. Murakami, T., Ikezoi, K., Nagai, K., et al.: A water-splitting system with a cobalt (II, III) oxide co-catalyst-loaded bismuth vanadate photoanode along with an organo-photocathode. ChemElectroChem **7**, 5029–5035 (2020). https://doi.org/10.1002/celc.202001271
277. Li, H., Wen, P., Hoxie, A., et al.: Interface engineering of colloidal CdSe quantum dot thin films as acid-stable photocathodes for solar-driven hydrogen evolution. ACS Appl. Mater. Interfaces **10**, 17129–17139 (2018). https://doi.org/10.1021/acsami.7b19229
278. Morozan, A., Bourgeteau, T., Tondelier, D., et al.: Noble metal-free hydrogen-evolving photocathodes based on small molecule organic semiconductors. Nanotechnology **27**, 355401 (2016). https://doi.org/10.1088/0957-4484/27/35/355401
279. Shi, W., Yu, W., Li, D., et al.: PTB7:PC_{61}BM bulk heterojunction-based photocathodes for efficient hydrogen production in aqueous solution. Chem. Mater. **31**, 1928–1935 (2019). https://doi.org/10.1021/acs.chemmater.8b04629
280. Xu, S.Q., Sun, H.J., Addicoat, M., et al.: Thiophene-bridged donor–acceptor sp^2-carbon-linked 2D conjugated polymers as photocathodes for water reduction. Adv. Mater. **33**, 2006274 (2021). https://doi.org/10.1002/adma.202006274
281. Oka, K., Nishide, H., Winther-Jensen, B.: Completely solar-driven photoelectrochemical water splitting using a neat polythiophene film. Cell Rep. Phys. Sci. **2**, 100306 (2021). https://doi.org/10.1016/j.xcrp.2020.100306
282. Xu, N., Li, F., Gao, L.L., et al.: Polythiophene coated $CuBi_2O_4$ networks: a porous inorganic-organic hybrid heterostructure for enhanced photoelectrochemical hydrogen evolution. Int. J. Hydrog. Energy **43**, 2064–2072 (2018). https://doi.org/10.1016/j.ijhydene.2017.12.036
283. Zhang, Y., Lv, H.F., Zhang, Z., et al.: Stable unbiased photoelectrochemical overall water splitting exceeding 3% efficiency via covalent triazine framework/metal oxide hybrid photoelectrodes. Adv. Mater. **33**, 2008264 (2021). https://doi.org/10.1002/adma.202008264
284. Najafi, L., Romano, V., Oropesa-Nuñez, R., et al.: Hybrid organic/inorganic photocathodes based on WS_2 flakes as hole transporting layer material. Small Struct. **2**, 2000098 (2021). https://doi.org/10.1002/sstr.202000098
285. Steier, L., Bellani, S., Rojas, H.C., et al.: Stabilizing organic photocathodes by low-temperature atomic layer deposition of TiO_2. Sustain. Energy Fuels **1**, 1915–1920 (2017). https://doi.org/10.1039/c7se00421d
286. Fumagalli, F., Bellani, S., Schreier, M., et al.: Hybrid organic–inorganic H_2-evolving photocathodes: understanding the route towards high performance organic photoelectrochemical water splitting. J. Mater. Chem. A **4**, 2178–2187 (2016). https://doi.org/10.1039/c5ta09330a
287. Bellani, S., Najafi, L., Capasso, A., et al.: Few-layer MoS_2 flakes as a hole-selective layer for solution-processed hybrid organic hydrogen-evolving photocathodes. J. Mater. Chem. A **5**, 4384–4396 (2017). https://doi.org/10.1039/c6ta10572f
288. Mezzetti, A., Fumagalli, F., Alfano, A., et al.: Stable hybrid organic/inorganic photocathodes for hydrogen evolution with amorphous WO_3 hole selective contacts. Faraday Discuss. **198**, 433–448 (2017). https://doi.org/10.1039/c6fd00216a
289. Bellani, S., Najafi, L., Martín-García, B., et al.: Graphene-based hole-selective layers for high-efficiency, solution-processed, large-area, flexible, hydrogen-evolving organic photocathodes. J. Phys. Chem. C **121**, 21887–21903 (2017). https://doi.org/10.1021/acs.jpcc.7b05904
290. Hosseini H, S.M., Siavash Moakhar, R., Soleimani, F., et al.: One-pot microwave synthesis of hierarchical C-doped CuO dandelions/g-C_3N_4 nanocomposite with enhanced photostability for photoelectrochemical water splitting. Appl. Surf. Sci. **530**, 147271 (2020). https://doi.org/10.1016/j.apsusc.2020.147271
291. Basu, M., Zhang, Z.W., Chen, C.J., et al.: $CoSe_2$ embedded in C_3N_4: an efficient photocathode for photoelectrochemical water splitting. ACS Appl. Mater. Interfaces **8**, 26690–26696 (2016). https://doi.org/10.1021/acsami.6b06520
292. Gopalakrishnan, S., Bhalerao, G.M., Jeganathan, K.: G-C_3N_4 nanosheets functionalized silicon nanowires hybrid photocathode for efficient visible light induced photoelectrochemical water reduction. J. Power Sources **413**, 293–301 (2019). https://doi.org/10.1016/j.jpowsour.2018.12.034
293. O'Regan, B., Grätzel, M.: A low-cost, high-efficiency solar cell based on dye-sensitized colloidal TiO_2 films. Nature **353**, 737–740 (1991). https://doi.org/10.1038/353737a0
294. Song, W.J., Chen, Z.F., Glasson, C.R.K., et al.: Interfacial dynamics and solar fuel formation in dye-sensitized photoelectrosynthesis cells. ChemPhysChem **13**, 2882–2890 (2012). https://doi.org/10.1002/cphc.201200100
295. Li, L., Duan, L., Xu, Y., et al.: A photoelectrochemical device for visible light driven water splitting by a molecular ruthenium catalyst assembled on dye-sensitized nanostructured TiO_2. Chem. Commun. **46**, 7307–7309 (2010). https://doi.org/10.1039/c0cc01828g
296. Gao, Y., Ding, X., Liu, J.H., et al.: Visible light driven water splitting in a molecular device with unprecedentedly high photocurrent density. J. Am. Chem. Soc. **135**, 4219–4222 (2013). https://doi.org/10.1021/ja400402d
297. Gao, Y., Zhang, L.L., Ding, X., et al.: Artificial photosynthesis–functional devices for light driven water splitting with photoactive anodes based on molecular catalysts. Phys. Chem. Chem. Phys. **16**, 12008–12013 (2014). https://doi.org/10.1039/c3cp55204g
298. Li, F.S., Fan, K., Xu, B., et al.: Organic dye-sensitized tandem photoelectrochemical cell for light driven total water splitting. J. Am. Chem. Soc. **137**, 9153–9159 (2015). https://doi.org/10.1021/jacs.5b04856
299. Windle, C.D., Kumagai, H., Higashi, M., et al.: Earth-abundant molecular Z-scheme photoelectrochemical cell for overall water-splitting. J. Am. Chem. Soc. **141**, 9593–9602 (2019). https://doi.org/10.1021/jacs.9b02521
300. Kaeffer, N., Windle, C.D., Brisse, R., et al.: Insights into the mechanism and aging of a noble-metal free H_2-evolving dye-sensitized photocathode. Chem. Sci. **9**, 6721–6738 (2018). https://doi.org/10.1039/c8sc00899j
301. Ji, Z., He, M., Huang, Z., et al.: Photostable p-type dye-sensitized photoelectrochemical cells for water reduction. J. Am. Chem.

Soc. **135**, 11696–11699 (2013). https://doi.org/10.1021/ja404525e
302. Lattach, Y., Fortage, J., Deronzier, A., et al.: Polypyrrole-Ru(2,2'-bipyridine)$_3^{2+}$/MoS$_x$Structured composite film as a photocathode for the hydrogen evolution reaction. ACS Appl. Mater. Interfaces **7**, 4476–4480 (2015). https://doi.org/10.1021/acsami.5b00401
303. Charisiadis, A., Giannoudis, E., Pournara, Z., et al.: Synthesis and characterization of a covalent porphyrin-cobalt diimine-dioxime dyad for photoelectrochemical H_2 evolution. Eur. J. Inorg. Chem. **2021**, 1122–1129 (2021). https://doi.org/10.1002/ejic.202001111
304. Lyu, S.L., Massin, J., Pavone, M., et al.: H_2-evolving dye-sensitized photocathode based on a ruthenium–diacetylide/cobaloxime supramolecular assembly. ACS Appl. Energy Mater. **2**, 4971–4980 (2019). https://doi.org/10.1021/acsaem.9b00652
305. Ladomenou, K., Nikolaou, V., Charalambidis, G., et al.: "Click"-reaction: an alternative tool for new architectures of porphyrin based derivatives. Coord. Chem. Rev. **306**, 1–42 (2016). https://doi.org/10.1016/j.ccr.2015.06.002
306. Smith, W.A., Sharp, I.D., Strandwitz, N.C., et al.: Interfacial band-edge energetics for solar fuels production. Energy Environ. Sci. **8**, 2851–2862 (2015). https://doi.org/10.1039/c5ee01822f
307. Wadsworth, B.L., Beiler, A.M., Khusnutdinova, D., et al.: Interplay between light flux, quantum efficiency, and turnover frequency in molecular-modified photoelectrosynthetic assemblies. J. Am. Chem. Soc. **141**, 15932–15941 (2019). https://doi.org/10.1021/jacs.9b07295
308. Gurrentz, J.M., Rose, M.J.: Non-catalytic benefits of Ni(II) binding to an Si(111)-PNP construct for photoelectrochemical hydrogen evolution reaction: metal ion induced flat band potential modulation. J. Am. Chem. Soc. **142**, 5657–5667 (2020). https://doi.org/10.1021/jacs.9b12824
309. Baikie, T., Fang, Y.N., Kadro, J.M., et al.: Synthesis and crystal chemistry of the hybrid perovskite $(CH_3NH_3)PbI_3$ for solid-state sensitised solar cell applications. J. Mater. Chem. A **1**, 5628 (2013). https://doi.org/10.1039/c3ta10518k
310. Noh, J.H., Im, S.H., Heo, J.H., et al.: Chemical management for colorful, efficient, and stable inorganic-organic hybrid nanostructured solar cells. Nano Lett. **13**, 1764–1769 (2013). https://doi.org/10.1021/nl400349b
311. Eperon, G.E., Stranks, S.D., Menelaou, C., et al.: Formamidinium lead trihalide: a broadly tunable perovskite for efficient planar heterojunction solar cells. Energy Environ. Sci. **7**, 982 (2014). https://doi.org/10.1039/c3ee43822h
312. Saliba, M., Matsui, T., Seo, J.Y., et al.: Cesium-containing triple cation perovskite solar cells: improved stability, reproducibility and high efficiency. Energy Environ. Sci. **9**, 1989–1997 (2016). https://doi.org/10.1039/c5ee03874j
313. Smith, I.C., Hoke, E.T., Solis-Ibarra, D., et al.: A layered hybrid perovskite solar-cell absorber with enhanced moisture stability. Angew. Chem. Int. Ed. **53**, 11232–11235 (2014). https://doi.org/10.1002/anie.201406466
314. Kim, I.S., Cao, D.H., Buchholz, D.B., et al.: Liquid water- and heat-resistant hybrid perovskite photovoltaics via an inverted ALD oxide electron extraction layer design. Nano Lett. **16**, 7786–7790 (2016). https://doi.org/10.1021/acs.nanolett.6b03989
315. Habisreutinger, S.N., Leijtens, T., Eperon, G.E., et al.: Carbon nanotube/polymer composites as a highly stable hole collection layer in perovskite solar cells. Nano Lett. **14**, 5561–5568 (2014). https://doi.org/10.1021/nl501982b
316. Kim, I.S., Pellin, M.J., Martinson, A.B.F.: Acid-compatible halide perovskite photocathodes utilizing atomic layer deposited TiO_2 for solar-driven hydrogen evolution. ACS Energy Lett. **4**, 293–298 (2019). https://doi.org/10.1021/acsenergylett.8b01661
317. Zhang, H.F., Yang, Z., Yu, W., et al.: A sandwich-like organolead halide perovskite photocathode for efficient and durable photoelectrochemical hydrogen evolution in water. Adv. Energy Mater. **8**, 1800795 (2018). https://doi.org/10.1002/aenm.201800795
318. Kim, J.H., Seo, S., Lee, J.H., et al.: Perovskite-based photocathodes: efficient and stable perovskite-based photocathode for photoelectrochemical hydrogen production. Adv. Funct. Mater. **31**, 2170119 (2021). https://doi.org/10.1002/adfm.202170119
319. Koo, B., Kim, D., Boonmongkolras, P., et al.: Unassisted water splitting exceeding 9% solar-to-hydrogen conversion efficiency by Cu(In, Ga)(S, Se)$_2$ photocathode with modified surface band structure and halide perovskite solar cell. ACS Appl. Energy Mater. **3**, 2296–2303 (2020). https://doi.org/10.1021/acsaem.9b02387
320. Dias, P., Schreier, M., Tilley, S.D., et al.: Transparent cuprous oxide photocathode enabling a stacked tandem cell for unbiased water splitting. Adv. Energy Mater. **5**, 1501537 (2015). https://doi.org/10.1002/aenm.201501537
321. Park, N.M., Choi, C.J., Seong, T.Y., et al.: Quantum confinement in amorphous silicon quantum dots embedded in silicon nitride. Phys. Rev. Lett. **86**, 1355–1357 (2001). https://doi.org/10.1103/physrevlett.86.1355
322. Gopalakrishnan, S., Shankar, R., Kolandaivel, P.: Effect of doping on the opto-electronic properties of hollow spheroid ZnO quantum dots: a theoretical study. Mater. Sci. Eng. B **270**, 115220 (2021). https://doi.org/10.1016/j.mseb.2021.115220
323. Huang, X., Guo, Q., Yang, D., et al.: Reversible 3D laser printing of perovskite quantum dots inside a transparent medium. Nat. Photonics **14**, 82–88 (2020). https://doi.org/10.1038/s41566-019-0538-8
324. Wu, K., Li, H., Klimov, V.I.: Tandem luminescent solar concentrators based on engineered quantum dots. Nat. Photonics **12**, 105–110 (2018). https://doi.org/10.1038/s41566-017-0070-7
325. Shu, Y.F., Lin, X., Qin, H.Y., et al.: Quantum dots for display applications. Angew. Chem. Int. Ed. **59**, 22312–22323 (2020). https://doi.org/10.1002/anie.202004857
326. Litvin, A.P., Martynenko, I.V., Purcell-Milton, F., et al.: Colloidal quantum dots for optoelectronics. J. Mater. Chem. A **5**, 13252–13275 (2017). https://doi.org/10.1039/c7ta02076g
327. Chistyakov, A.A., Zvaigzne, M.A., Nikitenko, V.R., et al.: Optoelectronic properties of semiconductor quantum dot solids for photovoltaic applications. J. Phys. Chem. Lett. **8**, 4129–4139 (2017). https://doi.org/10.1021/acs.jpclett.7b00671
328. Ryu, H., Hong, S., Kim, H.S., et al.: Role of quantum confinement in 10 nm scale perovskite optoelectronics. J. Phys. Chem. Lett. **10**, 2745–2752 (2019). https://doi.org/10.1021/acs.jpclett.9b00645
329. Su, W.A., Shen, W.Z.: A statistical exploration of multiple exciton generation in silicon quantum dots and optoelectronic application. Appl. Phys. Lett. **100**, 071111 (2012). https://doi.org/10.1063/1.3687184
330. Ruberu, T.P.A., Dong, Y.M., Das, A., et al.: Photoelectrochemical generation of hydrogen from water using a CdSe quantum dot-sensitized photocathode. ACS Catal. **5**, 2255–2259 (2015). https://doi.org/10.1021/cs5021035
331. Li, X.B., Liu, B., Wen, M., et al.: Solar energy conversion: hole-accepting-ligand-modified CdSe QDs for dramatic enhancement of photocatalytic and photoelectrochemical hydrogen evolution by solar energy. Adv. Sci. **3**, 1500282 (2016). https://doi.org/10.1002/advs.201670020
332. Kang, S.H., Zhu, K., Neale, N.R., et al.: Hole transport in sensitized CdS–NiO nanoparticle photocathodes. Chem. Commun. **47**, 10419–10421 (2011). https://doi.org/10.1039/c1cc13932k
333. Lv, H., Wang, C., Li, G., et al.: Semiconductor quantum dot-sensitized rainbow photocathode for effective photoelectrochemical

hydrogen generation. Proc. Natl. Acad. Sci. U. S. A. **114**, 11297–11302 (2017). https://doi.org/10.1073/pnas.1712325114
334. Roy, K., Ghosh, D., Sarkar, K., et al.: Chlorophyll(a)/carbon quantum dot bio-nanocomposite activated nano-structured silicon as an efficient photocathode for photoelectrochemical water splitting. ACS Appl. Mater. Interfaces **12**, 37218–37226 (2020). https://doi.org/10.1021/acsami.0c10279
335. Ghosh, D., Roy, K., Sarkar, K., et al.: Surface plasmon-enhanced carbon dot-embellished multifaceted Si(111) nanoheterostructure for photoelectrochemical water splitting. ACS Appl. Mater. Interfaces **12**, 28792–28800 (2020). https://doi.org/10.1021/acsami.0c05591
336. Ma, C.Y., Ma, D.K., Yu, W.Y., et al.: Ag and N-doped graphene quantum dots co-modified $CuBi_2O_4$ submicron rod photocathodes with enhanced photoelectrochemical activity. Appl. Surf. Sci. **481**, 661–668 (2019). https://doi.org/10.1016/j.apsusc.2019.03.172
337. Meng, P., Wang, M., Yang, Y., et al.: CdSe quantum dots/molecular cobalt catalyst co-grafted open porous NiO film as a photocathode for visible light driven H_2 evolution from neutral water. J. Mater. Chem. A **3**, 18852–18859 (2015). https://doi.org/10.1039/c5ta06255a
338. Li, J., Gao, X., Liu, B., et al.: Graphdiyne: a metal-free material as hole transfer layer to fabricate quantum dot-sensitized photocathodes for hydrogen production. J. Am. Chem. Soc. **138**, 3954–3957 (2016). https://doi.org/10.1021/jacs.5b12758
339. Su, X., Chen, Y., Ren, L., et al.: Cobalt catalyst grafted CdSeTe quantum dots on porous NiO as photocathode for H_2 evolution under visible light. ACS Sustainable Chem. Eng. **7**, 11166–11174 (2019). https://doi.org/10.1021/acssuschemeng.9b00305
340. Lai, L.H., Gomulya, W., Berghuis, M., et al.: Organic–inorganic hybrid solution-processed H_2-evolving photocathodes. ACS Appl. Mater. Interfaces **7**, 19083–19090 (2015). https://doi.org/10.1021/acsami.5b04550
341. Zhou, R., Stalder, R., Xie, D., et al.: Enhancing the efficiency of solution-processed polymer: colloidal nanocrystal hybrid photovoltaic cells using ethanedithiol treatment. ACS Nano **7**, 4846–4854 (2013). https://doi.org/10.1021/nn305823w
342. Liu, Y., Gibbs, M., Puthussery, J., et al.: Dependence of carrier mobility on nanocrystal size and ligand length in PbSe nanocrystal solids. Nano Lett. **10**, 1960–1969 (2010). https://doi.org/10.1021/nl101284k
343. Su, D.W., Ran, J., Zhuang, Z.W., et al.: Atomically dispersed Ni in cadmium-zinc sulfide quantum dots for high-performance visible-light photocatalytic hydrogen production. Sci. Adv. **6**, eaaz8447 (2020). https://doi.org/10.1126/sciadv.aaz8447
344. Barkhouse, D.A., Pattantyus-Abraham, A.G., Levina, L., et al.: Thiols passivate recombination centers in colloidal quantum dots leading to enhanced photovoltaic device efficiency. ACS Nano **2**, 2356–2362 (2008). https://doi.org/10.1021/nn800471c
345. Luther, J.M., Law, M., Song, Q., et al.: Structural, optical, and electrical properties of self-assembled films of PbSe nanocrystals treated with 1, 2-ethanedithiol. ACS Nano **2**, 271–280 (2008). https://doi.org/10.1021/nn7003348
346. Benazzi, E., Cristino, V., Boaretto, R., et al.: Photoelectrochemical hydrogen evolution using $CdTe_xS_{1-x}$ quantum dots as sensitizers on NiO photocathodes. Dalton Trans. **50**, 696–704 (2021). https://doi.org/10.1039/d0dt03567j
347. Liu, B., Li, X.B., Gao, Y.J., et al.: A solution-processed, mercaptoacetic acid-engineered CdSe quantum dot photocathode for efficient hydrogen production under visible light irradiation. Energy Environ. Sci. **8**, 1443–1449 (2015). https://doi.org/10.1039/c5ee00331h
348. Dong, Y.M., Wu, R.X., Jiang, P.P., et al.: Efficient photoelectrochemical hydrogen generation from water using a robust photocathode formed by CdTe QDs and nickel ion. ACS Sustainable Chem. Eng. **3**, 2429–2434 (2015). https://doi.org/10.1021/acssuschemeng.5b00450
349. Wen, M., Wu, H.L., Jian, J.X., et al.: Integrating CdSe quantum dots with a [FeFe]-hydrogenase mimic into a photocathode for hydrogen evolution at a low bias voltage. ChemPhotoChem **1**, 260–264 (2017). https://doi.org/10.1002/cptc.201700041
350. Wu, H.L., Li, X.B., Wang, Y., et al.: Hand-in-hand quantum dot assembly sensitized photocathodes for enhanced photoelectrochemical hydrogen evolution. J. Mater. Chem. A **7**, 26098–26104 (2019). https://doi.org/10.1039/c9ta10056c
351. Yang, J.F., Goguen, J., Kleiman, R.: Silicon solar cell with integrated tunnel junction for multijunction photovoltaic applications. IEEE Electron Device Lett. **33**, 1732–1734 (2012). https://doi.org/10.1109/LED.2012.2217391
352. Jin, Hu., W., Wang, Z., Yu, W., et al.: Optically controlled electroresistance and electrically controlled photovoltage in ferroelectric tunnel junctions. Nat. Commun. **7**, 10808 (2016). https://doi.org/10.1038/ncomms10808
353. Wang, X., Koleilat, G.I., Tang, J., et al.: Tandem colloidal quantum dot solar cells employing a graded recombination layer. Nat. Photonics **5**, 480–484 (2011). https://doi.org/10.1038/nphoton.2011.123
354. Hou, P.F., Yang, K.X., Ni, K.K., et al.: An ultrathin flexible electronic device based on the tunneling effect: a flexible ferroelectric tunnel junction. J. Mater. Chem. C **6**, 5193–5198 (2018). https://doi.org/10.1039/c8tc00500a
355. Wang, M., Cai, W., Zhu, D., et al.: Field-free switching of a perpendicular magnetic tunnel junction through the interplay of spin–orbit and spin-transfer torques. Nat. Electron. **1**, 582–588 (2018). https://doi.org/10.1038/s41928-018-0160-7
356. Grifoni, M., Hänggi, P.: Driven quantum tunneling. Phys. Rep. **304**, 229–354 (1998). https://doi.org/10.1016/S0370-1573(98)00022-2
357. Gatteschi, D., Sessoli, R.: Quantum tunneling of magnetization and related phenomena in molecular materials. Angew. Chem. Int. Ed. **42**, 268–297 (2003). https://doi.org/10.1002/anie.200390099
358. Liu, J., Zhang, Y.Q., Chen, J., et al.: Separation and quantum tunneling of photo-generated carriers using a tribo-induced field. Matter **1**, 650–660 (2019). https://doi.org/10.1016/j.matt.2019.05.017
359. Lewerenz, H.J., Skorupska, K., Muñoz, A.G., et al.: Micro- and nanotopographies for photoelectrochemical energy conversion. II: Photoelectrocatalysis - Classical and advanced systems. Electrochim. Acta **56**, 10726–10736 (2011). https://doi.org/10.1016/j.electacta.2011.05.028
360. Muñoz, A.G., Lewerenz, H.J.: Advances in photoelectrocatalysis with nanotopographical photoelectrodes. ChemPhysChem **11**, 1603–1615 (2010). https://doi.org/10.1002/cphc.200900856
361. Fan, F.R.F., Keil, R.G., Bard, A.J.: Semiconductor electrodes. 48. Photooxidation of halides and water on n-silicon protected with silicide layers. J. Am. Chem. Soc. **105**, 220–224 (1983). https://doi.org/10.1021/ja00340a013
362. Kobayashi, M., Kinoshita, A., Saraswat, K., et al.: Fermi-level depinning in metal/Ge Schottky junction and its application to metal source/drain Ge NMOSFET. 2008 Symposium on VLSI Technology. Honolulu, HI, USA. IEEE, 54–55 (2008). https://doi.org/10.1109/VLSIT.2008.4588561
363. Esposito, D.V., Levin, I., Moffat, T.P., et al.: H_2 evolution at Si-based metal–insulator–semiconductor photoelectrodes enhanced by inversion channel charge collection and H spillover. Nat. Mater. **12**, 562–568 (2013). https://doi.org/10.1038/nmat3626
364. Ji, L., McDaniel, M.D."., Wang, S., et al.: A silicon-based photocathode for water reduction with an epitaxial $SrTiO_3$ protection layer and a nanostructured catalyst. Nat. Nanotechnol. **10**, 84–90 (2015). https://doi.org/10.1038/nnano.2014.277

365. Zhang, H., Zhang, P., Zhao, J., et al.: The hole-tunneling heterojunction of hematite-based photoanodes accelerates photosynthetic reaction. Angew. Chem. Int. Ed. **60**, 16009–16018 (2021). https://doi.org/10.1002/anie.202102983
366. Ji, L., Hsu, H.Y., Li, X.H., et al.: Localized dielectric breakdown and antireflection coating in metal–oxide–semiconductor photoelectrodes. Nat. Mater. **16**, 127–131 (2017). https://doi.org/10.1038/nmat4801
367. Young, J.L., Steiner, M.A., Döscher, H., et al.: Direct solar-to-hydrogen conversion via inverted metamorphic multi-junction semiconductor architectures. Nat. Energy **2**, 17028 (2017). https://doi.org/10.1038/nenergy.2017.28
368. Yang, W., Park, J., Kwon, H.C., et al.: Solar water splitting exceeding 10% efficiency via low-cost Sb_2Se_3 photocathodes coupled with semitransparent perovskite photovoltaics. Energy Environ. Sci. **13**, 4362–4370 (2020). https://doi.org/10.1039/d0ee02959a
369. Edwardes Moore, E., Andrei, V., Zacarias, S., et al.: Integration of a hydrogenase in a lead halide perovskite photoelectrode for tandem solar water splitting. ACS Energy Lett. **5**, 232–237 (2020). https://doi.org/10.1021/acsenergylett.9b02437
370. Luo, J.S., Li, Z., Nishiwaki, S., et al.: Targeting ideal dual-absorber tandem water splitting using perovskite photovoltaics and $CuIn_xGa_{1-x}Se_2$ photocathodes. Adv. Energy Mater. **5**, 1501520 (2015). https://doi.org/10.1002/aenm.201501520
371. Lee, H., Yang, J.W., Tan, J., et al.: Crystal facet-controlled efficient SnS photocathodes for high performance bias-free solar water splitting. Adv. Sci. **8**, 2170142 (2021). https://doi.org/10.1002/advs.202170142
372. Jun, S.E., Hong, S.P., Choi, S., et al.: Boosting unassisted alkaline solar water splitting using silicon photocathode with TiO_2 nanorods decorated by edge-rich MoS_2 nanoplates. Small **17**, 2103457 (2021). https://doi.org/10.1002/smll.202103457
373. Yang, J.W., Park, I.J., Lee, S.A., et al.: Near-complete charge separation in tailored $BiVO_4$-based heterostructure photoanodes toward artificial leaf. Appl. Catal. B Environ. **293**, 120217 (2021). https://doi.org/10.1016/j.apcatb.2021.120217
374. Lee, S.A., Park, I.J., Yang, J.W., et al.: Electrodeposited heterogeneous nickel-based catalysts on silicon for efficient sunlight-assisted water splitting. Cell Rep. Phys. Sci. **1**, 100219 (2020). https://doi.org/10.1016/j.xcrp.2020.100219

Yibo Zhao was awarded a B.E. degree in 2016 by the Qingdao University of Science and Technology, China. In 2016, he joined the research group of Professor Jinlin Long at the State Key Laboratory of Photocatalysis on Energy and Environment as a master's candidate. In 2018, he began to study for a degree as a PhD candidate under the supervision of Professor Xianzhi Fu and Professor Jinlin Long. Now he is focusing on photoelectrochemical hydrogen production and directional conversion of methane molecules at room temperature and pressure.

Zhenjie Niu received a B.E. degree in 2019 from Xuchang University, China. In 2020, she joined the research group of Professor Jinlin Long at the State Key Laboratory of Photocatalysis on Energy and Environment as a master's candidate. Now she is focusing on theoretical calculations based on first principles, photoelectrocatalytic water splitting and carbon dioxide reduction.

Jiwu Zhao received a B.E. degree in Chemical Engineering and Technology in 2016 from Fuzhou University, China. Subsequently, he joined the research group of Prof. Fulan Zhong at the National Engineering Research Center of Chemical Fertilizer Catalyst as a master's candidate to study automobile exhaust sensors. In 2018, as a PhD candidate, he joined the research group of Prof. Jinlin Long at the State Key Laboratory of Photocatalysis on Energy and Environment, where his work focuses on theoretical calculations based on first principles, photoelectrochemical water oxidation and biomimetic carbon assimilation.

Xue Lan was awarded a B.E. degree in 2020 by Henan University, China. In 2020, she joined the research group of Prof. Jinlin Long at the State Key Laboratory of Photocatalysis on Energy and Environment as a master's candidate. Now she is focusing on theoretical calculations based on first principles, photoelectrocatalytic water splitting and carbon dioxide reduction.

Xianzhi Fu received a B.S. degree in 1982 and a PhD degree in 1991 from Peking University. After a postdoctoral stay (1991–1993) at Peking University and a later postdoctoral stay at the University of Wisconsin-Madison (1993–1997), he was appointed as a full professor at Fuzhou University, China. He was selected as an academician of the Chinese Academy of Engineering (CAE) in 2009. Currently, he is the president of Fuzhou

University and the director of the State Key Laboratory of Photocatalysis on Energy and Environment. His research focuses on the development of photocatalysis and photoelectrocatalysis to solve energy and environmental problems.

Jinlin Long obtained a PhD degree from Fuzhou University in 2009. After that, he completed one year of post-doctoral training (2012) at Nanyang Technological University, Singapore, and conducted one year of visiting research (2016) in the Department of Chemistry at Emory University, USA. Currently, he is a full Professor in the State Key Laboratory of Photocatalysis on Energy and Environment at Fuzhou University, China. His research interests focus on the development of photocatalysts, artificial photosystems, and photoelectrochemical cells and devices for solar-to-chemical energy conversions.